ORIGIN AND AGE OF TABULAR MASSIVE ICE AND ICE WEDGES IN THE SMOKING HILLS, NORTHWEST TERRITORIES, CANADA

CLODY DESJARDINS

Thesis submitted to the University of Ottawa
in partial Fulfillment of the requirements for the
Master of Science in Geography

Department of Geography, Environment and Geomatics
Faculty of Arts
Université d'Ottawa

Abstract

The Smoking Hills area is located in the Northwest Territories, Canada. It contains many retrogressive thaw slumps that expose different permafrost units, including tabular massive ice and ice wedges. This study investigates the origin and age of these ice bodies to refine the glacial and permafrost history of the Smoking Hills region. Using cryostratigraphic observations, stable water isotope analysis, major ion geochemistry, and radiocarbon dating, samples from four retrogressive thaw slumps headwalls were analyzed. The results suggest that three of the sites contained buried glacial ice deposited during the Late Wisconsinan glaciation. Deformed and truncated ice wedges at one of the sites also show evidence of a glacial retreat during the Bølling–Allerød interstadial followed by a short glacial re-advance before of during the Younger Dryas. Holocene-aged ice wedges from a second retrogressive thaw slumps reflect the re-establishment of permafrost after the Wisconsin glaciation. Chemical anomalies in some ice units indicate a possible influence from the Smoking Hills Formation on Holocene-aged ground ice. These results highlight a dynamic glacial and permafrost history in the region.

Acknowledgments

First, I would like to thank my supervisor, Denis Lacelle for having given me the opportunity to do this project and work in the Canadian Arctic. Without his help and support, this project would not exist.

I am also very grateful to my co-supervisor, Rod Smith, whose insightful comments and expertise greatly enriched this project. Without his contributions, this work would not have been possible.

This project is part of the Natural Resources Canada's GEM Geo-North Cretaceous Black Shale project, and I would like to recognize their financial (RAP Bursary) and logistical support. This research was conducted under Inuvialuit Land Administration licence ILA23TN007, and Northwest Territories Scientific Research licence 17284.

I also wish to acknowledge the Northern Scientific Training Program (NSTP), Natural Sciences and Engineering Research Council of Canada (NSERC) Discovery Grant and NSERC Northern Supplement program, for their monetary and logistical support.

I would also like to thank the Paulatuk and Tuktoyaktuk Hunters and Trappers' Committees for their review and approval of this research. I am especially grateful to Kelly Ruben from Paulatuk and Johnny Panaktalok from Tuktoyaktuk for their assistance in the field.

Thank you to John Gosse, for his help during fieldwork and for supporting the development of this research.

I am grateful to Paul Middlestead and the team at the Jan Veizer Stable Isotope Laboratory, Sarah Murseli and her team at the A.E. Lalonde AMS Laboratory, Smitarani Mohanty and Nimal DeSilva from the Geochemistry Laboratory, as well as Shauna Madore and her team at the Geochemistry & Sedimentology Labs of Natural Resources Canada. It was a pleasure collaborating with all of you.

To my colleagues, thank you for your moral and technical support, especially with the many technical and administrative aspects involved in completing this thesis.

Finally, I want to thank my friends and family for your unwavering support, encouragement, and patience throughout this journey. Your belief in me made all the difference.

Table of Contents

List of Figures and Tables:

1. Introduction

Large tabular bodies of massive ground ice are often located in formerly glaciated terrain near the maximum and recessional extent of ice sheets (Mackay, 1971; Lorraine and Demeur 1985; French and Harry, 1990; Dyke and Savelle, 2000; Dyke and Evans 2003; Ingólfsson and Lokrantz, 2003; Lacelle et al., 2018; Coulombe et al., 2019). The development and preservation of these tabular massive ice bodies reflect a heritage of Late Quaternary glacial history and ground thermal conditions. In western Arctic Canada, the origin of tabular massive ice bodies preserved in permafrost has been associated with either: i) the burial of remnants of glacial ice (usually from the Laurentide Ice Sheet; LIS) by an insulating cover of supraglacial meltout debris with thicknesses greater than the active layer (e.g., Dyke and Savelle, 2000; Lakeman and England, 2012); or ii) the in situ freezing of glacial-fed groundwater migrating in a talik toward a freezing front during permafrost aggradation (i.e., segregated-intrusive origin) (Dallimore and Wolfe, 1988; Harry et al., 1988; Rampton, 1988; Mackay and Dallimore, 1992; Lacelle et al., 2004).

The Smoking Hills region in the Northwest Territories (NWT) was covered by the LIS during the last glacial maximum (Evans et al., 2021; Dalton et al., 2023). Recent climate warming has initiated numerous retrogressive thaw slumps (RTS) in this region that expose tabular massive ice and ice-rich permafrost (Kokelj et al., 2017). Cryostratigraphic observations of the headwall of a RTS along a tributary of the Anderson River in the Smoking Hills in 2018 revealed deformed and thermally truncated ice wedges 4-5 m below the surface that developed within tabular massive ice (inferred to be Pleistocene age) covered by an icy diamict (Evans et al., 2021). The deformation of the ice wedges is aligned with streamlined landforms and other ice flow directional indicators in the immediate vicinity, which suggest deformation and shear of the ice wedges and enclosing tabular massive ice by an overriding ice sheet (Evans, 2018). Based on these observations, Evans et al. (2021) suggested that either: i) the ice wedges developed prior to the last glaciation and their subglacial deformation occurred during the advance of the LIS during the Late Wisconsin glaciation; or ii) the ice wedges developed following the retreat of the LIS, but the LIS had at least one episode of re-advancement, leading to the subglacial deformation of the ice wedges. As such, the Smoking Hills region either preserve evidence of pre-Late Wisconsin glaciation (MIS2) or the LIS during the Late Wisconsin glaciation was more dynamic than previously reconstructed (i.e., Rampton, 1988; Dyke et al., 2003; Duk-Rodkin et al., 2004; Tarasov et al., 2012; Batchelor et al., 2013, 2014; Margold et al., 2014, 2015).

This thesis was undertaken as part of the Geo-Mapping for Energy and Minerals (GEM) Geo North Cretaceous black shales project of Natural Resources Canada (Geological Survey of Canada) and contributes to studies focused on resolving aspects of glacial history and mineral dispersal. The aim of this study is to better understand the glacial and permafrost history of the Smoking Hills region and the implications this has for understanding indicator mineral dispersal in the region (**Figure 1**). This thesis mapped the distribution of RTS in the study area based on satellite imagery and determine the origin and age of tabular massive ice and ice wedges exposed in the headwalls of four RTS. Overall, the results helped to determine the timing and development of the ice wedges and consequently evaluate the timing as well as the advance and retreat dynamics of the LIS in the Smoking Hills.

1.1. Objectives

The study of the origin and age of tabular massive ice and ice wedges exposed by RTS in the Smoking Hills area aims to improve understanding of the glacial and permafrost history of the region. More specifically, the objectives are to: (1) assess the distribution of retrogressive thaw slumping in the Smoking Hills using satellite imagery; (2) determine the origin and characteristics of tabular massive ice and interstitial ice in the Smoking Hills region using the grain size of the enclosed sediments, the concentration of major ions in the ice and in the sediments and the stable water isotope (δD-$\delta^{18}O$) composition of the ice; and (3) determine the age of the ice wedges and massive ice exposed in RTS headwalls based on radiocarbon measurements of the dissolved organic carbon ($^{14}C_{DOC}$).

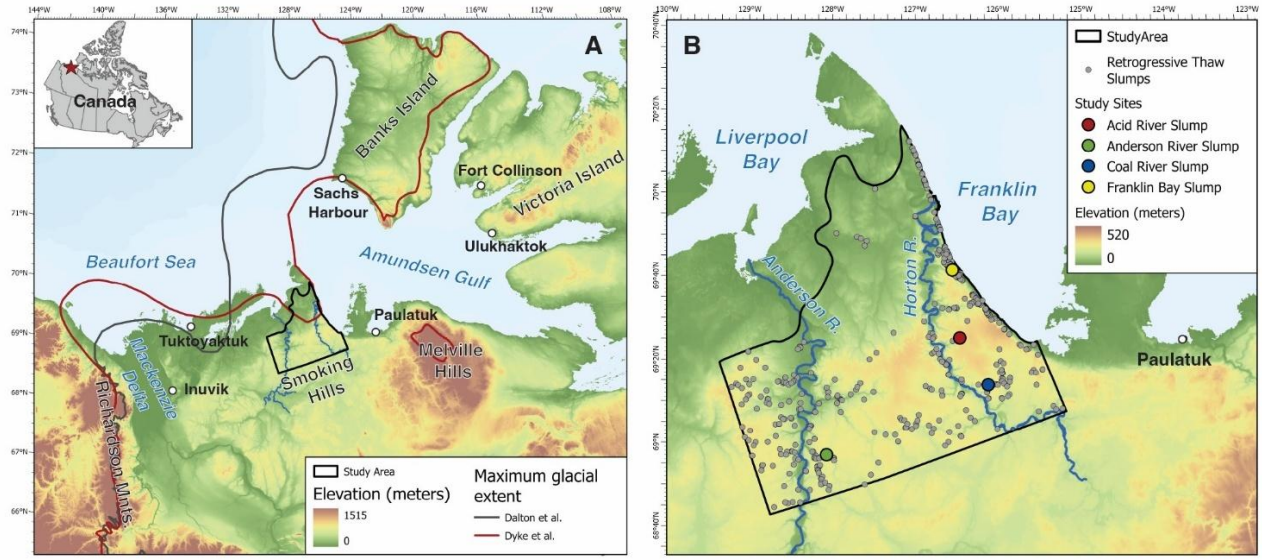

Figure 1. A) Study area in the Smoking Hills, Northwest Territory, western Arctic Canada and the maximum glacial extent as per Dyke et al., 2003 and Dalton et al. 2023. B) Sampled sites and locations of retrogressive thaw slumps identified in this study from satellite imagery.

2. Literature review

2.1. Permafrost

Permafrost is defined as ground that is continuously cryotic (temperature bellow 0 °C). It is found in many parts of the world, including the Arctic, the Tibetan plateau, Antarctica and mountains. In total, it covers over 23-25% of the world's land mass (French, 2007) and 50% of Canada's land mass (Smith and Riseborough, 2002). It can be categorized in different ways depending on its composition (e.g. ice-rich, ice-poor) or its distribution. The regions covered by permafrost are often categorized as continuous (90-100%), discontinuous (50-90%), sporadic (10-50%) or isolated (0-10%). The southern limits of these types of permafrost often roughly correspond to mean annual air temperature (MAAT) isotherms. For example, the southern limit of discontinuous permafrost is relatively close to the -1 °C MAAT isotherm. The southern limit of continuous permafrost, on the other hand, often corresponds to the -6 to -8 °C MAAT isotherm (Smith and Riseborough, 2002; French, 2007). The limit between continuous and discontinuous permafrost is also relatively close to the tree line. This means that continuous permafrost is more typical of an area covered by tundra, while discontinuous permafrost is more likely to be found in areas covered by boreal forest (French, 2007).

Permafrost is a thermal state of earth materials, defined by temperatures below 0°C for at least 2 years. It often (though not always) is composed of a mix of sediments and ground ice. This ice can take different forms depending on the conditions of formation. The three most common types of ground ice are pore ice followed by segregated ice and ice wedges. We can also find intrusive ice, ice veins and massive ice (French, 2007).

2.1.1. Ice wedges

Ice wedges are created through the formation of thermal contraction cracks that form during the winter and fill with meltwater during spring. When it freezes again, the water expands and often deforms the surrounding material (Leffingwell, 1915). This type of permafrost feature favours continuous permafrost and poorly drained tundra lowlands. This is due to the fact that they require a sufficient source of moisture and also need temperatures to be cold enough for the ice to crack under the stress of seasonal temperature changes (French, 2007). They will also grow better in flat to gently-sloped unconsolidated sediments, although they can also be found in bedrock and steeper-sloped areas. The frequency and direction of cracking vary according to the changes in air temperature, topography, type of sediment, and depth of snow cover (Mackay, 1984). If the snow cover is thin, there is a high correlation between the short-term variation in air temperature and the cracking of an ice wedge. Mackay (1993) reported that if there is a low snow cover depth in the Mackenzie Delta, ice wedge cracking is more likely when there is a change in temperature of around 1.8 °C per day for 4 consecutive days or more. Since ice wedge cracking is induced by a short-term change in temperature, the crack usually starts at lower depths, at the ground surface or near the top of permafrost (Mackay, 1993; 1984). Studies have also shown that the crack will usually form towards the middle of the ice wedges (Mackay, 1975), which is why the older parts of an ice wedge are typically found at the edges.

Ice wedges can be classified based on different characteristics, including the frequency of cracking, in which case they will be categorized as active, inactive or relict, or based on how they formed, in which case they will be categorized as epigenetic, syngenetic or anti-syngenetic (**Figure 2**; French, 2007).

Epigenetic ice wedges grow in stable and flat terrain where permafrost is already established. This means that they will be younger than the host sediments and their depth usually remains the same through time. Their growth is therefore lateral, making them wider with time.

This means that the surrounding material is pushed outward, deforming the surrounding units and creating an uplifted bulge around its edges. On the surface, this deformation is characterized by ice wedge furrows, and where these intersect, ice-wedge polygons. These types of ice wedges are typically less than 4.0 m deep and 2.0 m wide (French, 2007). The orientation of their long axis shows verry little variation relative to the slope and they are oriented vertically in a cross-section.

Syngenetic ice wedges grow in an area where the active layer continuously moves upwards, typically due to the accumulation of sediments. The ice wedge will therefore grow upwards, getting taller with time. Their shape, however, depends on the rate of accumulation of sediments and the rate of growth of the ice wedge. For example, an ice wedge will become wider if it grows faster than the sediments are accumulating over it. But if it grows slower than the sediments are accumulating, the ice wedge will become thinner. Similar to the epigenetic ice wedges, the slope angle and orientation has verry little impact on the orientation of the long axis and, in a cross section, they are oriented vertically. Since the formation of these types of ice wedges requires a long period of constant sedimentation and a sufficiently cold climate, most modern

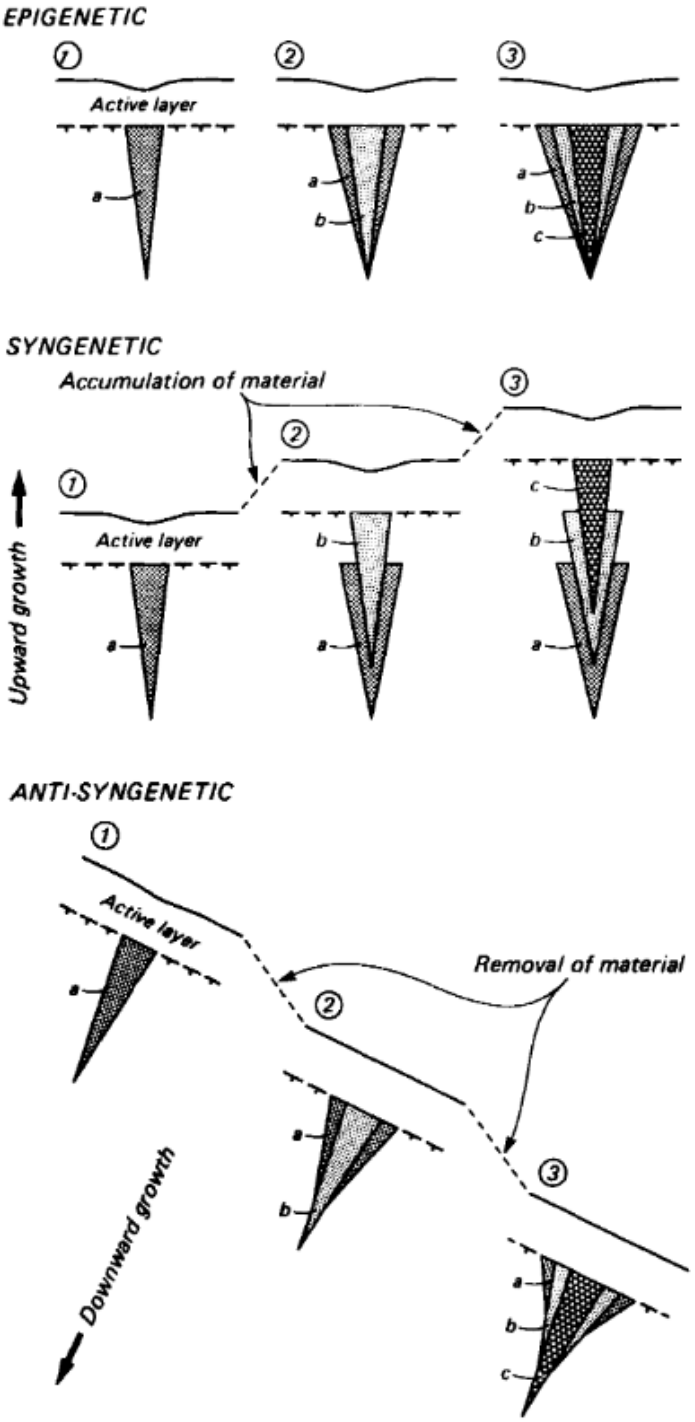

Figure 2. Schematic diagram showing three growth stages of epigenetic, syngenetic and anti-syngenetic ice wedges. Taken from Mackay (1990).

syngenetic ice wedges tend to be relatively small. Some Pleistocene-age syngenetic ice wedges, however, can be much larger. Also, since these types of ice wedges grow more or less at the same time as the enclosing material, the age of the ice wedge should be similar to the age of the surrounding sediments (French, 2007).

Anti-syngenetic ice wedges are the most common type of ice wedges in the western Canadian Arctic, probably due to the hilly terrain (Mackay, 1995). They form in areas where the active layer is moving downwards, typically due to the removal of overlying material. This means that the top of the ice wedge is repeatedly melted. However, since the thermal-contraction cracking remains the same, the ice wedge also keeps moving downwards. These ice wedges therefore typically grow to be wider than they are deep (Mackay, 1995; French, 2007). Unlike epigenetic and syngenetic ice wedges, in a cross-section, anti-syngenetic ice wedges can show a vertical or tilted orientation depending on the orientation o the cross-section in relation to the slope (Mackay, 1995). The ice wedge will therefore appear to have a vertical orientation if the cross-section is parallel to the slope. On the contrary, if the cross-section is oblique to the slope, the ice wedges will appear tilted.

2.1.2. Massive ice – segregated vs. buried glacial

Tabular massive ice is often found near the limits of past glaciations or along ice-margin stillstands (French and Harry, 1990; Dyke and Savelle, 2000; Dyke and Evans, 2003; Ingólfsson and Lokrantz, 2003; Lacelle et al., 2018; Coulombe et al., 2019). Their origin is typically associated with one of two processes: relict buried glacial ice (Lorrain and Demeur, 1985; St-Onge and McMartin, 1995; Dyke and Savelle, 2000) or segregated-intrusive ice (Rampton 1988; Mackay and Dallimore, 1992; Lacelle et al. 2004). Although the two can be very similar, there are some distinctive characteristics that allow us to differentiate the two. The type of contact between the massive ice unit and the overlying unit is perhaps one of the easiest to observe. A conformal contact (gradual change) is more typical of segregated ice, while a thaw unconformity (abrupt transition between two units due to a previous deepening of the active layer) at the top of the massive ice unit is more likely to be explained by a buried glacial origin (Harry et al., 1988; French and Harry, 1990). This is explained by the fact that an upwards progressive transition from clean ice to ice-rich sediments is probably best explained by a freezing front moving downwards (Harry et al., 1988), although it does not entirely exclude the possibility of a glacial origin. An abrupt transition

between clear ice and the overlying sediment-rich unit is more consistent with a glacial origin, as it suggests that the ice was emplaced prior to sediment deposition, rather than forming progressively through in situ freezing like segregated ice. However, it could also be caused by a thermal unconformity that developed after the formation of segregated massive ice. The difference in age between the massive ice and the overlying unit is another potential difference between the two types of massive ice. If the massive ice unit is older than the overlying sediments, then it is likely to have a buried glacial origin (French, 1990). The transitions at the contact between the massive ice unit and the overlying unit can also be reflected in the changes in water chemistry (e.g. oxygen isotopes and major ions; French et al., 1990). A gradual chemical transition across this interface may indicate the formation of segregated ice, whereas an abrupt transition in composition is more consistent with a buried glacial ice origin (French et al., 1990).

The isotopic composition is another difference between the two massive ice origins. While the δD-$\delta^{18}O$ regression slope of buried glacial ice is more likely to be around the global meteoric water line (GMWL=8.0) since the main source of moisture forming a glacier comes from precipitations, the regression slope of segregation ice is typically closer to 6.0 due to isotope fractionation (Lorrain and Demers, 1985; Mackay and Dallimore, 1992). The ratio of deuterium (δD) and mean deuterium-excess (d) can also be used to differentiate between different massive ice origin. For example, water that is frozen under equilibrium conditions will often have a strong negative relationship between d and δD due to the presence of a freezing slope (Souchez et al. 2000; Lacelle et al. 2008; Fritz et al. 2011). On the contrary, water that is frozen under non-equilibrium conditions or that froze in thin, successive layers in an open system will not have any linear relationship between d and δD (Souchez et al., 2000; Michael et al., 2011).

The $\delta^{18}O$ values themselves are also a good indicator of the ice's origin. For example, buried glacial ice in the western Canadian Arctic has very low $\delta^{18}O$ values (typically between -27 and -35‰; Lorrain and Demeur, 1985; French and Harry, 1990; Murton et al., 2004; Lacelle et al., 2018; Coulombe et al., 2019). Segregated-intrusive massive ice, on the other hand, typically have slightly higher $\delta^{18}O$ values, but can still range from -25 to -35‰ (Mackay and Dallimore, 1992; Lacelle et al., 2004; Murton et al., 2004; Roy et al., 2023). The overlap in $\delta^{18}O$ values between buried glacial ice and segregated-intrusive massive ice can be explained by the fact that the latter can come from infiltrated glacial meltwater. Since both ice types can derive from the same glacial source water, they may share similar isotopic signatures despite their different formation processes

2.1.3. Buried glacial massive ice

The burial of glacial ice is usually caused by supraglacial melt and the resultant accumulation of an insulating carapace of sediments around terminal margins or by the burial of glacial snouts by fluvial outwash or lacustrine sediments. However, this will only allow the preservation of relict ice if the ground temperature remains below 0 °C and the active layer does not go deeper than the bottom of the insulating carapace of sediments (Dyke and Savelle, 2000; Shur et al., 2005). Because the buried glacial ice is often clast-rich, changes in the depth of the active layer during the postglacial period can result in the combined melting of the upper buried ice, and a resultant thickening of the overlying insulating debris layer. For areas of buried glacial ice that experienced the hypsithermal Holocene warming, it is likely that the depth of overlying sediment reflects this maximum depth of active layer development (sediment accumulation/loss related to slope processes, deflation, etc.), rather than the immediate post-glacial stagnation and burial of the ice itself. Debris concentrations in glacial ice are highly variable (French and Harry, 1990; Murton, 2013; Lacelle et al. 2018; Coulombe et al., 2024).

2.1.4. Retrogressive thaw slumps and contemporary changes in permafrost landscapes

RTS are a type of mass wasting commonly found within areas of continuous permafrost (Huang et al., 2023). More specifically, they often form on sloped terrain underlain by ice-rich permafrost (Lacelle et al., 2015; Wang et al., 2016). They also tend to form clusters within certain areas (Lewkowicz and Way, 2019; Huang et al., 2023) and were reported to be often found in till or morainal deposits around prominent terminal and recessional ice margins (Lacelle et al., 2015; Lewkowicz and Way, 2019). Huang et al.'s (2023) model estimates around 11-20 RTS per 100 km^2 around the Smoking Hills region.

Permafrost containing massive ice is more likely to be subject to RTS due to the preferential erosion and melting of massive ice or ice-rich units and because meltwater can accelerate the movement of the overlying insulating soil layer (Burn et al., 2021).

RTS are caused by an initial mass movement that thins the overlying sediment cover or exposes massive ice or ice-rich permafrost (Mackay, 1974). The exposed or warmed ice then starts to melt, causing the loss of cohesion within the sediments and the initiation of a failure surface. With continuous warming and melting, the surface will lower, causing a progressive overdeepening

of the failure surface. This will lead to the formation of an RTS with an active headwall retreat (Costard et al., 2021). Once the massive ice within the headwall is exposed, the RTS will continue to grow as long as the slumping sediment does not cover/bury the ice-rich permafrost below the thickness of the active layer, or if all the ground ice melts (Burn, 2000; Wang et al., 2016). In the Richardson Mountains (Lacelle et al., 2015), the retreat rate typically varies between a few metres and tens of metres per year.

Van der Sluijs et al. (2023) have shown that the affected area and regional density of RTS within the western Canadian Arctic have increased by 38% and 69%, respectively, between 2004 and 2016. On Banks Island, it has also been reported that the number and density of RTS have significantly increased since 1961 (Rudy et al., 2017; Lewkowicz and Way, 2019). More specifically, the area covered by RTS on eastern Banks Island has reached 76 ha/100 km^2, with their density increasing by 131% since 2009 as opposed to the 35% increase between 1961 and 2009 (Rudy et al., 2017). Lewkowicz and Way (2019) also reported that 86% of the RTS formed between 1984 and 2013 were initiated during years where summer temperatures were particularly high compared to the 5-year centred running mean (over 0.5°C difference).

2.1.5. Permafrost history

Before the Wisconsin glaciation, permafrost was present in the northern Canadian Arctic, but the glacial advance had a big impact on it. Depending on the ice thickness, how long the region was covered by ice and if the glacier was warm or cold based, permafrost could have been eliminated, inhibited or maintained (Dyke, 1993; French, 2007; Hu et al., 2013).

There are, however, indications that the permafrost quickly re-formed during glacial retreat. The large amount of water from the melting glacier as well as the subglacial hydraulic pressure driving flow outward from beneath the ice into the pro-glacial aprons would also have favoured the formation of massive ice and other ice-rich units (Mackay and Dallimore, 1992; Boulton and Caban, 1995; Rampton, 1998). This theory would explain the presence of massive, segregated ice near the northern limits of the Laurentide Ice Sheet as well as buried glacial ice (Dyke and Evans, 2003).

Mackay (1995) also states that many Wisconsinan ice wedges stopped growing (or were thermally truncated) and were buried during the Hypsithemal period, but that some were later "reactivated" due to cold temperatures causing the ice to resume cracking.

3. Study Area

3.1. Physiography and geology

The study area (69°N; 130°W) is located along the west coast of Franklin Bay, south of Cape Bathurst, in the NWT. It covers an area of about 12,820 km^2 and is characterized by a flat to undulating upland (up to 400 m above sea level) that has been incised by the northward-flowing Horton and Anderson rivers and their tributaries. The area is underlain by Cretaceous bedrock composed of poorly consolidated sedimentary rocks of the Mason River, Horton River, and the Smoking Hills formations. The Smoking Hills are named after the spontaneously combusting mudrock (bocannes) that are sometimes formed in landslides or slumped material (Selwyn, 1877; Dawson, 1881; Crickmay, 1967; Mathews and Bustin, 1984; Grasby et al., 2023). The slumping causes intermixing and oxidation of abundant framboidal pyrite and organic-rich materials leading to the combustion of the mudrock. These bocannes emit water vapour and sulfuric acid gas. Ponds found within the Smoking Hills formation are highly acidic and have a very high conductivity (Mathews and Bustin, 1984; Grasby, et al. 2018; Grasby et al., 2022).

3.2. Glacial history

The glacial history of the western Canadian Arctic helped shape the landscape of the Smoking Hills region (Evans et al., 2021). The Quaternary glaciations of the Smoking Hills region can be represented by at least 9 phases that were described by Evans et al. (2021), which likely started with a very old glaciation (2.9 ± 0.3 Ma) and ended with the Late Wisconsin glaciation (phase F-H; **Figure 3**). The first phase (phase A) is the first record of ice advance in the region creating a fluvially incised landscape, but not necessarily as it exists today. The second phase (phase B) is characterized by glacial ice covering the valleys and the upland regions, which deformed the underlying bedrock and sediments. Phase C is the retreat of this glacial ice and the deposition of glacio-fluvial sediments in the proto-Horton River. Phase D is a continuing ice retreat and the development of an ice-dammed lake within the lower Horton River area and possibly other low-lying regions because of the coalescence of ice in the Liverpool Bay and Amundsen Gulf in the lower reach of the Horton River. Phase E corresponds to the draining of the lake and the subsequent potential permafrost aggradation as evidenced by ice wedge pseudomorphs in glaciofluvial gravels. This could also have allowed for the development of the ice wedges observed in the tabular massive

ice body at the Anderson River slump site. Phases F to H represent the advance and retreat of the LIS during the Late Wisconsin period. There are still uncertainties about the timing and position of the local glacial maximum extent. For example, the reconstruction of Dyke et al. (2003) placed the maximum extent of the LIS around 18,000 ^{14}C yr BP (equivalent to 21,400 cal yr BP) and suggested that most of Banks Island, the northern tip of the peninsula between Liverpool Bay and Franklin Bay (including part of the Smoking Hills region) and part of the Tuktoyaktuk Peninsula remained unglaciated (**Figure 4**). Conversely, the reconstruction of Dalton et al. (2023), which included additional cosmogenic ages from Banks and Victoria Islands, suggested that the maximum extent of the LIS occurred around 18,500 cal yr BP and covered the entire region, including all of Banks Island and the Smoking Hills. A more recent study suggested that the timing of the maximum extent probably occurred before 24,000 cal yr BP, reaching all the way to the west of Banks Island and onto the continental and Mackenzie-Beaufort shelves during an early LIS advance (Vaughan et al., 2024). During the Late Wisconsin glaciation, the dominant LIS ice flow in and around the Smoking Hills region alternated between ice feeding northward towards the Amundsen Gulf ice stream (flowing from the east, but remained confined to the marine trough of Amundsen Gulf) and an Anderson ice stream (flowing from the southwest during the deglacial period; **Figure 5**; Stokes et al., 2016; Evans et al., 2021; Stoker et al., 2024). The last phase is the deglaciation that started around 17,000 cal yr BP, where the ice margin retreated eastward of the Mackenzie Valley area so that the Tuktoyaktuk Peninsula and probably a part of the Makenzie Delta and the northern part of the Smoking Hills, were deglaciated by 16,000 cal yr BP (Dalton et al., 2023). At 14,000 cal yr BP, the entire area west of Franklin Bay was deglaciated (Dalton et al., 2023), as the LIS continued to retreat eastward (Murton et al.,1997; Bateman and Murton, 2006; Murton et al., 2007; Stoker et al., 2022; Dalton et al., 2023; Vaughan et al., 2024). However, according to Stokes et al. (2016), the Amundsen Gulf and Anderson ice streams that surrounded the Smoking Hills were last active around 10,800 cal yr BP and 14,300-13,300 cal yr BP, respectively.

The surficial sediments in the study area therefore consist of mostly glacial sediments (till veneer and some till blankets) and some thin colluvial sediment layers (Fulton, 1995). There are also areas of glaciofluvial deposits along the western coast of Franklin Bay and the upper Horton River Valley (Fulton, 1995; Evans et al., 2021). The impact of the last glaciation is shown in geomorphological features such as glacial-thrust moraines, flutings, meltwater channels and eskers

(Klassen, 1971; Evans et al., 2021). Evans et al. (2021) also reported that there are 3-5 diamict layers present in the Smoking Hills region that display evidence of glaciotectonic deformation.

3.3. Climate and vegetation

There is no climate data available for the Smoking Hills region. Based on the 1991-2020 climate normal from Paulatuk (~120 km east of the Smoking Hills), Tuktoyaktuk (~220 km west of the Smoking Hills) and Inuvik (~270 km west-south-west of the Smoking Hills), the mean annual air temperature in the Smoking Hills is likely between -9.1 and -7°C with mean January temperatures between -25.8 and -24.7°C and mean July temperature between 10.3 and 14.2 °C (Environment and Climate Change Canada, 2024). The total annual precipitation is between 227 and 249.8 mm with approximately 63-78% falling as snow (Environment and Climate Change Canada, 2024).

Most of the study area is located north of the tree line, which extends furthest north along the Horton and Anderson River valleys. The southern most sampled site (the Anderson River Slump) was the only one located near the tree line and was therefore sparsely forested. The vegetation south of the tree line is dominated by spruce shrubs as well as willow and alder shrubs, whereas the rest of the study area is mostly covered by mixed tundra vegetation with low shrub tundra as well as tussocks, sedges and mosses. There are also some dwarf shrubs to the southeast of the study area (NWT Centre for Geomatics, 2021). According to Dyke et al. (2003), the Smoking Hills area has been covered by tundra vegetation since the retreat of the LIS, with herb tundra being slowly replaced by shrub tundra between 10,000 and 9000 ^{14}C yr BP (**Figure 6**; Dyke et al., 2003). A study done by Ritchie and Hare (1971) has also shown that forest tundra covered the Tuktoyaktuk Peninsula and Mackenzi Valley during the early Holocene (as early as 10,000 ^{14}C yr BP). All though their research did not extent to the Smoking Hills area, this biome could have extended further eastward to include part of the southern Smoking Hills (Ritchie and Hare, 1971; Dyke et al., 2003). Between 8000 and 7000 ^{14}C yr BP, part of the south-west region of the study area, was covered by forest tundra (Dyke et al., 2003) while boreal forest covered the Tuktoyaktuk Peninsula and the area just west of the Smoking Hills (Ritchie and Hare, 1971; Dyke et al., 2003). According to Dyke et al. (2003), the boreal forest did not reach the Smoking Hills during this period (**Figure 6**), although this may reflect an absence of measurements.

3.4. Permafrost and ground ice

Based on the climate and vegetation conditions, the Smoking Hills are in the continuous permafrost zone. The thickness of permafrost measured at the nearby Elf G-02 well near the Mason River is about 141 m (Hu et al., 2013). As far as we know, there are no studies that focused on the ground ice in the Smoking Hills region, but one of the most studied regions is just to the west of the Smoking Hills along the Yukon Coastal Plain and Mackenzie Delta region. There are also a few studies that investigated the massive ground ice from the hummocky moraines in the Bluenose Lake Moraine to the east (St-Onge and McMartin, 2002) and on the Wollaston Peninsula on Victoria Island to the north (Dyke and Savelle, 2000). In the Yukon Coastal Plains and Mackenzie Delta region, thick bodies of tabular massive ice are often found in Pleistocene-age sediments. Some are associated with ice segregation origin following the retreat of the LIS (Mackay and Dallimore, 1992; Rampton, 1998; Murton et al., 2004; Burn and Kokelj, 2009) or a buried glacial ice origin (Murton et al., 2004). Therefore, Murton (2005) suggested that the massive ice in the region can be categorized in one of three categories: (1) preglacial segregated massive ice that was deformed by a cold-based margin of the LIS, (2) buried glacial ice, and (3) post-glacial segregated massive ice. Ice wedges are also commonly found in this region, both in the uplands and in the lowlands (Mackay, 1995; Kokelj and Burn, 2004). So far, most ice wedges have been dated to the mid to late Holocene (Holland et al., 2020). However, Mackay (1995) has reported the presence of 50-60 truncated Late Pleistocene-aged ice wedges on the islands of the Mackenzie Delta. It was suggested that the growth of these ice wedges predated a Late Wisconsinan advance of the Laurentide Ice Sheet, and that permafrost has probably been present in this region since the Early Wisconsinan of even earlier (Mackay, 1972; Mackay and Matthews 1983). In the Smoking Hills region, the deformed ice wedges observed by Evans et al. (2021), could have either (i) formed prior to the Late Wisconsin glaciation, and been deformed by the advance of the LIS during the Late Wisconsin; or (ii) formed after the retreat of the LIS in the Late Wisconsin and been deformed by a re-advancement of the LIS during the deglacial period.

Since the area is ice-rich, numerous landforms associated with the degradation of permafrost are observed in the western Canadian Arctic. The most prominent ones are thaw slumps, and most of them are located along the maximum extent of the LIS or along ice-margin stillstands (Lacelle et al., 2015; Kokel et al., 2017).

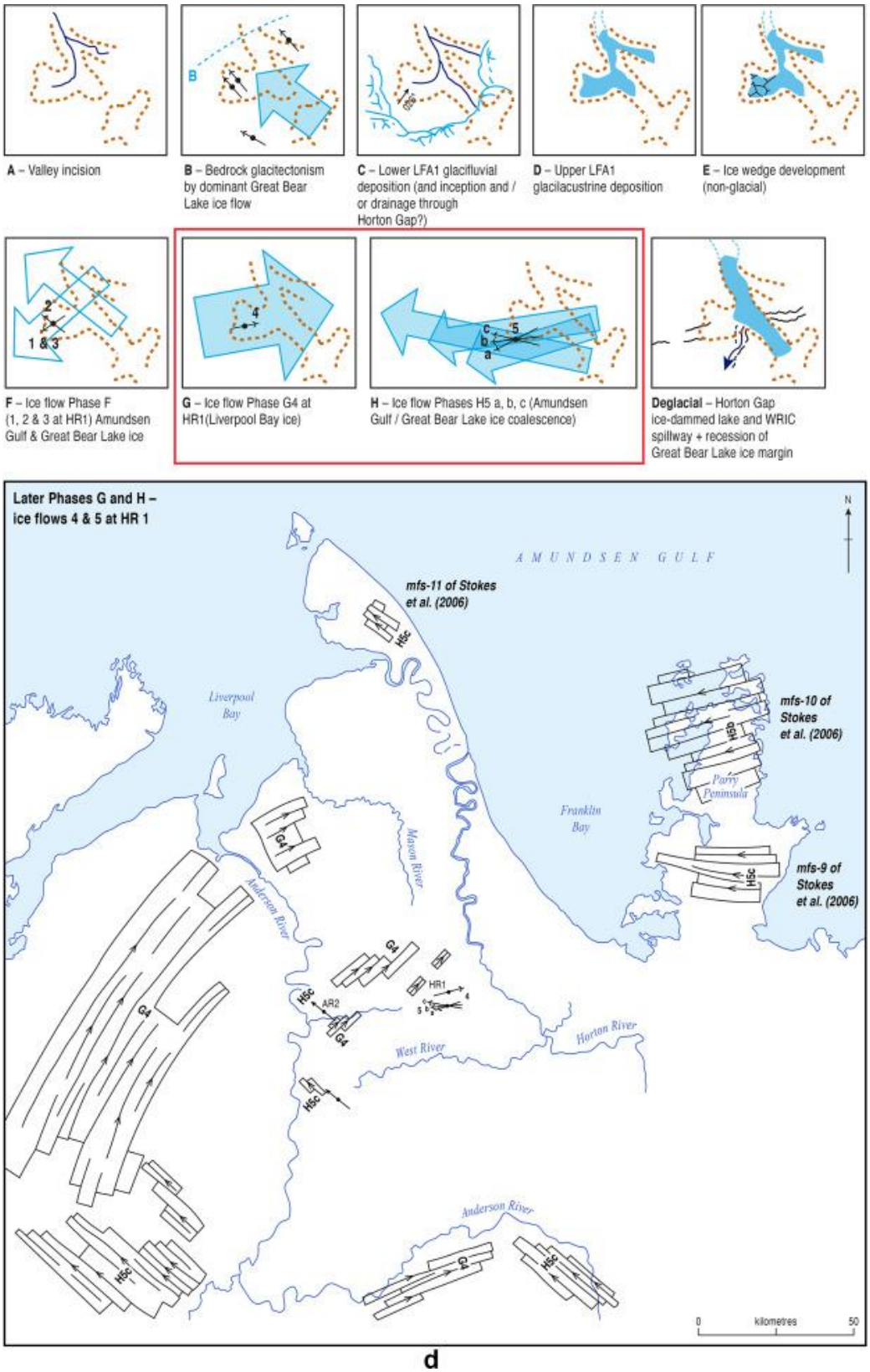

Figure 3. Paleogeographic event reconstructions of the local glacial history in the upper Horton River region based on glacial landforms. Taken from Evan et al. (2021).

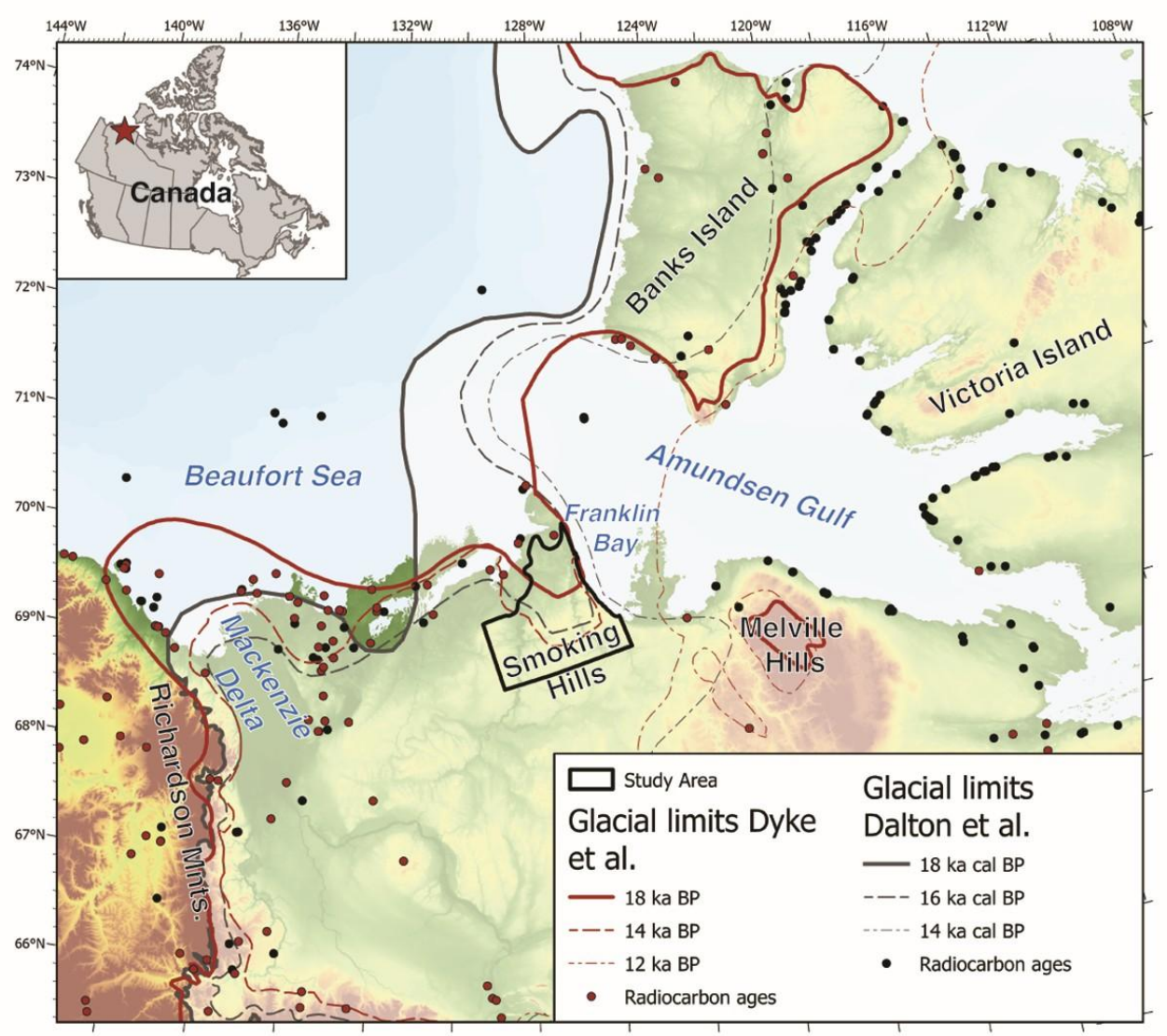

Figure 4. Glacial margins during the local glacial maxima and glacial retreat according to the models created by Dyke et al. (2003) and Dalton et al. (2023). Note that Dyke et al.'s dates are carbon dates which correspond roughly to the following calibrated ages: 21 ka cal BP (18 ka BP), 17 ka cal BP (14 ka BP) and 14 ka cal BP (12 ka BP).

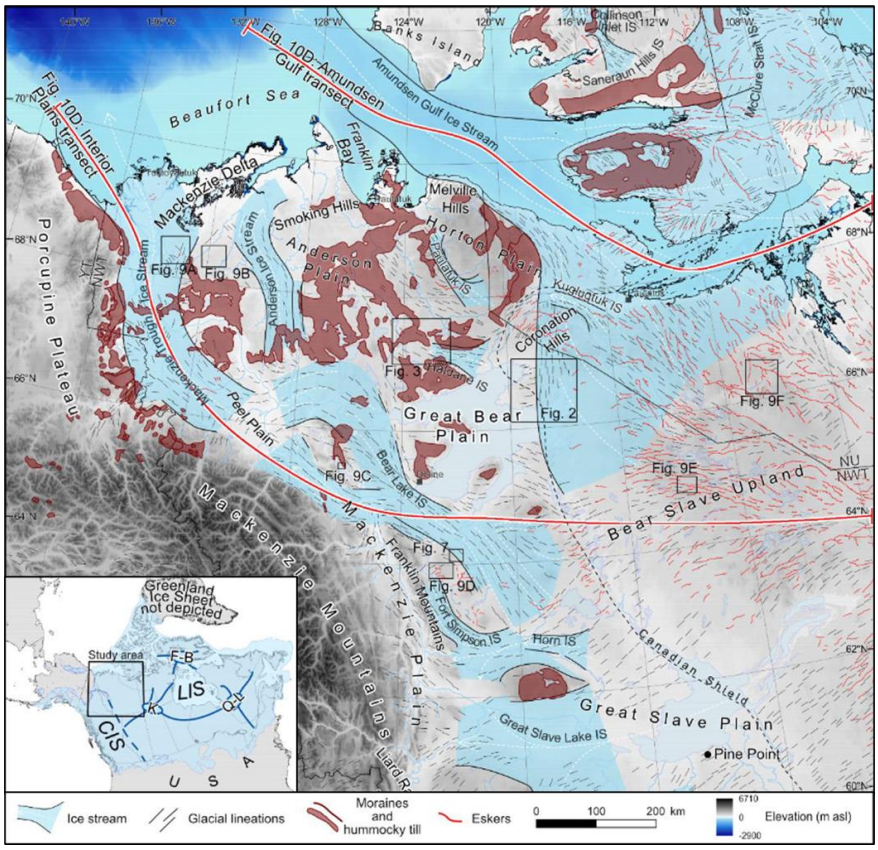

Figure 5. Northwestern LIS ice streams. Taken from Stoker et al., (2024).

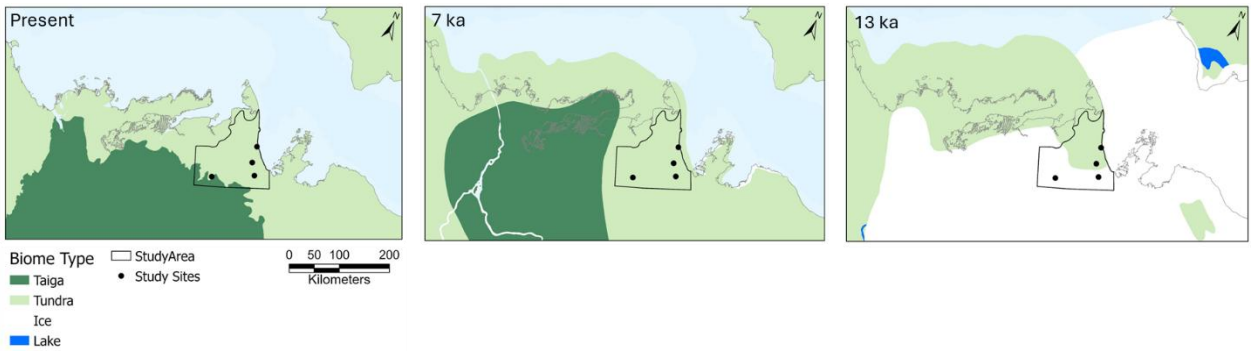

Figure 6. Biomes found within the western Canadian Arctic since the last glaciation. Based on the data from Dyke et al. (2003), Ecosystem Classification Group (2013) and Commission for Environmental Cooperation (2023). Note that the dates are presented in this figure are carbon ages.

4. Methods

4.1. Field sampling

Four sites were investigated to assess the origin and age of the tabular massive ice and ice wedges exposed in the headwall of RTS in the Smoking Hills region. The first site is the Anderson River slump (ARS; 68°56'59" N; 128°08'47" W), which was observed by Evans et al. (2021) in 2018. This RTS is located along one of the tributaries of the river after which it is named. It is the most southern site that was investigated and is located in an area of till veneer that is sparsely forested, probably just south of tree line. The second site (Franklin Bay slump; FBS; 69°40'31" N; 126°40'02" W) is located along the western coast of Franklin Bay. It is the most northern site and located in an area of gently to steeply slope terrain covered by a veneer to blanket of colluviated glacial sediments. It was selected because it was thought that it could potentially reflect the activity of the Amundsen Gulf Ice Stream. The third site (Coal River slump; CRS; 69°12'43" N; 126°18'52" W) was selected because it is in a thrust moraine belt in till blanket. Finally, the fourth site (Acid River slump; AcRS; 69°24'16" N; 126°36'52" W) was selected due to its isolated location in a veneer of colluviated glacial sediments and for the presence of ice wedges developed in tabular massive ice.

At each site (**Figure 1b**), Professor Lacelle, Dr. Smith and myself collected samples of permafrost, tabular massive ice and ice wedges from the headwall of the thaw slumps with the help of Professor Gosse and Kelly Ruben. Prior to sampling, the cryostratigraphy of the exposed headwall was described, photographed and sketched. Sampling was done using a Stihl BT 45 auger equipped with a core barrel measuring 30 cm in length and 6.5 cm in diameter or using an ice pick. Before taking the samples, 5-10 cm of the exposed ice or icy permafrost was removed with a pickaxe. Each ice wedge was sampled horizontally at three locations about 30-50 cm below their top, targeting the exposed edges and an approximate center, although deformation in some wedges meant that these designations were only nominally defined. The surrounding massive ice or icy permafrost was sampled at different depths, generally over a vertical transect of 1-2 m. Each ice sample was placed in a sealed clean plastic bag, allowed to partially melt and the first 50-100 ml of meltwater was discarded to further remove potential surface contamination. The rest of the ice samples was then completely melted and transferred to clean plastic bottles and the sediments within the ice were kept in the plastic bag for analyses. A total of 84 samples were collected,

including ice wedges (n=15), massive tabular ice (n=54), diamict layers (n=7) and other units (n=8) such as ice lenses, soils and organic material in the active layer.

4.2. Laboratory analyses

The sediments extracted from the melted ice samples were submitted to the Geological Survey of Canada (GSC) Sedimentology Laboratory. Samples were freeze-dried and then sieved by the team at the Sedimentology Laboratory and myself to isolate the <0.063 μm fraction for major, minor and trace element chemical analysis. The particle size distribution on the <2 mm sediment size fraction was determined using a laser particle size analyzer (Camsizer and Beckman LS13-320). The volume percentage of particles <2 mm was reported for sand (2-63 μm), silt (63-2 μm) and clay (<2 μm).

The sediment samples were then submitted to Activation Laboratories Ltd (Actlabs) for geochemical analysis. There, depending on sediment mass recovered, either 30 g or 0.5 g of the fine fraction (<0.063 μm) of sediments were digested with aqua regia (HCl + HNO_3) and heated until complete dissolution. Diluted HCl was then added to the solution to get 20 ml before being analyzed by inductively coupled plasma - optical emission spectrometer (ICP-OES) (cf., Zdanowicz et al., 2006). Analytical reproducibility is ± 5%.

The melted ice samples were kept cool and left undisturbed for several days to allow fine sediments to settle by sedimentation. I then filtered the meltwater in the laboratory with 0.45 μm quartz filters prior to analyses for major ions, stable water isotopes, dissolved organic carbon (DOC) and $^{14}C_{DOC}$. I prepared all the filtered melted ice samples before they were analysed by the geochemistry laboratory of the University of Ottawa to determine the concentration of major ions. Anions (Cl, SO_4, NO_3) were analyzed unacidified by Inductively Coupled Plasma Emission Spectrometry (ICP-ES). Cations (Ca, Mg, Na, Al, Ba, Fe, K, Mn, S, Si, Sr) were analyzed on samples acidified to pH 2 with 0.1 ml nitric acid by ICP-OES. Analytical reproducibility is ± 5%.

The concentrations of DOC and $\delta\ ^{13}C_{DOC}$ were analyzed at the Ján Veizer Stable Isotope Laboratory at the University of Ottawa. The concentrations of DOC and $\delta\ ^{13}C_{DOC}$ for were determined using an OI Analytical model 1030 wet TIC-TOC analyzer coupled with a model 1088 autosampler and interfaced to a Thermo Finnigan DeltaPlus XP IRMS via a Conflow 4 and following the method described by St-Jean et al. (2003). Analytical reproducibility for DOC and $\delta\ ^{13}C_{DOC}$ is ± 0.5 ppm and ± 0.2‰, respectively.

The $^{18}O/^{16}O$ and deuterium/hydrogen ratios (D/H) of the melted ice samples were determined using a Los Gatos Research liquid water analyzer coupled to a CTC LC-PAL autosampler for simultaneous $^{18}O/^{16}O$ and D/H ratio measurements of H_2O and verified for spectral interference contamination. The results are presented using the δ-notation ($\delta^{18}O$ and δD), where δ represents the parts per thousand differences for $^{18}O/^{16}O$ or D/H in a sample with respect to Vienna Standard Mean Ocean Water (VSMOW). Analytical reproducibility for $\delta^{18}O$ and δD are ± 0.3‰ and ± 1‰, respectively. D-excess ($d = \delta D - 8 \times \delta^{18}O$) was calculated following Dansgaard (1964).

Some samples of tabular massive ice and ice wedges were selected for $^{14}C_{DOC}$ measurements based on the DOC concentration and volume of meltwater available. The analysis requires a DOC concentration of ~1.0 mg C. When possible, two samples from each ice wedge were selected for measurements: one from the edge and one from the "centre". If the volume of meltwater from the edge sample was insufficient for $^{14}C_{DOC}$ analysis, the water from both sides of the ice wedge was combined. The $^{14}C_{DOC}$ measurements were performed at the A. E. Lalonde Accelerator Mass Spectrometer (AMS) Laboratory at the University of Ottawa, where I participated in the processing of the samples. There, the samples were acidified with 85% phosphoric acid to reach a pH <2 (Murseli et al., 2019). The samples were then sparged with He for 15 minutes before being heated for 1 hour at 60 °C and sparged again to discard any gases present in the headspace of the bottle (Murseli et al., 2019). The samples were then cooled to 4 °C and 8 ml of a $Na_2S_2O_8$ solution and 1 ml of 0.5 N $AgNO_3$ was added to the sample. The $Na_2S_2O_8$ solution serves as an oxidant, while the $AgNO_3$ serves as a catalyst to extract the CO_2 from the water (St-Jean, 2003; Lang et al., 2012, 2016; Zhou et al., 2015). The samples were then heated at 95 °for 1 hour and cooled to room temperature so that the CO_2 gets trapped in the headspace of the bottle. To extract and purify CO_2, the gas is put through a low-flow He carrier extraction line (Murseli et al., 2019) and the resulting CO_2 is stored in borosilicate breakseal containing 5-6 grains of silvered cobaltous / cobaltic oxide and baked at 200 °C overnight to eliminate any remaining sulfurous gases (Palstra and Meijer, 2014). The CO_2 samples were then converted to graphite through hydrogen reduction using a semi-automated graphitization line (St-Jean et al., 2017). The result is expressed in a fraction of modern carbon ($F^{14}C$), based on Reimer et al. (2004) calculations. The data is then background-corrected and corrected for spectrometer and preparation fraction based on the $^{13}C/^{12}C$ ratio measured by the AMS. The final result is reported in ^{14}C yr BP (BP = AD 1950) following Libby's half-life, as per Stuiver and Polach (1977). The errors for conventional

radiocarbon ages (^{14}C yr BP) are 1 σ and the F^{14}C uncertainties are below ±0.0061 (**Table 1**). The $^{14}C_{DOC}$ dates were also calibrated using the IntCal20 curve on OxCal v4.4.4 (Bronk Ramsey, 2009; Reimer et al. 2020; Bronk Ramsey, 2024). The calibrated ages of all melted ice samples were calculated using the lab reported uncertainties. However, the calibrated age ranges for the ice wedges samples were also calibrated using a ± 200 uncertainty representing the sample uncertainty. This was done due to the fact that each sample were around 10 cm wide which represents a growth period of approximatively 500 to 1000 years.

4.3. Data analysis

One of the questions this study is trying to answer is the origin of the massive ice exposed in the headwalls of RTS in the Smoking Hills. To do so, I analyzed the results of the stable water isotopes analysis ($\delta^{18}O$ and δD) and compared it with the data from different publications. For example, Lacelle et al. (2004) established that a low deuterium excess is typical for ice that melted and refroze. On the other hand, if the phase change occured in a closed system, the freezing process will preferentially use $\delta^{18}O$, leaving a decreasing amount in the residual water, which creates a gradual decrease of $\delta^{18}O$ in the ice. However, if the massive ice is predominantly composed of precipitation water that infiltrated the soil and froze under the active layer, the regression slope of $\delta^{18}O$ and δD will generally be around 6 due to isotope fractionnassions. On the contrary, the regression slope will be closer to the global meteoric waterline (8) if the source of water was unmodified precipitation, like what we would expect from a glacier (Lorrain and Demeur, 1985).

Another objective is to refine the permafrost and glacial history of the Smoking Hills region. This will be done using the $^{14}C_{DOC}$ dates as well as the stable isotopes and major ions result from different sampled units. The $^{14}C_{DOC}$ dates will allow us to better understand the timing and chronology of the events and link it to other studies. The stable isotope and major ion results will help us better understand the context of the formation of different ice units. Combined with the $^{14}C_{DOC}$ dates, this will help us better understand when the permafrost started to aggrade in this region and under what conditions. The presence of ice wedges, for example, does not only indicate that the region was unglaciated at the time of their formation, but also that the permafrost was likely continuous. The ice compositions could give us more information about the source of water that formed those wedges.

5. Results

5.1. Anderson River Slump

In 2023 the headwall of the ARS was about 6 m high and exposed three units (**Figure 7**). The active layer (unit 1) reached a thickness of approximately 40 cm (with an estimated maximum depth of 75 cm) and consisted of cryoturbated soils and organic material. The soils of the active layer were composed mostly of fine-grained sediments (75-78% silt), with only about 1% clasts (**Figure 11**). Unit 2 consisted of up to 3 m of icy diamict exhibiting various deformations and unconformities. This unit contained a veinlet over one of the sampled ice wedges. The icy diamict unit had coarser sediments, with 8-17% of clasts and the rest being less than 2 mm, of which 53-56% were silts and 29-34% were sand. Unit 3 rested bellow a thermal unconformity and exposed a layer of tabular massive ice that could be observed across the entire width of the headwall (>200 m long). The sediments within the massive ice were mostly smaller than 2 mm, with 5-13% of clasts, some of which were striated; silts comprised 57-61% and sand 21-26%. The tops of thermally truncated ice wedges were also visible within the massive ice, but the deformation observed by Evans et al. (2021) could not be seen, since the prominent ice wedges were mostly covered by the sediments which had accumulated in the slump floor since 2018. This means that only the uppermost 0.5-1.5 m of the ice wedges were exposed in 2023.

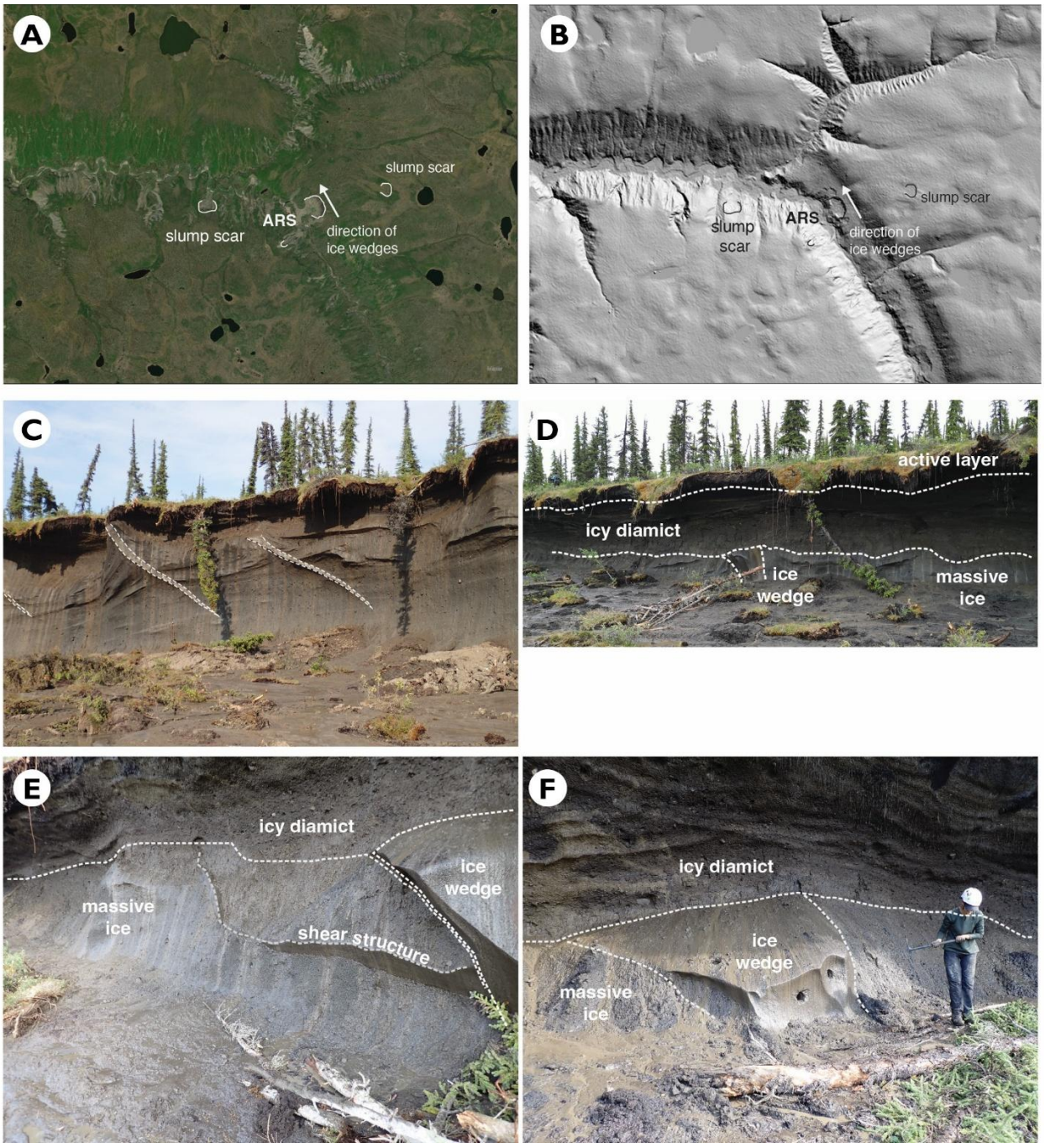

Figure 7. Anderson River slump headwall and sampled units. (a) Location of the ARS and other surrounding RTS as well the direction of deformation of the ice wedges. (b) Hillshade representation of the ARS showing the direction of deformation of the ice wedges which is parallel to the slope. (c) Section of the headwall from 2018 showing the deformed ice wedge and massive ice unit. (d) Section of the headwall showing the different units seen in 2023. (e) Details of the different units, including a glacial ice shear structure in the massive ice to the left of an ice wedge. (f) Sampled ice wedge and surrounding units; the holes near the top of the ice wedge show the location of two out of three ice cores.

5.1.1. Geochemistry of sediments

The major and minor element abundances determined from aqua-regia from the sediments in the active layer, diamict, massive ice and ice wedges are shown in **Figure 12a.** The sediments from the active layer often had lower major and minor ion abundance compared to the other units, except for K, which was higher, and Ba, which was similar to the other sampled units. The Ca, Mg, Na, Ba and K abundances were respectively 0.70%, 0.63%, 0.02%, 184.0 ppm and 0.63 ppm. The sediments from the diamict often had major and minor ion abundance in between the values found for the massive ice and ice wedge sediments. The Ca, Mg, Na, Ba and K abundances were respectively 2.55 ± 0.04 %, 1.22 ± 0.23 %, 0.02 ± 0.002 %, 171.50 ± 9.19 ppm and 0.20 ± 0.01 ppm. The sediments in the massive ice and ice wedge had similar Ca and K abundances, with 2.10 ± 0.41% and 0.27 ± 0.03 ppm, respectively for the massive ice, compared to 2.62 ± 0.20 % and 0.21 ± 0.02 ppm for the ice wedge. However, the massive ice had higher Na (0.04 ± 0.01% vs 0.02 ± 0.001%) and lower Mg (1.15 ± 0.10% vs 1.33 ± 0.01% relative), and Ba (125.41 ± 59.60 vs 202.00 ± 13.11 ppm) abundances compared to the ice wedges.

The chondrite-normalized abundance of rare earth element (REE) is presented in **Figure 12b**. For the sediments in the active layer, the diamict, the massive ice and ice wedges, there was a greater abundance of lighter REE (La-Sm) relative to heavier ones (Gd-Yb). La, Sm, Gd and Yb abundances for the active layer were 24.8 ppm, 5.6 ppm, 5.1 ppm and 1.5 ppm. The diamict had slightly lower abundance of La, Sm, Gd and Yb which were respectively 14.1 ± 0.5 ppm and 3.3 ± 0.4 ppm, 3.1 ± 0.2 ppm and 0.9 ± 0.0 ppm. The REE abundances in the massive ice were comparable to the diamict, with La, Sm, Gd and Yb abundances of 16.8 ± 1.1 ppm, 3.7 ± 0.2 ppm, 3.5 ± 0.2 ppm and 1.1 ± 0.1 ppm respectively. The ice wedges had lower concentrations of La, Sm, Gd and Yb, which were respectively 12.4 ± 1.1 ppm, 3.0 ± 0.3 ppm, 2.8 ± 0.1 ppm and 0.7 ± 0.1 ppm

5.1.2. Geochemistry of ground ice

The meltwater from the active layer was characterised by a Ca-SO_4 geochemical facies. The abundance of Ca, Mg, Na and K were 50.0 ± 23.5 mg/L, 25.0 ± 13.0 mg/L, 5.8 ± 2.5 mg/L and 5.0 ± 0.8 mg/L respectively. The abundance of SO_4 and Cl were 16.1 ± 5.0 mg/L and 3.3 ± 1.8 mg/L respectively. The meltwater from this unit had a $\delta^{18}O$ value of –23.7‰ and a mean deuterium-excess (*d*) of –2.9‰ (**Figure 13 and 14**).

The meltwater from the veinlet presents in unit 2 also had a Ca-SO_4 geochemical facies. The abundance of Ca, Mg, Na and K were 164.2 mg/L, 49.9 ppm, 33.3 mg/L and 16.8 mg/L, respectively. The abundance of SO_4 and Cl were 794.6 mg/L and 4.8 mg/L respectively. The veinlet had a mean $\delta^{18}O$ values of –23.7‰ and a mean *d* value of 2.9‰ (**Figure 13 and 14**).

The meltwater of the massive ice was characterized by a Na-SO_4 geochemical facies. Abundances of Na, Ca, Mg and K were 63.9 ± 15.2 mg/L, 30.2 ± 4.1 mg/L, 10.0 ± 1.7 and 14.1 ± 2.7 mg/L, respectively. Abundances for SO_4 and Cl were 95.1 ± 42.3 mg/L and 4.9 ± 2.8 mg/L, respectively. The massive ice unit had a mean $\delta^{18}O$ value of –28.9 ± 0.3‰ (**Figure 14)** and δD-$\delta^{18}O$ regression slope value of 9.7, which was slightly higher than that of the global meteoric water line, and a coefficient of determination (R^2) of 0.79. This unit had a mean *d* of -4.4 ± 1.4‰, a regression slope of 0.3 and a R^2 of 0.5 (**Figure 14**). The massive ice was of late Pleistocene age and yielded a $^{14}C_{DOC}$ age of 21,100 ^{14}C yr BP (**Table 1**).

The meltwater of four ice wedges had a Ca-SO_4 geochemical facies. Abundances of Ca, Mg, K and Na were 120.0 ± 30.7 mg/L and 15.8 ± 5.3 mg/L 7.3 ± 2.6 mg/L and 7.1 ± 3.6 mg/L, respectively. Abundances of SO_4 and Cl were 454.3 ± 124.8 mg/L and 4.8 ± 1.1 mg/L, respectively. The concentration of DOC had a mean value of 2.5 ± 1.1 mg/L and the $\delta^{13}C_{DOC}$ averaged –25.7 ± 1.2 ‰. The ice wedges had slightly lower $\delta^{18}O$ values (mean of –31.3 ± 0.5‰) than the enclosing massive ice, except for one (SUV23 005) which had higher values (average of –27.4 ± 0.1‰; **Figure 13 and 14**). All ice wedges at this site had a mean *d* of –1.5 ± 1.8‰ (**Figure 14**). The ice wedges that developed within the massive ice were all late Pleistocene age, ranging from 10,200 ^{14}C yr BP to 13,000 ^{14}C yr BP, corresponding roughly to the Bolling-Allerod and Younger Dryas (**Table 1**).

5.2. Franklin Bay Slump

The headwall of the FBS measured up to 9 m high and exposed 3 units (**Figure 8**). The active layer (unit 1) reached a thickness of about 35 cm and consisted mostly of fine-grained sediments, with only 0-1% clasts and the rest being smaller than 2 mm; of which 68-78% was silt and 15-26% was sand (**Figure 11**). Unit 2 consisted of 1 to 6 m of deformed icy diamict with ice lenses approximatively 50 cm thick. The diamict was composed of about 5% clasts and the rest was less than 2 mm, 52-58% of which was silt and 12-18% was sand.. Unit 3 exposed 1-5 m of foliated and deformed debris-rich ice. The sediments with the massive ice were mostly smaller than

2 mm, with only 8-15% being clasts. Silt comprised 35-54% and sand comprised 27-55%. Two ice wedges extended from near the base of the active layer through the diamict and into the top of the debris-rich ice (**Figure 8c**).

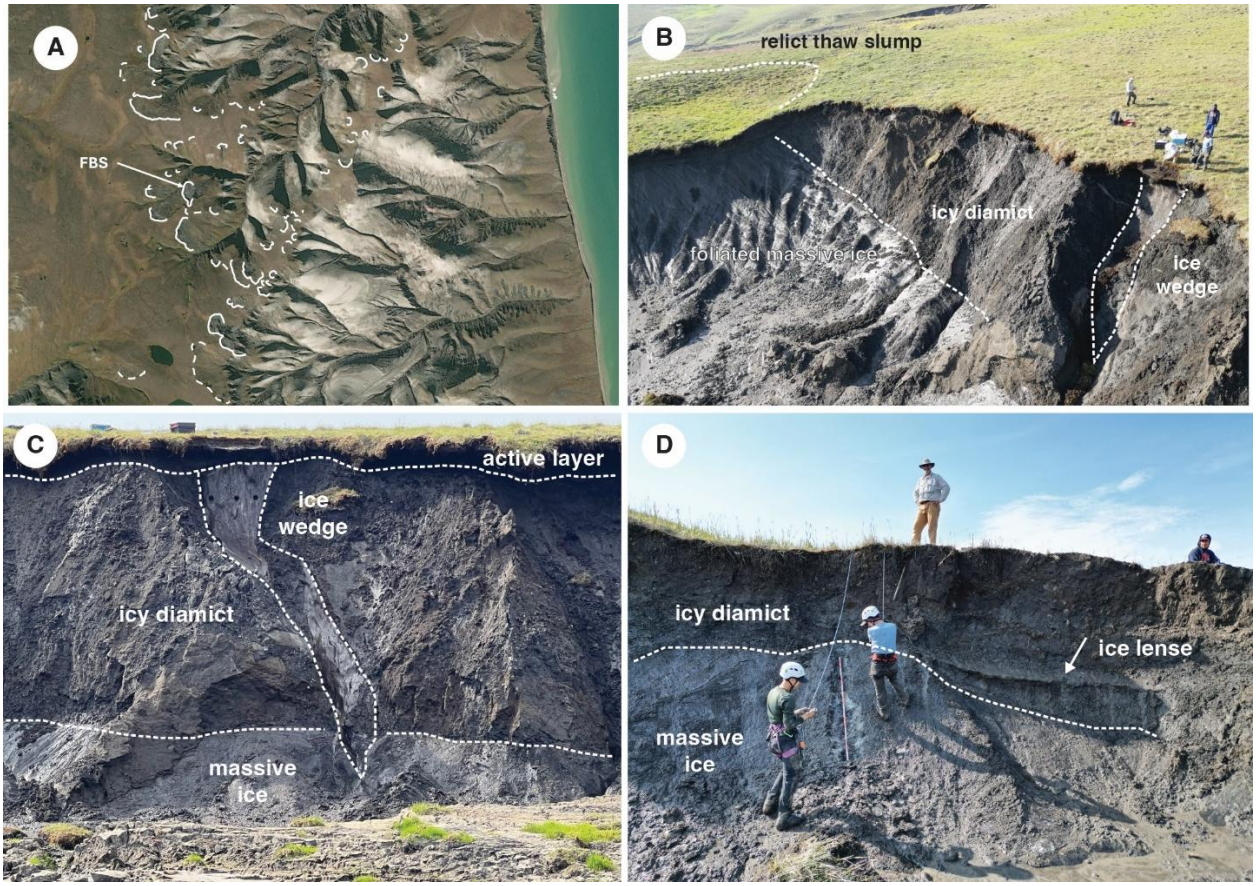

Figure 8. Headwall from the Franklin Bay slump. (a) Location of the FBS and other surrounding RTS. (b) Different units on the western headwall, including foliated massive ice extending under a relict thaw slump. (c) Different units on the southern headwall, including the sampled ice wedge. (d) RTS headwall approximately 50 m east (right) of the section shown in Figure 8b; Vertical profile taken from the massive ice unit under the 2 m tall stadia rod.

5.2.1. Geochemistry of sediments

The major and minor element abundances determined from aqua-regia from the sediments in active layer, diamict, massive ice and ice wedges are shown in **Figure 12a**. The sediments from the active layer typically had lower major and minor ion abundance compared to the diamict and massive ice units, except for the Ba abundance, which was higher than the diamict. The Ca, Mg, Na, Ba and K abundances for the active layer were respectively 0.81%, 0.51%, 0.01%, 0.2 ppm

and 162.0 ppm. The sediments from the diamict had Ca, Mg, Na, Ba and K abundances of 2.96 ± 0.77%, 1.99 ± 0.48%, 0.03 ± 0.01%, 44.63 ± 16.84 ppm and 0.25 ± 0.08 ppm, respectively. The sediments from massive ice had higher Ca (5.66 ± 3.22%), Mg (3.62 ± 2.08%) and Ba (130.08 ± 114.32 ppm) abundances, but similar Na (0.04 ± 0.04%) and K (0.28 ± 0.14 ppm) abundances.

The chondrite-normalized abundance of rare earth element (REE) is presented in **Figure 12b**. For both the sediments in the active layer, diamict and massive ice, there was a greater abundance of lighter REE (La-Sm) relative to heavier ones (Gd-Yb). The abundance of La, Sm, Gd and Yb, for the active layer sediments were 17.0 ppm, 3.4 ppm, 3.1 ppm and 1.1 ppm, respectively. The diamict had similar values which were respectively 17.9 ± 0.9 ppm, 3.8 ± 0.4 ppm, 3.5 ± 0.2 ppm and 1.1 ± 0.2 ppm. The sediments from the massive ice had slightly higher La and Sm abundances (17.9 ± 6.8 ppm and 3.8 ± 1.4 ppm, respectively), but similar Gd and Yb abundances (3.5 ± 1.2 ppm and 1.0 ± 0.3 ppm, respectively).

5.2.2. Geochemistry of ground ice

The meltwater from the ice lens formed above the massive ice had a Ca-SO_4 geochemical facies. The abundance of Ca, Mg, Na and K were 14.9 ± 12.6 mg/L, 2.9 ± 0.8 mg/L, 1.7 ± 1.1 mg/L, 1.6 ± 0.6 mg/L. The abundances of SO_4 and Cl were 34.3 ± 38.2 mg/L and 1.5 ± 1.0 mg/L respectively. The ice lens had a mean $\delta^{18}O$ of –24.7 ± 0.8‰ (**Figure 13 and 14**). This unit had a mean *d* of 11.0 ± 3.1‰ (**Figure 14**).

The meltwater from the sampled ice wedge was characterised by a Ca-SO_4 geochemical facies. The abundance of Ca, Mg, K and Na were 12.2 ± 1.6 mg/L, 6.1 ± 0.6 mg/L, 2.6 ± 0.3 mg/L, 2.1 ± 0.1 mg/L respectively. The abundance of SO_4 and Cl were respectively 22.6 ± 4.2 mg/L and 4.7 ± 0.8 mg/L. The sample had a concentration of DOC of 7.1 mg/L and a $\delta^{13}C_{DOC}$ of –26.3‰. The ice wedge had a mean $\delta^{18}O$ of –20.6 ± 0.1‰ (**Figure 13 and 14**). It also had a mean *d* of 4.6 ± 1.3‰ (**Figure 14**). The ice wedge was of Holocene age and yielded ^{14}CDOC ages between 2300 ^{14}C yr BP to 3000 ^{14}C yr BP (**Table 1**).

The meltwater from the massive ice unit had a Ca-SO_4 geochemical facies. Abundance of Ca, Na, K and Mg were respectively 14.6 ± 8.4 mg/L, 12.2 ± 13.4 mg/L, 6.3 ± 5.5 mg/L and 4.6 ± 2.6 mg/L. The abundance of SO_4 and Cl were 35.0 ± 32.5 mg/L and 0.6 ± 0.3 mg/L, respectively. The sample had a concentration of DOC of 2.4 mg/L and a $\delta^{13}C_{DOC}$ of –25.7‰. The mean $\delta^{18}O$ for the massive ice was –27.3 ± 0.4‰ (**Figure 13 and 14**) and the δD-$\delta^{18}O$ regression slope value of

11.6 which was higher than that of the global meteoric water line, and a R^2 of 0.77. This unit had a mean *d* of –1.3 ± 3.0‰, a regression slope value of 0.47 and a R^2 of 0.72 (**Figure 14**). The massive ice was of late Pleistocene age and yielded a $^{14}C_{DOC}$ age of 12,900 ^{14}C yr BP (**Table 1**).

5.3. Coal River Slump

The CRS is in an area with east-west aligned ice-thrust moraines, separated by elongated lakes. The headwall of the slump was about 3 m high and exposed 3 units similar to the ones observed at the Franklin Bay slump, but no ice wedges were exposed (**Figure 9**). Unit 1 was the 0.5 cm thick active layer (not sampled). Unit 2 consisted of a 1.3 m of icy colluvium and diamict. The sediments within this unit were almost exclusively sand and silt, with only 0-2% clasts and the rest being less than 2 mm, 37-40% of which was silt and 50-54% was sand. A discontinuous 0.6 m thick, clean ice lens was found beneath Unit 2. The lower unit (Unit 3) consisted of foliated debris-rich ice. The sediments within this unit were mostly composed of sand and silt, with up to 4% clasts. The rest were smaller than 2 mm, 15-53% of which was silt and 34-36% was sand (**Figure 11**). A wooden stick was discovered protruding within the lower sediment-rich massive ice unit.

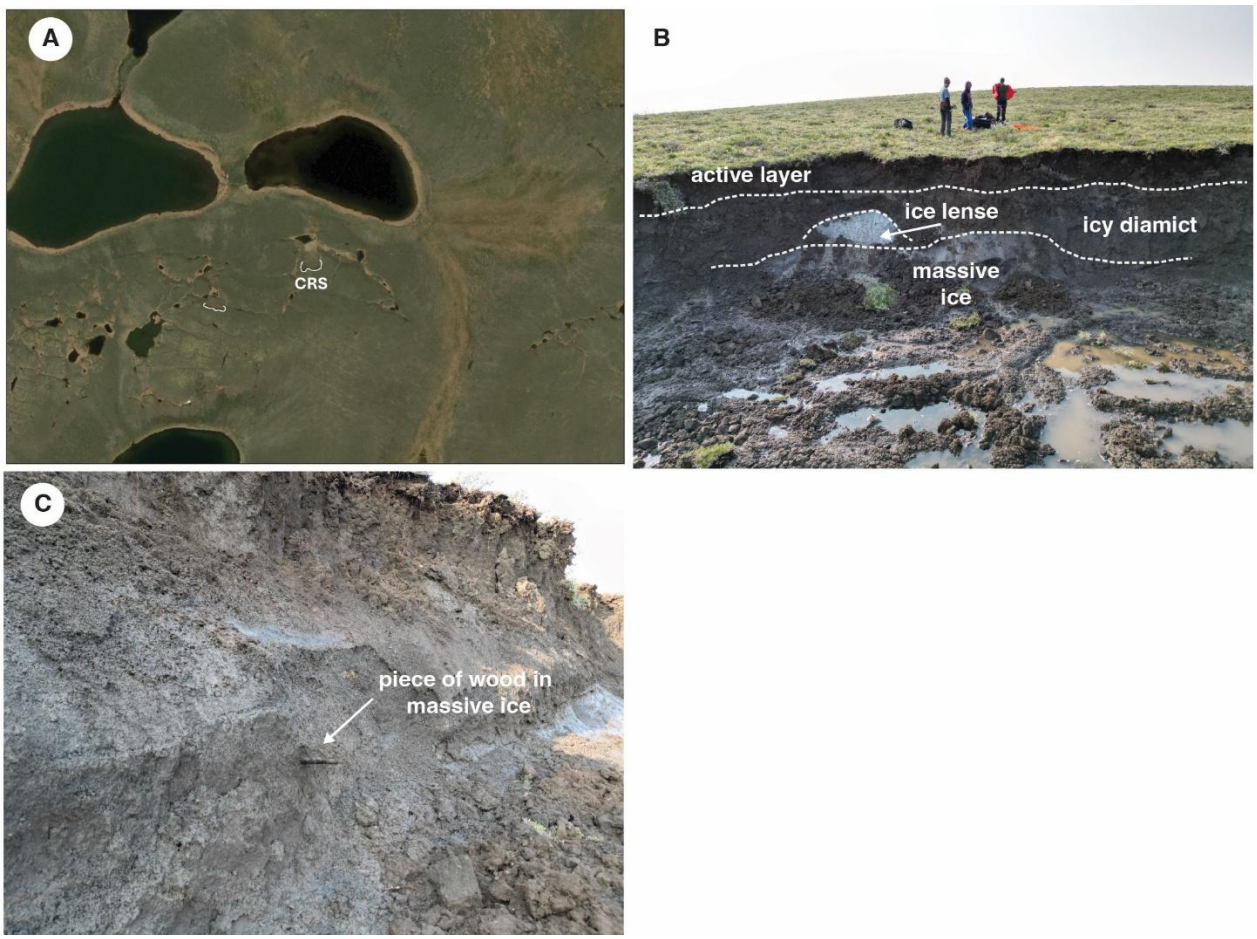

Figure 9. Headwall from the Coal River slump. (a) Location of the CRS and one other RTS. (b) Different sampled units on the 3 m tall headwall. (c) 20 cm long wooden stick protruding from the massive ice layer.

5.3.1. Geochemistry of sediments

The major and minor element abundances determined from aqua-regia from the sediments in the diamict and massive ice unit are shown in **Figure 12a**. The diamict had concentrations of Ca, Mg, Na, Ba and K of 5.69 ± 0.52%, 3.21 ± 0.37%, 0.01 ± 0.00%, 153.00 ± 22.63 ppm and 0.15 ± 0.02 ppm respectively. In comparison, the massive ice had concentrations of Ca, Mg, Na, Ba, and K of 4.27 ± 0.34%, 2.15 ± 0.34%, 0.02 ± 0.01%, 82.70 ± 49.78 ppm and 0.17 ± 0.07 ppm, respectively.

The chondrite-normalized abundance of rare earth element (REE) is presented in **Figure 12b**. For both the diamict and massive ice, there was a greater abundance of lighter REE (La-Sm) relative to heavier ones (Gd-Yb). In the diamict, the abundance of La, Sm, Gd and Yb were 13.2 ± 0.6 ppm, 2.9 ± 0.1 ppm, 2.7 ± 0.1 ppm and 0.8 ± 0.0 ppm. In the massive ice, the abundance

of La, Sm, Gd and Yb were 13.4 ± 1.4 ppm, 3.4 ± 0.3 ppm, 3.1 ± 0.4 ppm and 0.9 ± 0.1 ppm, respectively.

5.3.2. Geochemistry of ground ice

The meltwater of the pore ice in the diamict layer had a Ca-SO_4 geochemical facies. The abundance of Ca, Mg, Na and K were 47.1 ± 27.0 mg/L, 27.1 ± 18.0 ppm, 7.8 ± 5.8 mg/L and 5.2 ± 2.8 mg/L, respectively. The abundance of SO_4 and Cl were 205.5 ± 148.8 mg/L and 12.3 ± 10.2 mg/L respectively. The pore ice had a mean $\delta^{18}O$ values of -30.5 ± 0.6‰ and a mean *d* value of 2.5 ± 1.1‰ (**Figure 13 and 14**). This unit was of late Pleistocene age and yielded a $^{14}C_{DOC}$ age of 22,000 ^{14}C yr BP (**Table 1**).

The meltwater from the ice lens formed above the massive ice had a Ca-SO_4 geochemical facies and had similar major and minor ion abundances compared to the diamict. The abundance of Ca, Mg, K and Na were 7.4 ± 1.3 mg/L, 1.8 ± 0.5 mg/L, 1.1 ± 0.5 mg/L, 0.7 ± 0.3 mg/L. The abundances of SO_4 and Cl were 11.2 ± 1.1 mg/L and 0.8 ± 0.2 mg/L respectively. The ice lens had a mean $\delta^{18}O$ of –31.9 ± 0.7‰ (**Figure 13 and 14**) and the δD-$\delta^{18}O$ regression slope value of 7.5 which was near that of the global meteoric water line. This unit had a mean *d* of 1.4 ± 0.3‰ (**Figure 14**).

The meltwater from the massive ice unit also had a Ca-SO_4 geochemical facies and had similar major and minor ion abundance compared to the diamict. The abundance of Ca, Mg, Na and K were 60.3 ± 45.0 mg/L, 24.2 ± 25.8 mg/L, 16.8 ± 16.9 mg/L and 8.9 ± 5.4 mg/L. The abundance of SO_4 and Cl were 259.9 ± 308.5 mg/L and 21.7 ± 32.0 mg/L. The mean $\delta^{18}O$ value of the massive ice was –30.8 ± 0.2‰ and had a regression slope value of 9.6 with a R^2 value of 0.8 (**Figure 13 and 14**). It had a mean *d* of 1.8 ± 1.1, a regression slope value of 0.3 and a R^2 value of 0.5 (**Figure 14**). It contained a piece of wood that yielded a non-finite age (>44,880 ^{14}C yr BP).

5.4. Acid River Slump

The AcRS did not seem to have many other thaw slumps in its vicinity. The headwall exposed was about 15 m tall and exposed 4 units, including the active layer (unit 1) and an ice-rich diamict (unit 2; **Figure 10**). The upper 3-5 m of the diamict showed complex layering and deformation. This unit also contained an ice wedge that was partially melted from the bottom. Unit 3 was sediment-poor (<25% sediments) massive ice. The sediments within this unit were almost

exclusively sand and silt, with only 3-4% clasts. The rest were smaller than 2 mm, of which around 67% were silt and 18-23% were sand (**Figure 11**). Unit 4 was composed of clean massive ice with little sediments. Two ice wedges reaching up to 8 m deep developed within units 3 and 4 and did not appear to show any deformation. However, these were not sampled due to unsafe conditions.

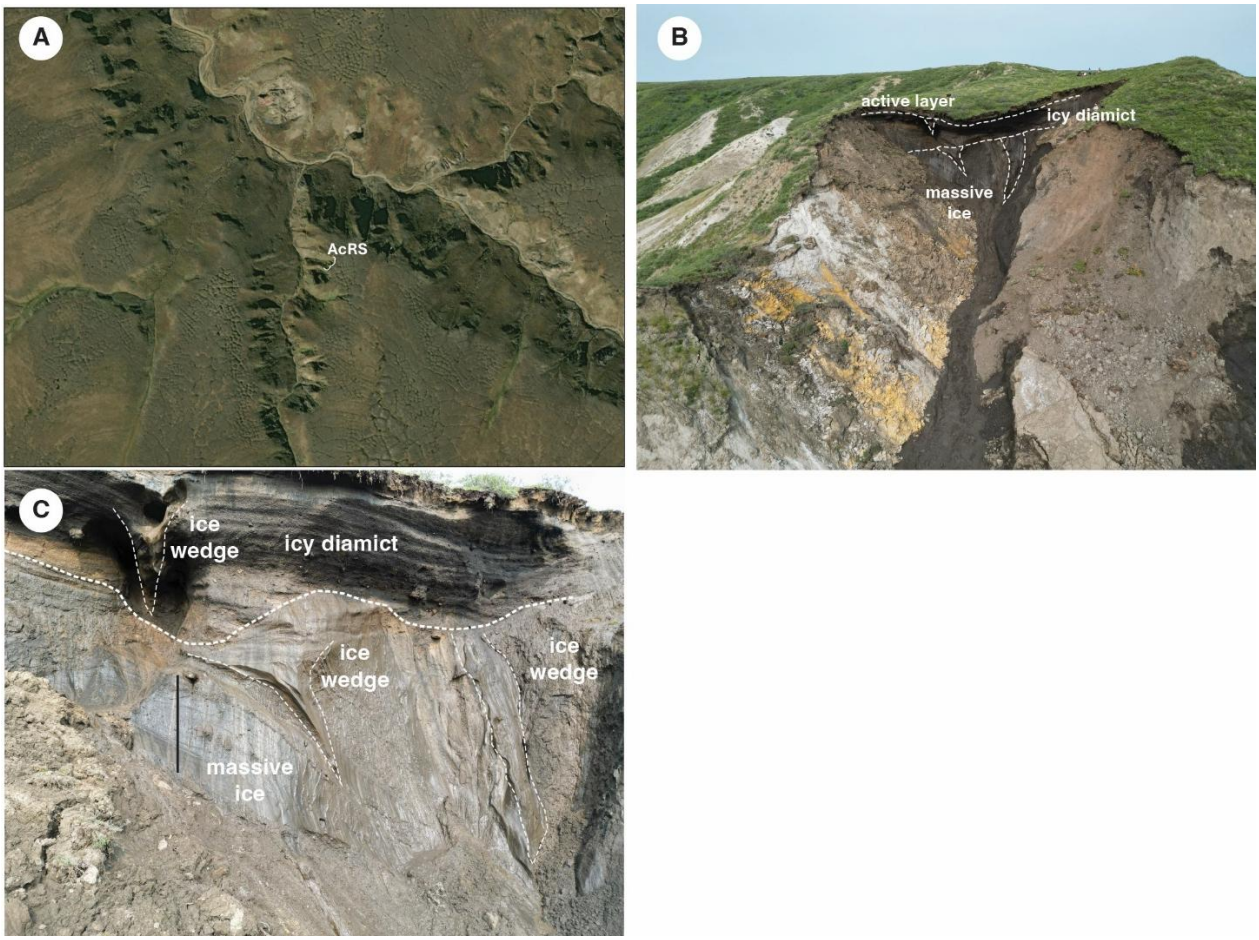

Figure 10. Headwall from the Acid River Slump. (a) Location of the AcRS near a tributary or the Horton River. (b) Headwall containing up to 15 m thick massive ice overlaid by diamict and poorly consolidated Smoking Hills Formation mudrock. (c) Detailed headwall showing an active ice wedge within a diamict layer measuring 3-5m in depth as well as the massive ice unit contains two older ice wedges. The location of massive ice sample 030 is indicated by the black line.

5.4.1. Geochemistry of sediments

The major and minor element abundances determined from aqua-regia from the sediments of unit 3 unit are shown in **Figure 12a**. It had concentrations of Ca, Mg, Na, Ba and K of 1.41%, 1.02%, 0.02%, 28.4 ppm and 0.18 ppm, respectively. Unit 4 had concentrations of Ca, Mg, Na, Ba and K of 1.70%, 0.95%, 0.03%, 23.6 ppm and 0.23 ppm, respectively.

The chondrite-normalized abundance of rare earth element (REE) is presented in **Figure 12b**. The sediments from the sediment-poor ice had a greater abundance of lighter REE (La-Sm) relative to heavier ones (Gd-Yb). The abundance of La, Sm, Gd and Yb, for the sediments in unit 3 were 19.2 ppm, 4.7 ppm, 4.0 ppm and 1.3 ppm, respectively. In comparison, the abundances of these ions in the sediments of unit 4 were 16.1 ppm, 3.6 ppm, 3.6 ppm and 1.2 ppm respectively.

5.4.2. Geochemistry of ground ice

The meltwater from unit 3 had a Ca-SO_4 geochemical facies. The abundance of Ca, Na, Mg, and K were 77.3 ± 21.0 mg/L, 49.7 ± 7.1 mg/L, 30.2 ± 7.3 ppm and 28.2 ± 7.6 mg/L respectively. The abundance of SO_4 and Cl were 474.7 ± 111.5 mg/L and 8.6 ± 2.6 mg/L respectively. This unit had a mean $\delta^{18}O$ of –28.1 ± 0.1‰ (**Figure 13 and 14**) and a mean *d* of 3.7 ± 0.6‰ (**Figure 14**).

The meltwater from one sample of massive ice from unit 4 also had a Ca-SO_4 geochemical facies but had lower major and minor ion abundance compared to the unit above. The abundance of Ca, Na, Mg, and K were 18.4 mg/L, 6.0 ppm, 7.8 mg/L and 7.8 mg/L, respectively. The abundance of SO_4 and Cl were 99.1 mg/L and 1.8 mg/L, respectively. The massive ice unit had higher $\delta^{18}O$ values (–25.9‰) compared to the overlying sediment-poor massive ice (**Figure 13 and 14**). It also had a lower *d* (0.4‰; **Figure 14**).

Table 1. Radiocarbon ages of ice wedges and massive ice samples taken from the Anderson River slump (ARS), the Franklin Bay slump (FBS) and Coal River slump (CRS).

Sample site and ID	Lab ID	Ice type	Age (^{14}C yr BP)	$F^{14}C$	Calibrated age range and probability (cal yr BP)	Median (cal yr BP)
ARS 002C	UOC-25119	Ice wedge (side)	12,050 ± 95	0.2242 ± 0.0026	13750-14160 (93.8%)	13,930
ARS 003	UOC-26609	Massive ice	21,100 ± 190	0.0725 ± 0.0017	25035-25840 (95.4%)	25,440
ARS 005B	UOC-26607	Ice wedge (centre)	13,000 ± 120	0.1987 ± 0.0028	15215-15920 (95.4%)	15,560
ARS 005C	UOC-25120	Ice wedge (side)	10,500 ± 50	0.2710 ± 0.0016	12440-12680 (80.1%)	12,540

ARS 007AC	UOC-25121	Ice wedge (both sides)	10,150 ± 50	0.2840 ± 0.0017	11600-11950 (90%)	11,780
ARS 009AC	UOC-25122	Ice wedge (both sides)	10,450 ± 70	0.2728 ± 0.0023	12040-12620 (94.4%)	12,345
FBS 015A	UOC-25123	Ice wedge (side)	2290 ± 35	0.7525 ± 0.0032	2300-2360 (54.3%)	2,310
FBS 015B	UOC-26608	Ice wedge (centre)	3040 ± 50	0.6851 ± 0.0042	3110-3370 (92.6%)	3,240
FBS 018	UOC-25124	Massive ice	12,900 ± 90	0.2015 ± 0.0021	15160-15690 (95.4%)	15,425
CRS 023	UOC-26610	Diamict	22,000 ± 280	0.0650 ± 0.0023	25830-27000 (95.4%)	26,280

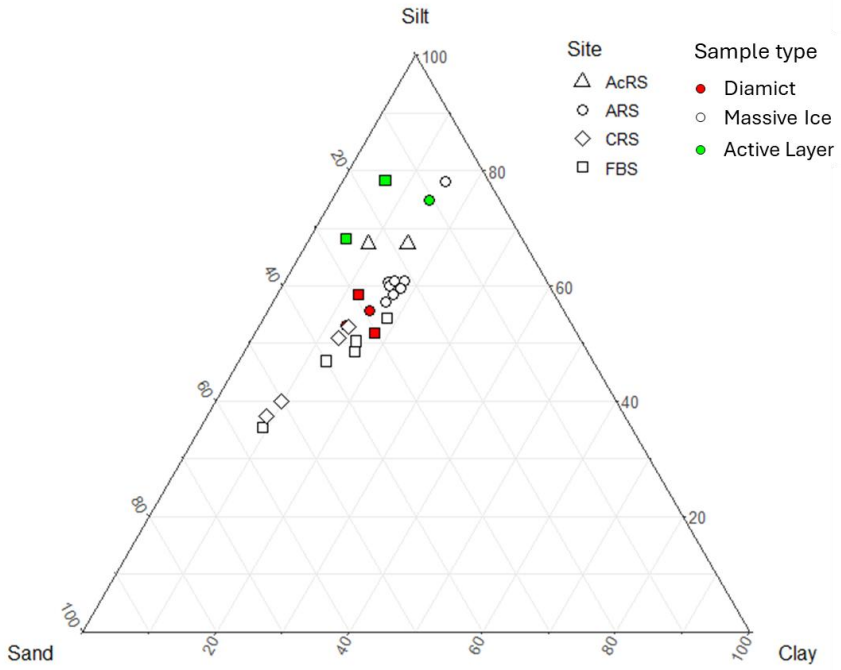

Figure 11. Volumetric percentage grain size of sediments smaller than 2 mm found in different samples taken at the Acid River slump (AcRS), Anderson River slump (ARS), Coal River slump (CRS) and Franklin Bay slump (FBS).

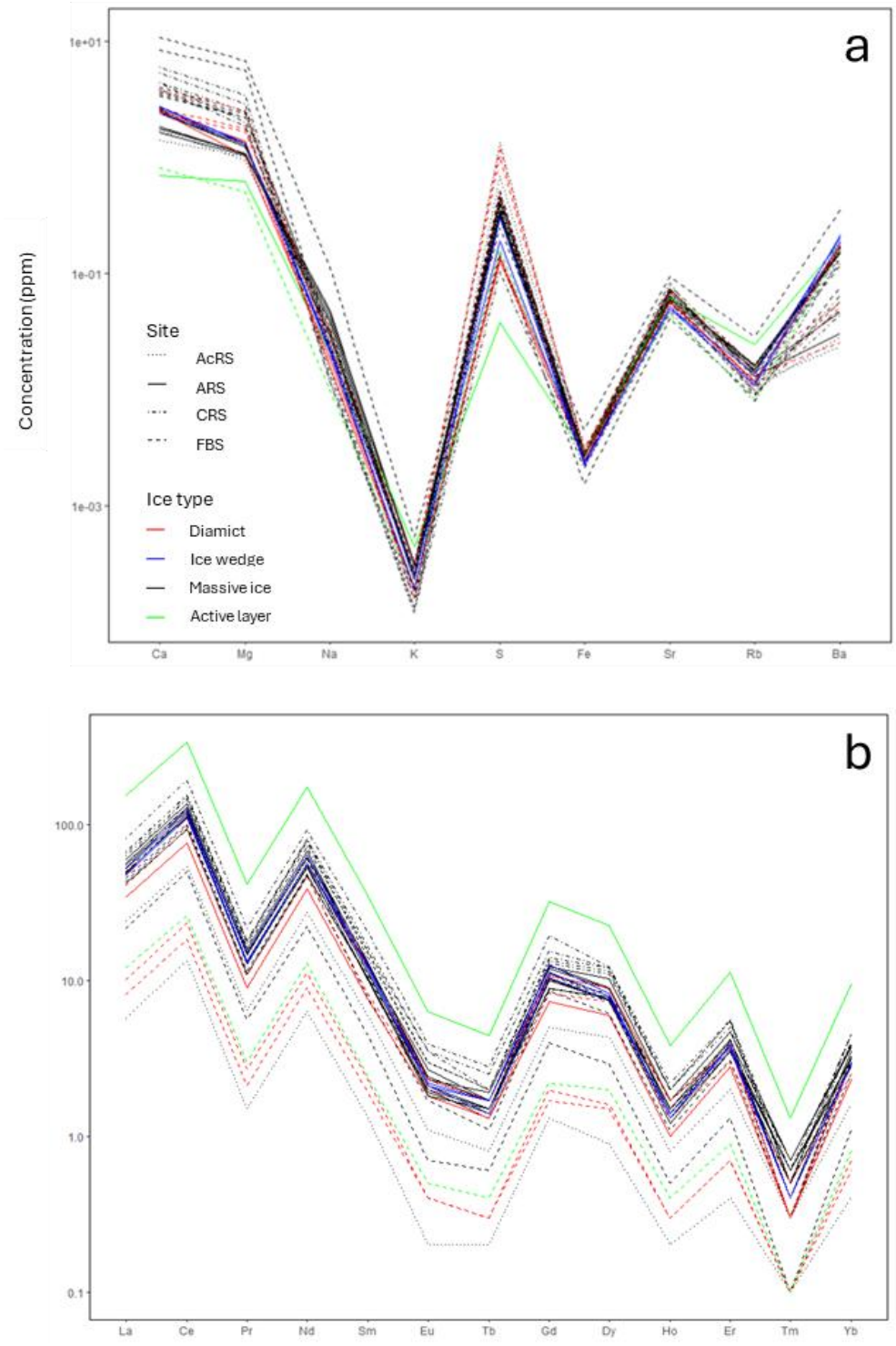

Figure 12. Abundances of major and minor elements (a) as well as Cadmium-normalized abundance of rare earth elements (b) within the sediments of different samples taken at the Acid River slump (AcRS), Anderson River slump (ARS), Coal River slump (CRS) and Franklin Bay slump (FBS).

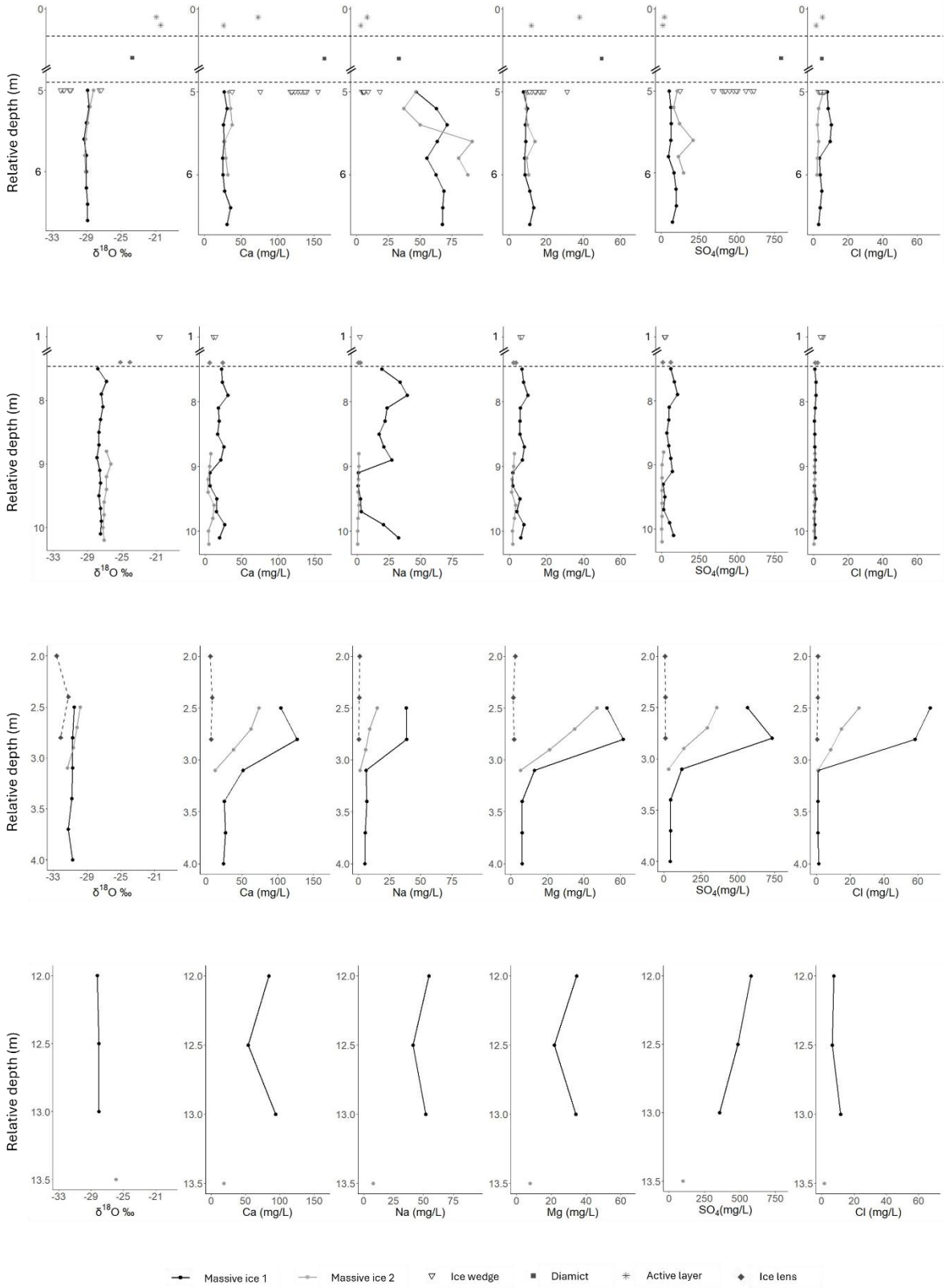

Figure 13. Biomes found within the western Canadian Arctic since the last glaciation. Based on the data from Dyke et al. (2003), Ecosystem Classification Group (2013) and Commission for Environmental Cooperation (2023). Note that the dates are presented in this figure are carbon ages.

6. Discussion

6.1. Origin of the tabular massive ice in the Smoking Hills.

As discussed earlier, based on previous work done by Evans et al. (2021), there are two main theories that could be used to explain the permafrost stratigraphy found at the ARS and the formation of deformed ice wedges and massive ice. The first one is that the massive ice is older than the last (Late) Wisconsinan glaciation, and the ice wedges formed during an interglacial period. They could then have been deformed by a glacial readvance during the Late Wisconsinan glacial period. The second hypothesis is that the ice wedges formed during the retreat of the LIS in the last glaciation and were later deformed by a readvance.

The massive ice units from the ARS, FBS as well as the pore ice from the diamict at the CRS were dated at around 25,400, 15,400 and 26,300 cal yr BP, respectively, which means that they were formed during the Late Wisconsin glaciation at the latest. The presence of an old piece of wood in the CRS massive ice as well at the other organic remains with non-finite age found in the area by Evans et al. (2021) could be explained by its inclusion in younger massive ice during its formation. The simplest was to explain the presence of older organic material in massive ice and the overlying sediments is if the organic material was incorporated in the LIS during its advancement and redeposited during its retreat. A study done by Lachniet et al. (2012) also documented the presence of older organic material that was included in younger ice. It is therefore likely that the age of DOC from melted massive ice is more accurate than the age of macro-organic matter, such as the pieces of wood found within it.

Many studies have shown that the characteristics of massive ice units can be used to infer their origins. For example, the presence of banded or foliated massive ice, such as the ones observed at the FBS and CRS, or sediment rich massive ice, such as the one observed at the ARS, is often indicative of buried glacial ice. This interpretation is further supported when the ice is also deformed (Lorrain and Demeur, 1985; French and Harry, 1990; St-Onge and McMartin, 2002; Ingólfsson and Lokrantz, 2003; Murton et al., 2004; Lacelle et al., 2004), as is the case at both the ARS and FBS. However, horizontal banding (or banding parallel to the contact with the overlying sediments) can also be associated with segregated massive ice (Mackay, 1971; Mackay and Dallimore, 1992). At the FBS site, the bands within the massive ice are clearly oblique to the sediment contact, supporting the interpretation that this ice is likely buried glacial ice. In contrast,

the evidence is less definitive at the ARS and CRS sites, since the ARS massive ice lacks visible banding, and the CRS ice exhibits banding that is not clearly oblique to the overlying sediments.

The nature of the contact between massive ice units and overlying sediments is another key indicator of their origin. An unconformable thaw contact, such as that observed at the ARS, is characteristic of buried glacial ice, whereas a conformable contact is indicative of segregated massive ice (Mackay and Dallimore, 1992; St-Onge and McMartin, 2002; Ingólfsson and Lokrantz, 2003; Murton et al., 2004; French, 2007). At the ARS, this thermal unconformity as well as deformation structures are found in both the massive ice and the enclosed ice wedges. In some cases, the deformation and sheer structures are continuous between the two units (**Figure 7**). Similar observations were made by Evans et al. (2021), who reported deformation of the thermal unconformity in 2018, including a discontinuity where the top of an ice wedge had been folded over the unconformity and another truncated ice wedge. Such features strongly suggest that the massive ice and ice wedges were both emplaced before the development of the thermal unconformity and that they were subsequently deformed at the same time. Evans et al. (2021) interpret this combination of features as evidence of a glacial advance or re-advance. Similarly, the massive ice units at the FBS and CRS also exhibit unconformable contact with the overlying sediments, which further support their interpretation of buried glacial ice.

This hypothesis is further supported by the differences in $\delta^{18}O$ values as well as water ion concentrations between the massive ice unit and the overlying units from the ARS, FBS and AcRS (**Figure 13**). The differences in $\delta^{18}O$ values indicate that the massive ice and the segregated ice from the overlying units originated from different water sources and did not freeze in a continuous manner. Such discontinuity is inconsistent with the formation of segregated massive ice (Mackay and Dallimore, 1992; Ingólfsson and Lokrantz, 2003; French, 2007). At the ARS, a notable difference in ion concentration (especially Ca, Mg and SO_4) between the massive ice and overlying diamict further indicates that both units come from distinct sources of water. At the FBS, the difference in water ion concentration between the massive ice and the overlying ice lens is less pronounced. Nevertheless, sediment ion ratios (Ca/K, Ba/Ca and Cs/K) in the overlying diamict at FBS are generally lower than those in the massive ice, which further supports the interpretation of different formation processes (**Figure 15**).

If the massive ice unit had formed through segregation, we would also expect the $\delta^{18}O$ values to change gradually due to the downward movement of the freezing front (Mackay and

Dallimore, 1992, Souchez et al., 2000; Ingólfsson and Lokrantz, 2003; French, 2007; Fritz et al., 2011). In such a scenario, the downward movement of the freezing front typically results in a closed system, where progressive freezing leads to the depletion of heavy isotopes in the residual liquid water (Souchez et al., 2000). However, the vertical $\delta^{18}O$ profiles of the four massive ice samples analyzed in this study do not exhibit such gradual changes. This absence of isotopic stratification suggests that the ice did not form under closed-system conditions and is therefore inconsistent with a segregated origin. It would also be important to note however, that the sampled vertical profiles were taken in deformed ice units, especially at ARS and FBS. As such the vertical profiles does not necessarily represent a chronological succession. The lack of gradual changes in $\delta^{18}O$ values with depth is therefore not conclusive in the cases of ARS and FBS massive ice samples.

However, the low $\delta^{18}O$ values of all the massive ice samples (-28.6 ± 2.7‰; **Figure 13**), which are amongst the lowest values found in this study along with the ARS ice wedges, would suggest that these units were formed in a cold environment, which likely corresponds to the Late Wisconsinan glacial period. Similar $\delta^{18}O$ values have been measured in massive ice units found in other areas within the western Canadian Arctic. Some have been attributed to buried glacial ice from the Late Pleistocene period (Lorrain and Demeur, 1985; French and Harry, 1990; Murton et al., 2004, 2005; Fritz et al., 2011; Lacelle et al., 2018; Coulombe et al., 2019), and others were associated with glacial meltwater (Mackay and Dallimore, 1992; Lacelle et al., 2004; Murton et al., 2004; Roy et al., 2023). More specifically, studies done by Murton et al. (2004, 2005) around Husky Lakes, Liverpool Bay, and Richards Island have revealed the presence of buried glacier ice with average $\delta^{18}O$ values ranging from -28.1 to -32.6‰.

The δD-$\delta^{18}O$ regression slope of all massive ice units is 7.7 (r^2 of 0.91), which closely approximates the GMWL (8), suggesting a predominantly meteoric origin. However, the variability in slopes from individual units of different RTS, along with the occurrence of unusually high slope values, renders the interpretations of site-specific origin inconclusive and is probably due to the mixing of more than one individual ice layer in many of the samples (Roy et al., 2023).

The *d* values for massive ice samples varied widely (from 4.3‰ to -7.3‰) and did not show a strong negative relationship between *d* and δD since it had a slope of 0.1 and a R^2 of 0.1. A strong negative relationship would have indicated the existence of a freezing slope, typical of water frozen under equilibrium conditions (Souchez et al. 2000; Lacelle et al. 2008; Fritz et al. 2011). On the contrary, the absence of a δD-*d* linear relationship implies that freezing either occurred under non-

equilibrium conditions (Michael et al., 2011) or involved the successive freezing of thin water layers in an open system, such as at the base of a glacier (Souchez et al., 2000). Since the values of *d* are also well below the GMWL (*d* = 10‰; **Figure 14**), it would suggest that the source of water that formed the massive ice units did not come directly from precipitation, such as what could be found in englacial ice. Instead, the water that formed the massive ice units was subject to preferential fractionation of heavy isotopes, which led to a lower *d* value. This could be explained by either a segregated-intrusive origin or basal-glacial origin (Lacelle et al., 2008). However, as shown earlier, the morphology of the massive ice units as well as the $\delta^{18}O$-δD profile (**Figure 13**), are inconsistent with a segregated origin. Furthermore, the massive ice found at the ARS, FBS and CRS have very similar physical characteristics to the buried glacial ice found in the Bluenose moraine, east of the Smoking Hills (St-Onge and McMartin, 2002), and what has been extensively observed along eastern Banks Island in the area of the Jesse moraine belt (Worsley, 1999; Vaughan et al., 2024;). We can therefore conclude that the sampled massive ice units from the ARS, FBS and CRS are likely buried basal glacial ice dating from the Late Wisconsin glaciation.

The clear massive ice (unit 4) at the AcRS slump seems to come from the same origin as the massive ice units from the other sampled sites, since it has similar $\delta^{18}O$ and δD composition and also has comparable ion concentration and ratios. However, more data would be needed to confirm this hypothesis, since only one sample was collected from this unit. The overlying sediment-poor massive ice (unit 3) had similar $\delta^{18}O$ values, which would suggest that it was formed in a similar environment. However, the particularly high water ion concentration, when compared to other massive ice units, would suggest that it might have a different origin, such as segregated glacial meltwater. The concentration of SO_4 is particularly high, especially when compared to the underlying pure ice, which had a much lower ion concentration. This sampled RTS was indeed close to bocanne sites and adjacent to a “red river” contaminated by the Smoking Hills Formation. It is therefore likely that the sediment-poor massive ice is of segregated origin, and its water chemistry was influenced by the local geological formation. However, more data would be needed to confirm this hypothesis.

6.2. Timing of growth of ice wedges and implications for glacial history in the Smoking Hills

The glacial and permafrost histories of the Yukon Coastal Plain and the Mackenzie Delta region are closely interconnected. Prior to the glacial advance over the region, permafrost was

present near the glacial margin (Mackay, 1971; Mackay, 1972). In the subsequent Late Wisconsinan, when the region was overridden by the LIS, the condition of the permafrost depended on the thermal regime of the ice: in areas with warm-based ice, permafrost likely would have thinned from the bottom up, potentially melting out completely (Rampton, 1988; Lacelle et al., 2013), whereas in areas with cold-based ice, it may have been preserved and deformed (Dyke, 1993; Dyke and Evans, 2003; Murton, 2005; Evans et al., 2018). Where degradation occurred, permafrost subsequently re-aggraded during or following glacial retreat (Rampton, 1988; Dyke and Evans, 2003). Similar to what was observed in 2018 in the Smoking Hills by Evans et al. (2021), there was a thermal unconformity above the deformed glacial massive ice in Tuktoyaktuk (Murton et al., 2004; Murton, 2005). However, contrary to the Smoking Hills, the ice wedges observed in the massive ice were not deformed, suggesting that they formed after the deformation and erosion of the underlying massive ice (Murton et al., 2004).

As discussed earlier, the massive ice sampled in this study is buried glacial ice dating back to 26,300 – 15,400 cal yr BP, which corresponds to the Late Wisconsin period (**Figure 16**) and are in accordance with the established LIS models (Bateman and Murton, 2006; Evans et al., 2021; Stoker et al., 2022; Dalton et al., 2023; Vaughan et al., 2024).

Since the growth of ice wedges require the presence of continuous permafrost, the ARS ice wedges that developed in buried glacial ice indicates that the permafrost aggraded sometime after the glacial retreat. Although this indicates that the climactic condition allowed for the preservation of buried glacial ice and its integration into the permafrost, it dose not indicate whether the permafrost aggraded immediately after the glacial retreat or shortly after.

The low $\delta^{18}O$ values of the ice wedges (-31.4 ± 0.6‰) also suggest that they were formed in a cold environment, likely corresponding to the Wisconsinan glacial period. As shown in **Figure 17**, many studies have also shown that the western Canadian Arctic was likely ice-free and had conditions favourable for permafrost growth during the glacial retreat. This includes vegetation dominated by tundra during the entirety of the deglacial period (Ritchie and Hare, 1971; Dyke et al., 2003), which is favourable to the development of continuous permafrost and ice wedges (French, 2007). A study done by Zazula et al. (2009) also shows that there were bison present in the Mackenzie Delta around 13,700 cal yr BP, which means that there were no glaciers covering the region at the time. These indicators collectively point to a period of deglaciation with favourable

conditions for permafrost aggradation and ice wedge development by the Bølling–Allerød interstadial at the latest.

Based on the $^{14}C_{DOC}$ dates, the 1.5 m wide ARS ice wedges developed over a 3000-year period. Since the frequency at which an ice wedge crack is highly variable, their ages and chronology cannot be estimated by counting the layers, as it is done for glaciers. Instead, Mackay (1974) suggests that the probability of cracking of an ice wedge follows a gaussian distribution and that the average with (μ) and standard deviation (σ) of ice wedges can therefore be used to calculate it.

$$[1] \qquad P = \frac{1}{\sigma\sqrt{2\pi}} e^{\frac{-(x-\mu)^2}{2\sigma^2}}$$

This equation can then be combined with the annual growth increment of ice wedge (ΔX, typically 1-5 mm) to estimate the number of years (T_{ij}) required to increase the width from X_i to X_j. The time required to grow ice wedge of a certain width is then determined by summing T_{ji}.

$$[2] \qquad T_{ji} = \frac{(X_j - X_i)}{\Delta XP_{ij}}$$

The time needed to form ice wedges up to 1.5m wide was assessed based on a cracking probability curve using average widths of 1.36 ± 0.55 m (n=4) and three possible growth increments (2, 2.5 and 3 mm). Based on these calculations, it would take 3500 to 2375 years to form the 1.5 m wide ice wedges found at the ARS. This fits within approximately 3000 years the time frame suggested by the $^{14}C_{DOC}$ dates.

6.3. Tilted ice wedges and a late re-advance of the LIS: an event postdating the record of local ice recession

After their formation, the ice wedges, along with the surrounding massive ice, were all deformed towards the northwest. The ARS headwall is parallel to the slope, and the ice wedges direction of deformation is oblique to the slope aspect (**Figure 7b**). This therefore excludes the possibility of a downslope deformation due to the growth of anti-syngenetic wedges. Evans et al. (2021) also note that there are pitted flutings in the vicinity of the ARS that represent a northwestern ice flow direction. The thermal unconformity, together with deformation patterns and ice flow indicators, supports the hypothesis of a glacial re-advancement that occurred either just before or

during the Younger Dryas. This event likely brought the Laurentide Ice Sheet over the Smoking Hills for a second time. As a result, ice wedge development was terminated, and the underlying permafrost was deformed.

We can therefore conclude that there was an active ice margin over the Smoking Hills region during the late Wisconsin deglacial phase. Using the more conservative calibrated age range based on the sample uncertainty (**Table 2**), the retreat of the LIS from the Smoking Hills happened before approximately 16182-15000 cal yr BP (**Table 2**), as indicated by the oldest ice wedge age. This aligns well with other glacial reconstructions (Bateman and Murton, 2006; Evans et al., 2021; Stoker et al., 2022; Dalton et al., 2023; Vaughan et al., 2024). However, the interruption of ice wedge development constrained by minimum radiocarbon ages of approximately 13,000-11,000 cal yr BP, provides more localized evidence for a glacial readvancement. This interpretation is supported by the presence of a thermal unconformity and the deformation features affecting both massive ice and enclosed ice wedges. Although a glacial re-advancement is not indicated in current reconstructions covering the Smoking Hills area, it cannot be ruled out given the sparse chronological framework and the potential for localized ice margin fluctuations that remain undetected at the regional scale. The glacial limits traces around the mainland Western Canadian Arctic also have high uncertainty relative to their ages as there are relatively few data points and the existing ones only provide minimum-limiting radiocarbon ages (Dalton et al. 2024). As shown in **Figure 18**, there are also very few radiocarbon ages from the Younger Dryas in the Smoking Hills and Mackenzie Valley areas. Furthermore, the glacial limits during the recession period around the study area are mostly based on chronological control from marine environments such as Banks Island and Victoria Islands which might not capture the terrestrial glacier dynamics.

These brief changes in the glacier's dynamics suggested by the deformation of the ARS ice wedges coincide with the collapse of the Amundsen Gulf Ice stream which happened after or around 13,000 cal yr BP (Lakeman et al., 2018; Stoker et al., 2025) and the growing importance of the Paulatuk Ice Stream and Bear Lake Ice Stream which have a northwesterly and westerly flow respectively. The northwesterly deformation of the ARS ice wedges may reflect the influence of the Paulatuk Ice Stream located to the southwest of the Smoking Hills area. Stoker et al. (2025) also suggest that the collapse of the ice saddle between the LIS and the Cordilleran ice sheet which happened before 14,000 cal yr BP followed by the changes in ice stream dynamics could have

caused temporary surge overprinting and stagnation over an extensive area. This could explain the deformation of ice wedges and massive ice at the ARS. The Thermal unconformity present above the massive ice and ice wedges could also be explained by a short glacial readvancement over the region, especially if the glacier was warmed based.

The changes in ice stream dynamics and the deformation of ice wedges at the ARS supports the idea introduced by Evans et al. (2021) that the deglaciation in the area was not a simple linear retreat but may have involved oscillations or localized re-advances, which are not usually captured in broader regional models (e.g., Stoker et al., 2022; Dalton et al., 2023). The ARS is in a region where we expect to have deformable beds beneath the LIS (Clark, 1994). The Pleistocene-age ice wedges at ARS are about 6-7 m below the surface and their tops likely moved horizontally about 5-7 m. Assuming that this deformation occurred in less than 1000 years, this means that the horizontal displacement was in the order of a few centimeter per year (at least 5-7cm/yr, and up to 50-70 cm/yr if it occurred over 100 years). This rate of deformation is modest suggesting the surface slope of the LIS in this area was low. It is unknown if this advance could have also reached the lower Horton River near the coastline and explain some of the tilted ice wedges in deformed glacial sediments that Mackay (1995) observed. Nonetheless, there is growing evidence of previously unknown short-lived glacial advance of the LIS within the Bölling-Alleröd and Younger Dryas interval. For example, in western New York State, Young et al. (2021) provided evidence from new ^{14}C and OSL ages in tills and ice-marginal deposits of a LIS advance during a general period of recession. These events are analogous to ongoing surging of some glaciers along the Greenland and Antarctic ice sheets (e.g. Joughin et al., 2010; Rignot et al., 2011). After the cold period of the Younger Dryas, temperatures rose rapidly, as evidenced by the sharp increase in $\delta^{18}O$ values recorded in the Agassiz and Greenland ice caps (Lecavalier et al., 2017; Vinther et al., 2009; **Figure 17a**). This warming led to the retreat of the Laurentide Ice Sheet from the Smoking Hills region, leaving behind the diamict that now overlies the deformed buried massive ice units, thereby contributing to their preservation. In those conditions, during the Hypsithermal, a shrub or forest tundra biome covered the region (Ritchie and Hare, 1971; Dyke et al., 2003). Evidence from the FBS site suggests that continuous permafrost and tundra vegetation were re-established in the area no later than 2,300–3,200 cal yr BP, and likely before 7,500 cal yr BP, as indicated by the widespread presence of similarly aged ice wedges in the Mackenzie Delta (**Figure 17e**; Holland et al., 2020). The relatively high $\delta^{18}O$ values of the FBS ice wedge (-20.6 ± 0.1‰) also suggest that

it was formed under warmer climatic conditions. This is consistent with other studies which have reported similar $\delta^{18}O$ values on modern ice wedges within the western Canadian Arctic (Lorrain and Demeur, 1985; Michel, 1990). The FBS ice wedge reaches the base of the modern active layer, indicating that it formed during the Holocene period and is likely still active.

Table 2. Radiocarbon ages of ice wedges samples taken from Anderson River slump (ARS) and Franklin Bay slump (FBS). The calibrated age ranges are calculates using both the laboratory uncertainty indicated in the "Age (14C yr BP)" column and the sample uncertainty which was estimated at ± 200.

Sample site and ID	Ice type	Age (14C yr BP)	Calibrated age range and probability (cal yr BP)	
			Laboratory uncertainty	Sample uncertainty (± 200)
ARS 002C	Ice wedge (side)	12050 ± 95	13750-14160 (93,8%)	14620-13497 (89,9%)
ARS 005B	Ice wedge (centre)	13000 ± 120	15215-15920 (95,4%)	16182-15000 (95,4%)
ARS 005C	Ice wedge (side)	10500 ± 50	12440-12680 (80,1%)	12830-11730 (95,2%)
ARS 007AC	Ice wedge (side)	10150 ± 50	11600-11950 (90%)	12488-11235 (94,1%)
ARS 009AC	Ice wedge (side)	10450 ± 70	12040-12620 (94,4%)	12760-11682 (94%)
FBS 015A	Ice wedge (side)	2290 ± 35	2300-2360 (54,3%)	2780-1822 (95,4%)
FBS 015B	Ice wedge (centre)	3040 ± 50	3110-3370 (92,6%)	3649-2759 (94,4%)

6.4. Chemistry of ice wedges

As shown by Grasby et al. (2018), the ponds found in the sediments of the Smoking Hills Formation have a significantly increased concentration of ions compared to ponds found in the Mason River Formation. Studies done by Sheath et al. (1982) shows that this is especially true for the concentration of SO_4 and, to a lesser extent, Na, Mg and Ca. If the ground ice at the sampled sites was affected by the shales from the Smoking Hills Formation, we would therefore expect

elevated SO_4 concentrations and ion ratios resembling those observed in the acid ponds studied by Sheath et al. (1982).

This pattern is indeed reflected in the ice wedge sampled at the FBS site, which is within the Smoking Hills Formation and near bocanne sites. The only notable exception was the Ca/SO_4, which was higher in the ice wedges than in the acid ponds (**Figure 19**). The relatively low ion concentration in the FBS ice wedge could be due the shallow active layer at the FBS (approximately 35 cm deep) which likely restricted the interaction between infiltrating precipitation and the mineral soil. As a result, water entering thermal contraction cracks may have undergone minimal chemical weathering, reducing the ion content of the wedge ice. The low concentration of dissolved ions, especially of Na and Cl (**Figure 20**), suggests that despite its proximity to the ocean, the water forming the FBS ice wedges is primarily derived from meteoric sources and shallow groundwater, rather than from marine aerosols (Holland et al., 2023).

In contrast, at the ARS, which is located near the limit between the Horton River and Smoking Hills Formations, the Pleistocene ice wedges exhibited distinct ion ratios when compared to the acid ponds. This is especially true for the Ca/Cl and Ca/Mg ratios, which are higher in the ice wedges (**Figure 19**). However, the low concentrations of Na and Cl and higher concentrations of Ca and SO_4 would suggest a groundwater origin (**Figure 20**). This geochemical signature may indicate that the influence of the Smoking Hills Formation was reduced or absent at the ARS during the Bølling–Allerød interstadial. Alternatively, the geochemical differences could be attributed to the ARS's location, which lies approximately 1 km south of the boundary of the Smoking Hills Formation (Okulitch and Irwin, 2017), potentially limiting its effects on ground water.

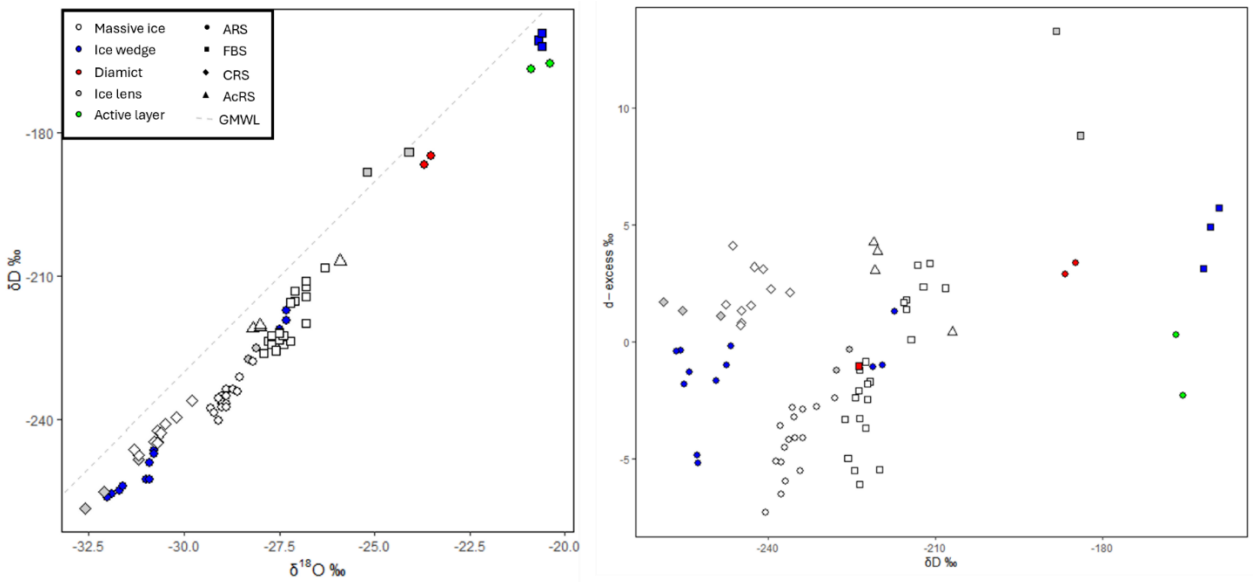

Figure 14. δD-$\delta^{18}O$ values (left) and relationship between δD and deuterium-excess (d) (right) of various ice samples from the tree sampled sites in the Smoking Hills, NWT. GMWL = global meteoric water line.

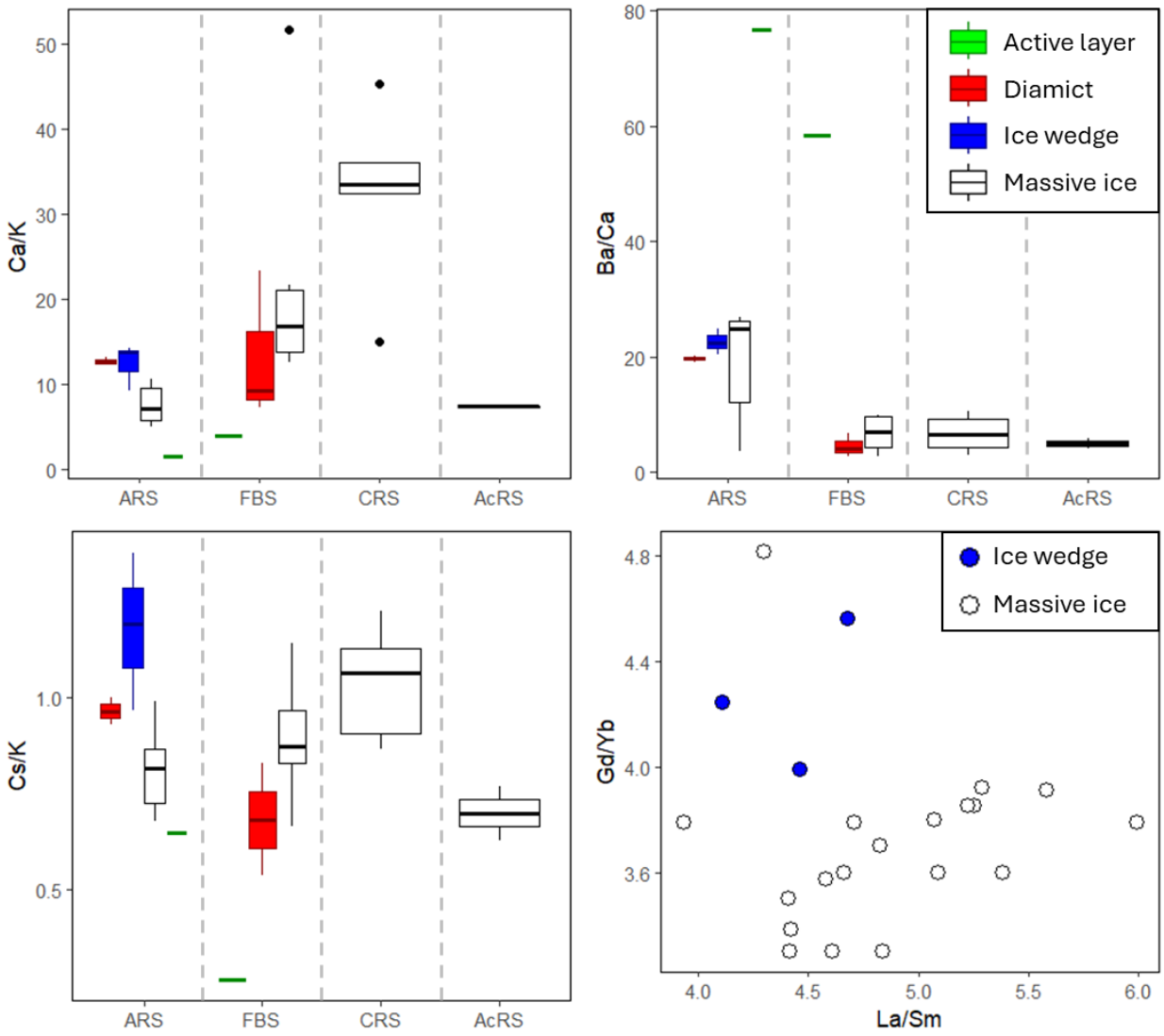

Figure 15. Trace element ratios found in the sediments of different samples taken at the Acid Anderson River slump (ARS), Franklin Bay slump (FBS), Coal River slump (CRS) and River slump (AcRS).

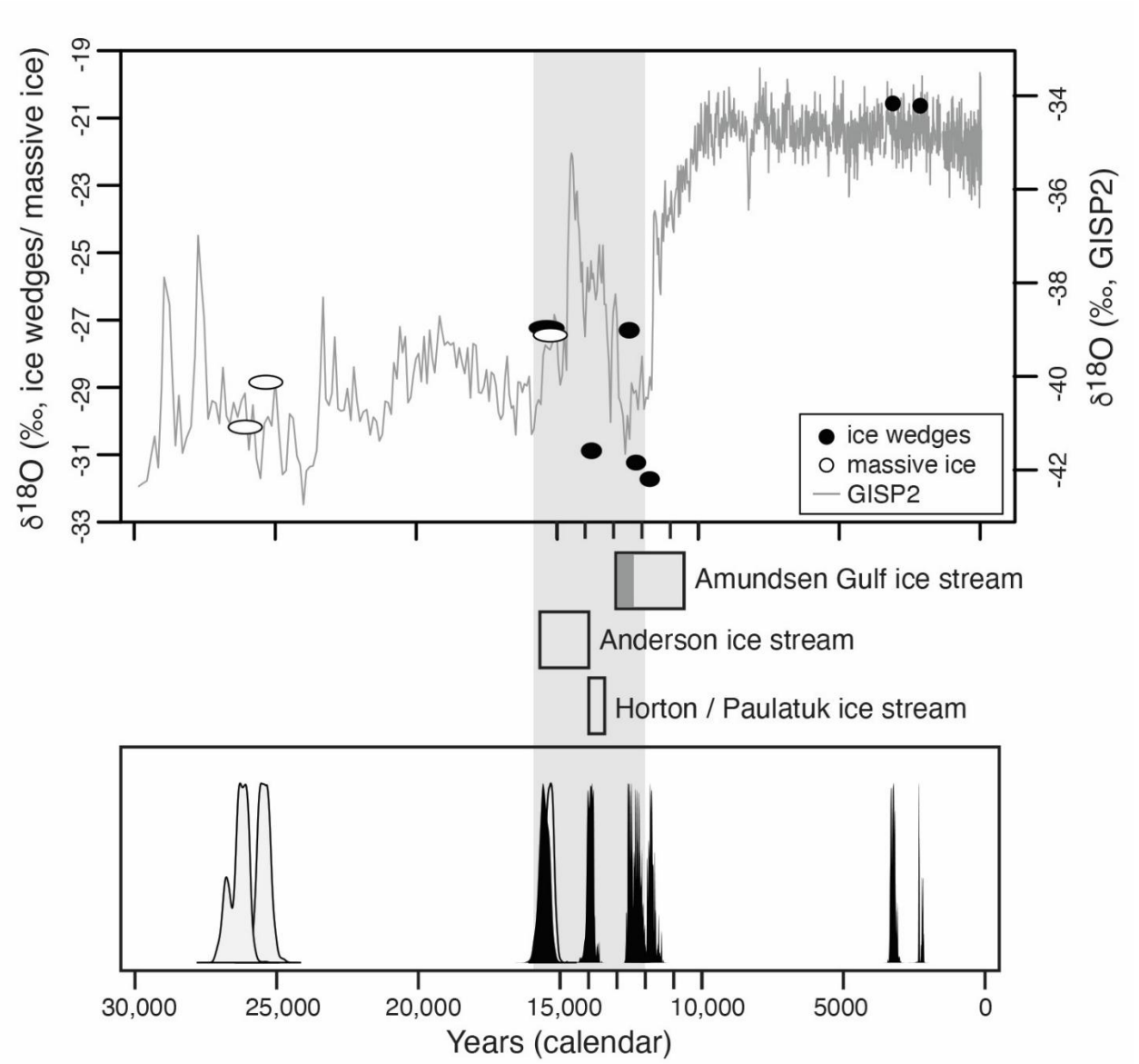

Figure 16. Calibrated age ranges and $\delta^{18}O$ values from the massive ice and ice wedges sampled at the four studied RTS compared to the $\delta^{18}O$ values of the GISP2 ice core. The white boxes represent the estimated end of each ice stream activity from Stokes et al. (2016) and the dark gray box represent the estimated end of the Amundsen Gulf ice stream based on Lakeman et al. (2018). The gray band represents the estimates period of ice wedge growth at the Anderson River Slump.

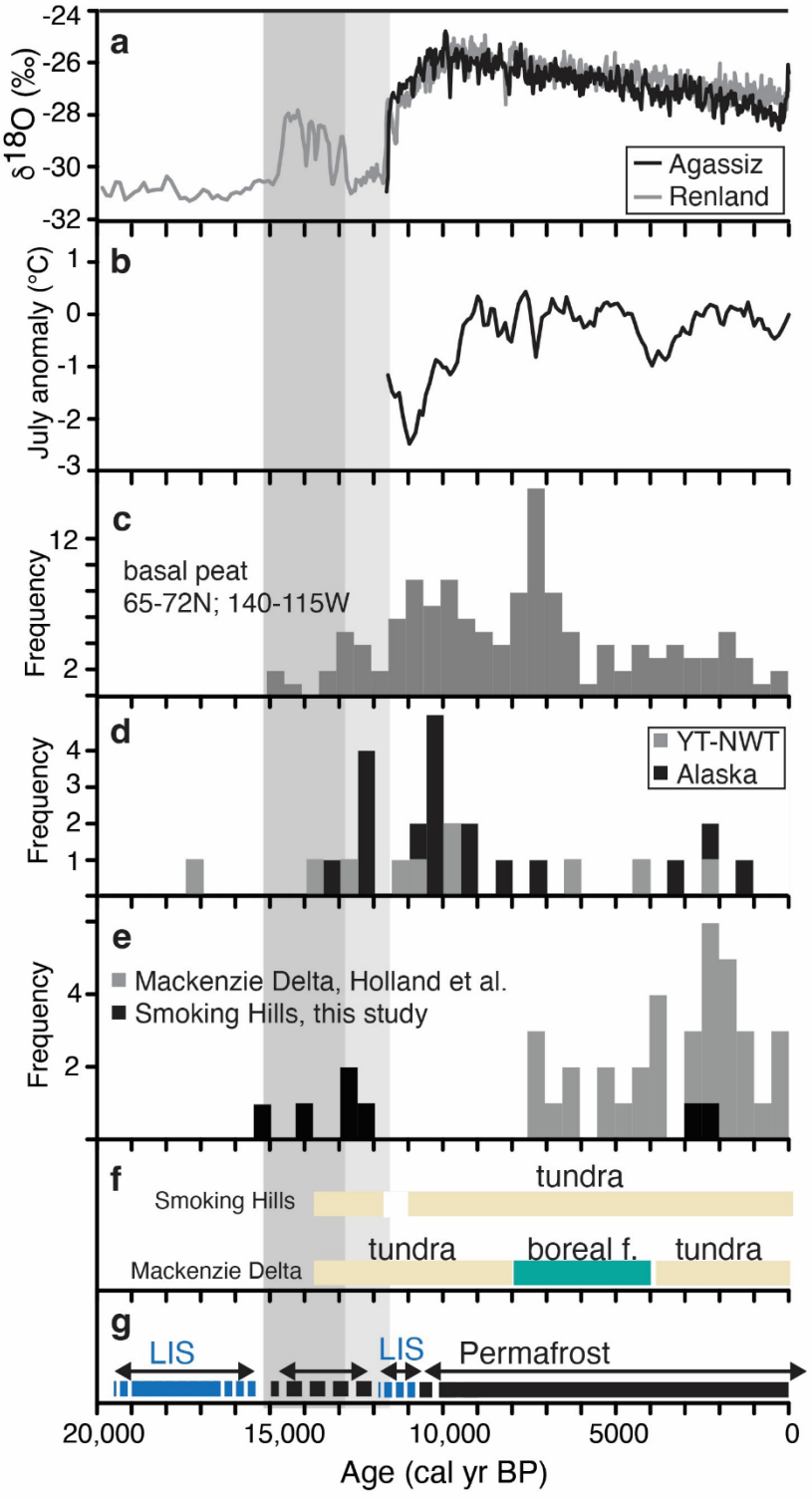

Figure 17. Reconstruction of paleo-environmental data in the Smoking Hills and MacKenzie Delta area since 20,000 cal yr BP. (a) $\delta^{18}O$ records from Agassiz Ice Cap (Ellesmere Island, NU, Canada; from Lecavalier et al., 2017) and Renland Ice Cap (Greenland; from Vinther et al., 2009). (b) July temperature anomaly for the Mackenzie Delta region (from Viau & Gajewski, 2009). (c) Frequency distribution of basal peat in northwestern Canada reflecting the presence of past vegetation (from Treat et al., 2017). (d) Frequency distribution of ^{14}C ages indicative of thaw lake initiation (from Walter et al., 2007). (e) Frequency distribution of ^{14}C ages from ice wedges indicating the presence of continuous permafrost (from Holland et al., 2020; this study). (f) Changes in distribution of biome in the study area (From Dyke et al. 2003). (g) Inferred presence of Laurentide Ice Sheet (LIS) and permafrost in the Smoking Hills area based on data shown in (a)–(g). The dark gray area represents the inferred presence of continuous permafrost and the period when Pleistocene ice wedges could have grown. The light gray area represents the inferred glacial readvancement period during the Younger Dryas.

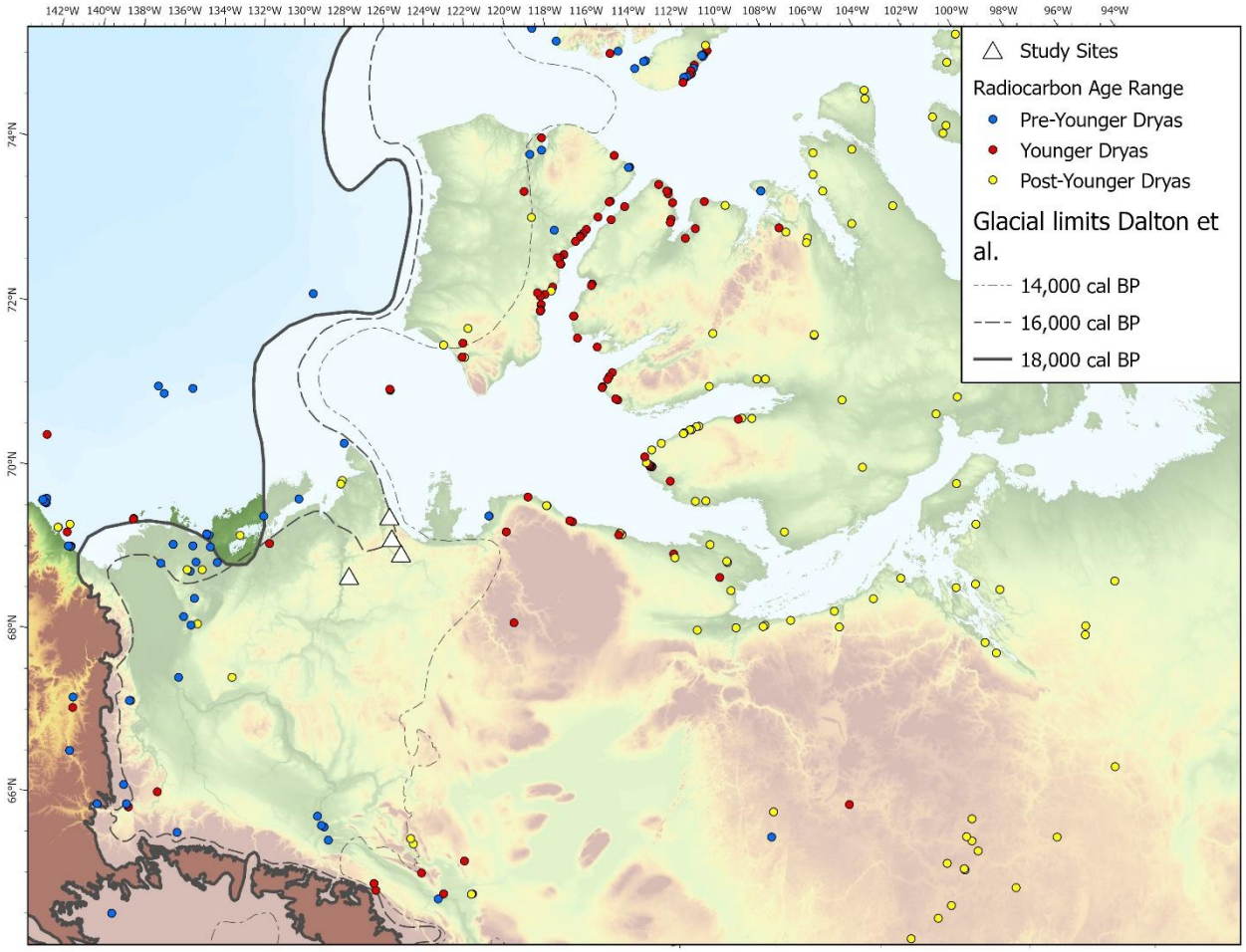

Figure 18. Radiocarbon ages in the northwestern Canadian Arctic grouped by age range. The data points are from Dalton et al. (2023) and Reyes et al. (2022). Note that Younger Dryas includes dates from 12,900 to 11,600 cal yr BP.

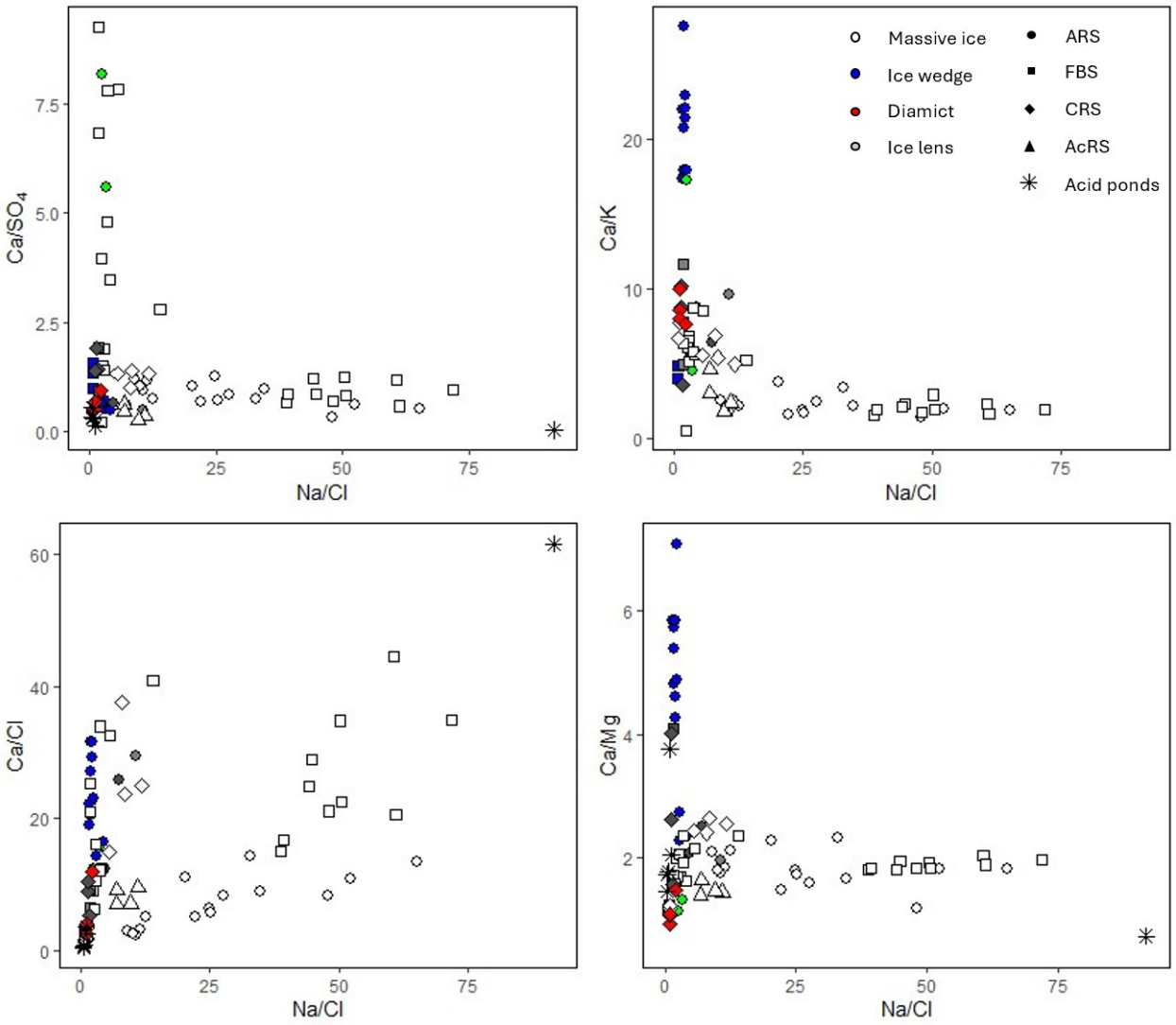

Figure 19. Molar ratios from meltwater samples of different ice types from the Acid Anderson River slump (ARS), Franklin Bay slump (FBS), Coal River slump (CRS) and River slump (AcRS).

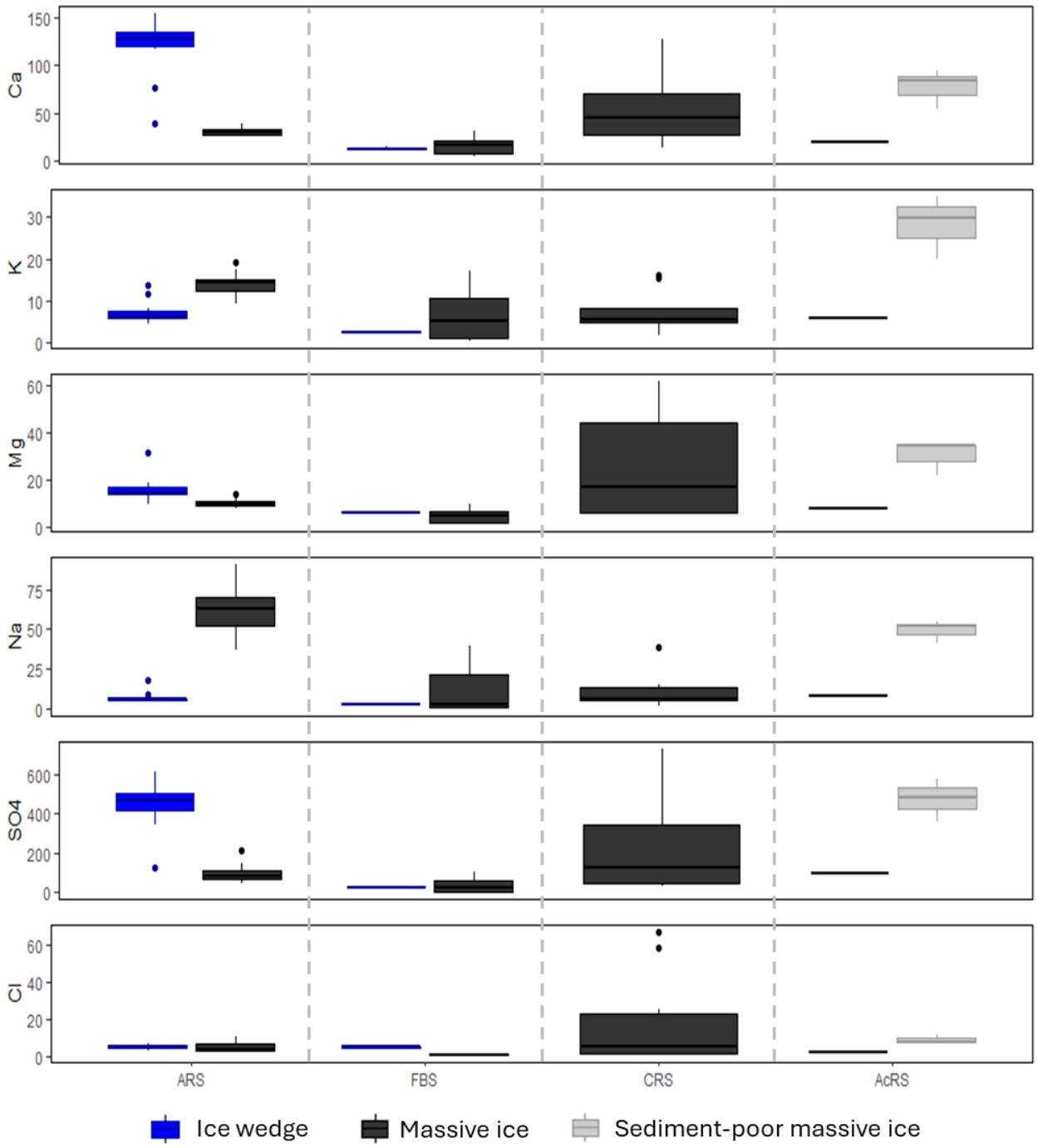

Figure 20. Ion abundances (in mg/L) from meltwater samples of ice wedges and massive ice from the Acid Anderson River slump (ARS), Franklin Bay slump (FBS), Coal River slump (CRS) and River slump (AcRS).

7. Conclusion

Based on the analysis of sediment and water geochemistry, stable water isotopes (δD-$\delta^{18}O$), $^{14}C_{DOC}$ age as well as the physical characteristics and stratigraphy of the different permafrost units observed on four RTS headwalls in the Smoking Hills region, we can draw the following conclusions:

1. The massive ice units sampled from the ARS, FBS, and CRS are buried glacial ice from the LIS, likely deposited during the Late Wisconsinan glaciation (26,300 - 15,400 cal yr BP). This is also supported by the presence of thermal unconformities, deformation structures, low $\delta^{18}O$ values, poor δD-d regression slope and abrupt isotopic changes between subsequent layers, which are inconsistent with segregated ice origin.
2. The clear ice unit at AcRS likely shares this origin, though data at this site is limited. However, the overlying sediment-poor ice unit may be segregated ice influenced by the Smoking Hills formation, based on its anomalously high SO_4 concentrations.
3. The presence of ice wedges (dated at 16,180 – 11,240 cal yr BP) within the massive ice at ARS indicates that the LIS retreated during the Bølling–Allerød interstadial, allowing for permafrost aggradation and ice wedge formation between approximately 16,000 and 11,000 cal yr BP.
4. The deformation of both massive ice and ice wedges at the ARS combined with the thermal unconformity and the ages of the ice wedges supports the hypothesis that the LIS re-advanced over the Smoking Hills region for a short period of time before or during the Younger Dryas period.
5. Holocene ice wedges developed at the FBS indicate post-glaciation permafrost aggradation, which is consistent with data from the Mackenzie Delta.
6. The chemical composition of ground ice (especially SO_4, Na, Ca) varies by location and age. While modern ice wedges at FBS show ion ratios resembling those from acid ponds near active bocannes, older ice at ARS shows no clear geochemical signature of bocannes influence. This could be due to either its location or the time of formation.

References

Bateman, M. D., & Murton, J. B. (2006). The chronostratigraphy of Late Pleistocene glacial and periglacial aeolian activity in the Tuktoyaktuk Coastlands, NWT, Canada. *Quaternary Science Reviews*, *25*(19), 2552–2568. https://doi.org/10.1016/j.quascirev.2005.07.023

Batchelor, C. L., Dowdeswell, J. A., & Pietras, J. T. (2013). Variable history of Quaternary ice-sheet advance across the Beaufort Sea margin, Arctic Ocean. *Geology*, *41*(2), 131–134. https://doi.org/10.1130/G33669.1

Batchelor, C. L., Dowdeswell, J. A., & Pietras, J. T. (2014). Evidence for multiple Quaternary ice advances and fan development from the Amundsen Gulf cross-shelf trough and slope, Canadian Beaufort Sea margin. *Marine and Petroleum Geology*, *52*, 125–143. https://doi.org/10.1016/j.marpetgeo.2013.11.005

Boulton, G. S., & Caban, P. (1995). Groundwater flow beneath ice sheets: Part II — Its impact on glacier tectonic structures and moraine formation. *Quaternary Science Reviews*, *14*(6), 563–587. https://doi.org/10.1016/0277-3791(95) 00058-W

Bronk Ramsey, C. (2009). Bayesian analysis of radiocarbon dates. Radiocarbon, 51(1), 337–360.

Bronk Ramsey, C. (2024). *OxCal*. https://c14.arch.ox.ac.uk/oxcal/OxCal.html#

Burn, C. R. (2000). The thermal regime of a retrogressive thaw slump near Mayo, Yukon Territory. *Canadian Journal of Earth Sciences*, *37*(7), 967–981. https://doi.org/10.1139/e00-017

Burn, C. R., & Kokelj, S. V. (2009). The environment and permafrost of the Mackenzie Delta area. *Permafrost and Periglacial Processes*, *20*(2), 83–105. https://doi.org/10.1002/ppp.655

Burn, C. R., Lewkowicz, A. G., & Wilson, M. A. (2021). Long-term field measurements of climate-induced thaw subsidence above ice wedges on hillslopes, western Arctic Canada. *Permafrost and Periglacial Processes*, *32*(2), 261–276. https://doi.org/10.1002/ppp.2113

Castagner, A., Brenning, A., Gruber, S., & Kokelj, S. V. (2023). Vertical distribution of excess ice in icy sediments and its statistical estimation from geotechnical data (Tuktoyaktuk Coastlands and Anderson Plain, Northwest Territories). *Arctic Science*, *9*(2), 483–496. https://doi.org/10.1139/as-2021-0041

Clark, P. U. (1994). Unstable Behavior of the Laurentide Ice Sheet over Deforming Sediment and Its Implications for Climate Change. *Quaternary Research*, *41*(1), 19–25. https://doi.org/10.1006/qres.1994.1002

Costard, F., Dupeyrat, L., Séjourné, A., Bouchard, F., Fedorov, A., & Saint-Bézar, B. (2021). Retrogressive Thaw Slumps on Ice-Rich Permafrost Under Degradation: Results From a Large-Scale Laboratory Simulation. *Geophysical Research Letters*, *48*(1), e2020GL091070. https://doi.org/10.1029/2020GL091070

Coulombe, S., Fortier, D., Lacelle, D., Kanevskiy, M., & Shur, Y. (2019). Origin, burial and preservation of late Pleistocene-age glacier ice in Arctic permafrost (Bylot Island, NU, Canada). *The Cryosphere*, *13*(1), 97–111. https://doi.org/10.5194/tc-13-97-2019

Coulombe, S., Fortier, D., Lacelle, D., St-Onge, G., & Guertin-Pasquier, A. (2024). Early Pleistocene glacier ice preserved in permafrost in the eastern Canadian Arctic. *Geology*. https://doi.org/10.1130/G52446.1

Crickmay, C. H. (1967). A note on the term bocanne. *American Journal of Science*, *265*(7), 626–627. https://doi.org/10.2475/ajs.265.7.626

Dallimore, S.A., Wolfe, S., 1988. Massive ground ice associated with glaciofluvial sediments, Richards Islands, N.W.T. Canada. In: Proceedings of the Fifth International Conference on Permafrost, Vol. 1, Tapir, Trondheim, pp. 132–137.

Dalton, A. S., Dulfer, H. E., Margold, M., Heyman, J., Clague, J. J., Froese, D. G., Gauthier, M. S., Hughes, A. L. C., Jennings, C. E., Norris, S. L., & Stoker, B. J. (2023). Deglaciation of the north American ice sheet complex in calendar years based on a comprehensive database of chronological data: NADI-1. *Quaternary Science Reviews*, *321*, 108,345. https://doi.org/10.1016/j.quascirev.2023.108345

Dawson, G. M. (1881). Report on an exploration from Port Simpson on the Pacific coast, to Edmonton on the Saskatchewan, embracing a portion of the northern part of British Columbia and the Peace River country, 1879. *Geological Survey of Canada, 1-177*. https://doi.org/10.4095/302782

Duk-Rodkin, A., Barendregt, R. W., Froese, D. G., Weber, F., Enkin, R., Rod Smith, I., Zazula, G. D., Waters, P., & Klassen, R. (2004). Timing and extent of plio-pleistocene glaciations in north-western canada and east-central alaska. In J. Ehlers & P.L. Gibbard, *Developments in Quaternary Sciences* (Vol. 2, pp. 313–345). Elsevier B. V. https://doi.org/10.1016/S1571-0866(04) 80206-9

Dyke, A. S. (1993). Landscapes of cold-centred Late Wisconsinan ice caps, Arctic Canada. *Progress in Physical Geography: Earth and Environment*, *17*(2), 223–247. https://doi.org/10.1177/030913339301700208

Dyke, A. S., & Evans, D. J. A. (2003). Ice-Marginal Terrestrial Landsystems: Northern Laurentide and Innuitian Ice Sheet Margins. In *Glacial Landsystems* (Arnold, pp. 143–165). https://www.researchgate.net/publication/270758451

Dyke, A. S., & Savelle, J. M. (2000). Major end moraines of Younger Dryas age on Wollaston Peninsula, Victoria Island, Canadian Arctic: Implications for paleoclimate and for formation of hummocky moraine. *Canadian Journal of Earth Sciences*, *37*(4), 601–619.

Dyke, A.S., Giroux, D. & Robertson, L. (2003). *Paleovegetation maps of Northern North America,18,000 to 1,000 BP* [Data set]. Geological Survey of Canada. Open File 4682.

England, J. H., Furze, M. F. A., & Doupé, J. P. (2009). Revision of the NW Laurentide Ice Sheet: Implications for paleoclimate, the northeast extremity of Beringia, and Arctic Ocean sedimentation. *Quaternary Science Reviews*, *28*(17), 1573–1596. https://doi.org/10.1016/j.quascirev.2009.04.006

Evans, D. J. A., Smith, I. R., Gosse, J. C., & Galloway, J. M. (2021). Glacial landforms and sediments (landsystem) of the Smoking Hills area, Northwest Territories, Canada: Implications for regional Pliocene – Pleistocene Laurentide Ice Sheet dynamics. *Quaternary Science Reviews*, *262*, 106,958. https://doi.org/10.1016/j.quascirev.2021.106958

French, H. M. (2007). *The periglacial environment* (3rd ed.). John Wiley and Sons. https://books-scholarsportal-info.proxy.bib.uottawa.ca/en/read?id=/ebooks/ebooks2/pda/2011-12-01/1/13559.9,780,470,865,903#page=12

French, H. M., & Harry, D. G. (1990). Observations on buried glacier ice and massive segregated ice, western arctic coast, Canada. *Permafrost and Periglacial Processes*, *1*(1), 31–43. https://doi.org/10.1002/ppp.3430010105

Fritz, M., Wetterich, S., Meyer, H., Schirrmeister, L., Lantuit, H., & Pollard, W. H. (2011). Origin and characteristics of massive ground ice on Herschel Island (western Canadian Arctic) as revealed by stable water isotope and Hydrochemical signatures. *Permafrost and Periglacial Processes*, *22*(1), 26–38. https://doi.org/10.1002/ppp.714

Fulton, R. J. (1995). Surficial materials of Canada. *Commission géologique du Canada, Carte série "A"*, 1880A, Ressources naturelles Canada. https://doi.org/10.4095/205040

Environment and Climate Change Canada (2024, June 27). *Canadian Climate Normals*. Government of Canada. Retrieved October 7, 2024, from https://climate.weather.gc.ca/climate_normals/index_e.html

Grasby, S. E., Bryant, R., Bringué, M. & Galloway, J. M. (2018). *Mineralogy and aquatic geochemistry associated with Smoking Hills bocannes*. Geological Survey of Canada, Open File, 8482, 17-21. https://doi.org/10.4095/311321

Grasby, S., Perciva, J., Smith, I. R., Galloway, J., & Bringué, M. (2023). Burning shales, acid ponds, and toxic waters—The long term impact of Cretaceous volcanism on the Canadian Arctic. Yellowknife Geoscience Forum Abstract Volume, p. 19. https://www.nwtgeoscience.ca/gsforum/sites/gsforum/files/resources/2023_abstractvolume.pdf

Grasby, S. E., Percival, J. B., Bilot, I., Ardakani, O. H., Smith, I. R., Galloway, J., Bringué, M., & McLoughlin-Coleman, T. (2022). Extensive jarosite deposits formed through auto-combustion and weathering of pyritiferous mudstone, Smoking Hills (Ingniryuat), Northwest Territories, Canadian Arctic – A potential Mars analogue. *Chemical Geology*, *587*, 120,634. https://doi.org/10.1016/j.chemgeo.2021.120634

Harry, D. G., French, H. M., & Pollard, W. H. (1988). Massive ground ice and ice-cored terrain near Sabine Point, Yukon Coastal Plain. *Canadian Journal of Earth Sciences*, *25*(11), 1846–1856. https://doi.org/10.1139/e88-174

Heginbottom, J.A., Dubreuil, M.-A., and Harker, P.A.C. (1995). Permafrost – Canada, National Atlas of Canada MCR 4177; Department of Energy, Mines and Resources Canada, scale 1:7 500 000. https://open.canada.ca/data/en/dataset/d1e2048b-ccff-5852-aaa5-b861bd55c367

Holland, K. M., Porter, T. J., Criscitiello, A. S., & Froese, D. G. (2023). Ion geochemistry of a coastal ice wedge in northwestern Canada: Contributions from marine aerosols and implications for ice‐wedge paleoclimate interpretations. *Permafrost and Periglacial Processes*, *34*(2), 180–193. https://doi.org/10.1002/ppp.2184

Holland, K. M., Porter, T. J., Froese, D. G., Kokelj, S. V., & Buchanan, C. A. (2020). Ice-Wedge Evidence of Holocene Winter Warming in the Canadian Arctic. *Geophysical Research Letters*, *47*(12). https://doi.org/10.1029/2020GL087942

Hu, K., Issler, D. R., Chen, Z., & Brent, T. A. (2013). Permafrost investigation by well logs, and seismic velocity and repeated shallow temperature surveys, Beaufort-Mackenzie Basin. Geological Survey of Canada, Open File 6956. https://doi.org/10.4095/293120

Huang, L., Willis, M. J., Li, G., Lantz, T. C., Schaefer, K., Wig, E., Cao, G., & Tiampo, K. F. (2023). Identifying active retrogressive thaw slumps from ArcticDEM. *ISPRS Journal of Photogrammetry and Remote Sensing*, *205*, 301–316. https://doi.org/10.1016/j.isprsjprs.2023.10.008

Ingólfsson, Ó., & Lokrantz, H. (2003). Massive ground ice body of glacial origin at Yugorski Peninsula, arctic Russia. *Permafrost and Periglacial Processes*, *14*(3), 199–215. https://doi.org/10.1002/ppp.455

Klassen, R. W. (1971). Surficial geology, Franklin Bay and Brock River, District of Mackenzie, Northwest Territories. *Geological Survey of Canada, Open File*, 48. https://doi.org/10.4095/129145

Kokelj, S. V., & Burn, C. R. (2004). Tilt of Spruce Trees near Ice Wedges, Mackenzie Delta, Northwest Territories, Canada. *Arctic, Antarctic, and Alpine Research*, *36*(4), 615–623. https://www.jstor.org/stable/1552316

Lacelle, D., Brooker, A., Fraser, R. H., & Kokelj, S. V. (2015). Distribution and growth of thaw slumps in the Richardson Mountains–Peel Plateau region, northwestern Canada. *Geomorphology*, *235*, 40–51. https://doi.org/10.1016/j.geomorph.2015.01.024

Lacelle, D., Fisher, D., Clark, I. D., & Berinstain, A. (2008). Distinguishing between vapour- and liquid-formed ground ice in the northern martian regolith and potential for biosignatures preserved in ice bodies. *Icarus*, *197*(2), 458–469. https://doi.org/10.1016/j.icarus.2008.05.017

Lacelle, D., Fisher, D. A., Coulombe, S., Fortier, D., & Frappier, R. (2018). Buried remnants of the Laurentide Ice Sheet and connections to its surface elevation. *Scientific Reports*, *8*(1), 1-10. https://doi.org/10.1038/s41598-018-31166-2

Lacelle, D., Lauriol, B., & Clark, I. D. (2004). Segregated-intrusive ice of subglacial meltwater origin in retrogressive thaw flow headwalls, Richardson Mountains, NWT, Canada. *Quaternary Science Reviews*, *23*(5–6), 681–696. https://doi.org/10.1016/j.quascirev.2003.09.005

Lachniet, M. S., Lawson, D. E., & Sloat, A. R. (2012). Revised^{14} C dating of ice wedge growth in interior Alaska (USA) to MIS 2 reveals cold paleoclimate and carbon recycling in ancient permafrost terrain. *Quaternary Research*, *78*(2), 217–225. https://doi.org/10.1016/j.yqres.2012.05.007

Lakeman, T. R., & England, J. H. (2012). Paleoglaciological insights from the age and morphology of the Jesse moraine belt, western Canadian Arctic. *Quaternary Science Reviews*, *47*, 82–100. https://doi.org/10.1016/j.quascirev.2012.04.018

Lakeman, T. R., Pieńkowski, A. J., Nixon, F. C., Furze, M. F. A., Blasco, S., Andrews, J. T., & King, E. L. (2018). Collapse of a marine-based ice stream during the early Younger Dryas chronozone, western Canadian Arctic. *Geology*, *46*(3), 211–214. https://doi.org/10.1130/G39665.1

Lang, S. Q., Bernasconi, S. M., & Früh-Green, G. L. (2012). Stable isotope analysis of organic carbon in small (µg C) samples and dissolved organic matter using a GasBench preparation device. *Rapid Communications in Mass Spectrometry*, *26*(1), 9–16. https://doi.org/10.1002/rcm.5287

Lang, S. Q., McIntyre, C. P., Bernasconi, S. M., Früh-Green, G. L., Voss, B. M., Eglinton, T. I., & Wacker, L. (2016). Rapid 14C Analysis of Dissolved Organic Carbon in Non-Saline Waters. *Radiocarbon*, *58*(3), 505–515. https://doi.org/10.1017/RDC.2016.17

Lecavalier, B. S., Fisher, D. A., Milne, G. A., Vinther, B. M., Tarasov, L., Huybrechts, P., Lacelle, D., Main, B., Zheng, J., Bourgeois, J., & Dyke, A. S. (2017). High Arctic Holocene temperature record from the Agassiz ice cap and Greenland ice sheet evolution. *Proceedings of the National Academy of Sciences*, *114*(23), 5952–5957. https://doi.org/10.1073/pnas.1616287114

Leffingwell, E. D. K. (1915). Ground-Ice Wedges: The Dominant Form of Ground-Ice on the North Coast of Alaska. *The Journal of Geology*, *23*(7), 635–654. https://doi.org/10.1086/622281

Lewkowicz, A. G., & Way, R. G. (2019). Extremes of summer climate trigger thousands of thermokarst landslides in a High Arctic environment. *Nature Communications*, *10*(1), 1-11. https://doi.org/10.1038/s41467-019-09314-7

Lorrain, R. D., & Demeur, P. (1985). Isotopic Evidence for Relic Pleistocene Glacier Ice on Victoria Island, Canadian Arctic Archipelago. *Arctic and Alpine Research*, *17*(1), 89–98. https://doi.org/10.2307/1550964

Mackay, J. R. (1971). The Origin of Massive Icy Beds in Permafrost, Western Arctic Coast, Canada. *Canadian Journal of Earth Sciences*, *8*(4), 397–422. https://doi.org/10.1139/e71-043

Mackay, J. R. (1972). The World of Underground Ice. Annals of the Association of American Geographers, 62(1), 1–22.

Mackay, J. R. (1974). *The Msckenzie Delts Area, N.W.T.* Government of Canada. https://emrlibrary.gov.yk.ca/gsc/miscellaneous_reports/mr-23.pdf

Mackay, J. R. (1975). Reticulate Ice Veins in Permafrost, Northern Canada: Reply. *Canadian Geotechnical Journal*, *12*(1), 163–165. https://doi.org/10.1139/t75-018

Mackay, J. R. (1984). The direction of ice-wedge cracking in permafrost: Downward or upward? *Canadian Journal of Earth Sciences*, *21*(5), 516–524. https://doi.org/10.1139/e84-056

Mackay, J. R. (1993). Air temperature, snow cover, creep of frozen ground, and the time of ice-wedge cracking, western Arctic coast. *Canadian Journal of Earth Sciences*, *30*(8), 1720–1729. https://doi.org/10.1139/e93-151

Mackay, J. R. (1995). Ice wedges on hillslopes and landform evolution in the late Quaternary, western Arctic coast, Canada. *Canadian Journal of Earth Sciences*, *32*(8), 1093–1105. https://doi.org/10.1139/e95-091

Mackay, J. R., & Dallimore, S. R. (1992). Massive ice of the Tuktoyaktuk area, western Arctic coast, Canada. *Canadian Journal of Earth Sciences*, *29*(6), 1235–1249. https://doi.org/10.1139/e92-099

Mackay, J. R., & Matthews, J. V. (1983). Pleistocene ice and sand wedges, Hooper Island, Northwest Territories. *Canadian Journal of Earth Sciences*, *20*(7), 1087–1097. https://doi.org/10.1139/e83-097

Margold, M., Stokes, C. R., & Clark, C. D. (2015). Ice streams in the Laurentide Ice Sheet: Identification, characteristics and comparison to modern ice sheets. *Earth-Science Reviews*, *143*, 117–146. https://doi.org/10.1016/j.earscirev.2015.01.011

Margold, M., Stokes, C. R., Clark, C. D., & Kleman, J. (2014). Ice streams in the Laurentide Ice Sheet: A new mapping inventory. *Journal of Maps*, *11*(3), 380–395. https://doi.org/10.1080/17445647.2014.912036

Mathews, W. H., & Bustin, R. M. (1984). Why do the Smoking Hills smoke? *Canadian Journal of Earth Sciences*, *21*(7), 737–742. https://doi.org/10.1139/e84-080

Michel, F. A. (1990). Isotopic Composition of Ice-Wedge Ice in Northwestern Canada. *Fifth Canadian Permafrost Conference, Nordicana*, *54*, 5–9.

Murseli, S., Middlestead, P., St-Jean, G., Zhao, X., Jean, C., Crann, C. A., Kieser, W. E., & Clark, I. D. (2019). The Preparation of Water (DIC, DOC) and Gas (CO2, CH4) Samples for Radiocarbon Analysis at AEL-AMS, Ottawa, Canada. *Radiocarbon*, *61*(5), 1563–1571. https://doi.org/10.1017/RDC.2019.14

Murton, J. B. (2005). Ground-ice stratigraphy and formation at North Head, Tuktoyaktuk Coastlands, western Arctic Canada: A product of glacier–permafrost interactions. *Permafrost and Periglacial Processes*, *16*(1), 31–50. https://doi.org/10.1002/ppp.513

Murton, J. B. (2013). 8.14 Ground Ice and Cryostratigraphy. In J. F. Shroder (Ed.), *Treatise on Geomorphology* (pp. 173–201). Academic Press. https://doi.org/10.1016/B978-0-12-374739-6.00206-2

Murton, J. B., French, H. M., & Lamothe, M. (1997). Late Wisconsinan erosion and eolian deposition, Summer Island area, Pleistocene Mackenzie Delta, Northwest Territories: Optical dating and implications for glacial chronology. *Canadian Journal of Earth Sciences*, *34*(2), 190–199. https://doi.org/10.1139/e17-015

Murton, J. B., Frechen, M., & Maddy, D. (2007). Luminescence dating of mid- to Late Wisconsinan aeolian sand as a constraint on the last advance of the Laurentide Ice Sheet across the Tuktoyaktuk Coastlands, western Arctic Canada. *Canadian Journal of Earth Sciences, 44*(6), 857–863. https://doi.org/10.1139/E07-015

Murton, J. B., Waller, R. I., Hart, J. K., Whiteman, C. A., Pollard, W. H., & Clark, I. D. (2004). Stratigraphy and glaciotectonic structures of permafrost deformed beneath the northwest margin of the Laurentide ice sheet, Tuktoyaktuk Coastlands, Canada. *Journal of Glaciology*, *50*(170), 399–412. https://doi.org/10.3189/172756504781829927

NWT Centre for Geomatics. (2021, February 5). *Level II EcoRegions (map)*. https://www.maps.geomatics.gov.nt.ca/Geocortex/Essentials/REST/sites/NWT_Species_and_Habitat_Viewer/virtualdirectory/metadataviewer/index.html? folder=xmldata&name=Level%20II%20EcoRegions&displayname=Level%20II%20EcoRegions

Okulitch, A. V., & Irwin, D. (2017). *Geological Compilation of the Western Mainland and Arctic Islands of the Northwest Territories* (NWT Open File 2016-09) [ESRI® digital files]. Northwest Territories Geological Survey. https://datahub-ntgs.opendata.arcgis.com/maps/d3d9e3c0786f4c59b5827db4dc9d3702/about

O'Neill, H. B., Wolfe, S. A., & Duchesne, C. (2020). *Ground ice map of Canada* [Map]. Natural Resources Canada. https://ostrnrcan-dostrncan.canada.ca/handle/1845/138065

Palstra, S. W. L., & Meijer, H. A. J. (2014). Biogenic Carbon Fraction of Biogas and Natural Gas Fuel Mixtures Determined with 14C. *Radiocarbon*, *56*(1), 7–28. https://doi.org/10.2458/56.16514

Pollard, W. H., & French, H. M. (1980). A first approximation of the volume of ground ice, Richards Island, Pleistocene Mackenzie delta, Northwest Territories, Canada. *Canadian Geotechnical Journal*, *17*(4), 509–516. https://doi.org/10.1139/t80-059

Rampton, V. N. (1988). *Quaternary Geology of the Tuktoyaktuk Coastlands, Northwest Territories*. Government of Canada (423; p. 98). https://doi.org/10.4095/126937

Reimer, P. J., Brown, T. A., & Reimer, R. W. (2004). *Discussion: Reporting and calibration of post-bomb 14C data*. *46*(3). https://epic.awi.de/id/eprint/45280/1/Reimer-etal_2004.pdf

Reimer, P. J., Austin, W. E. N., Bard, E., Bayliss, A., Blackwell, P. G., Ramsey, C. B., Butzin, M., Cheng, H., Edwards, R. L., Friedrich, M., Grootes, P. M., Guilderson, T. P., Hajdas, I., Heaton, T. J., Hogg, A. G., Hughen, K. A., Kromer, B., Manning, S. W., Muscheler, R., … Talamo, S. (2020). The IntCal20 Northern Hemisphere Radiocarbon Age Calibration Curve (0–55 cal kBP). *Radiocarbon*, *62*(4), 725–757. https://doi.org/10.1017/RDC.2020.41

Ritchie, J. C., & Hare, F. K. (1971). Late-quaternary vegetation and climate near the arctic tree line of northwestern North America. *Quaternary Research*, *1*(3), 331–342. https://doi.org/10.1016/0033-5894(71)90,069-X

Roy, C., Campbell-Heaton, K., Lacelle, D., & Pollard, W. (2023). Massive ground ice of glacial meltwater origin in raised marine-deltaic sediments, Fosheim Peninsula, high Arctic Canada. *Quaternary Research*, 1–12. https://doi.org/10.1017/qua.2023.30

Rudy, A. C. A., Lamoureux, S. F., Kokelj, S. V., Smith, I. R., & England, J. H. (2017). Accelerating Thermokarst Transforms Ice-Cored Terrain Triggering a Downstream Cascade to the Ocean. *Geophysical Research Letters*, *44*(21), 11,080-11,087. https://doi.org/10.1002/2017GL074912

Selwyn, A.E.C. (1877). Report on exploration in the Yukon and Mackenzie basins, Northern Territories. Geological Survey of Canada, Annual Report, Part D, pp. 1-163.

Sheath, R. G., Havas, M., Hellebust, J. A., & Hutchinson, T. C. (1982). Effects of long-term natural acidification on the algal communities of tundra ponds at the Smoking Hills, N.W.T., Canada. *Canadian Journal of Botany*, *60*(1), 58–72. https://doi.org/10.1139/b82-008

Shur, Y., Hinkel, K. M., & Nelson, F. E. (2005). The transient layer: Implications for geocryology and climate-change science. *Permafrost and Periglacial Processes*, *16*(1), 5–17. https://doi.org/10.1002/ppp.518

Smith, M. W., & Riseborough, D. W. (2002). Climate and the limits of permafrost: A zonal analysis. *Permafrost and Periglacial Processes*, *13*(1), 1–15. https://doi.org/10.1002/ppp.410

Souchez, R., Jouzel, J., Lorrain, R., Sleewaegen, S., Stiévenard, M., & Verbeke, V. (2000). A kinetic isotope effect during ice formation by water freezing. *Geophysical Research Letters*, *27*(13), 1923–1926. https://doi.org/10.1029/2000GL006103

St-Jean, G. (2003). Automated quantitative and isotopic (13 C) analysis of dissolved inorganic carbon and dissolved organic carbon in continuous-flow using a total organic carbon analyser. *Rapid Communications in Mass Spectrometry*, *17*(5), 419–428. https://doi.org/10.1002/rcm.926

St-Jean, G., Kieser, W. E., Crann, C. A., & Murseli, S. (2017). Semi-Automated Equipment for CO2 Purification and Graphitization at the A.E. Lalonde AMS Laboratory (Ottawa, Canada). *Radiocarbon*, *59*(3), 941–956. https://doi.org/10.1017/RDC.2016.57

St-Onge, D. A., & McMartin, I. (2002). La Moraine du Lac Bluenose (Territoires du Nord-Ouest), une moraine à noyau de glace de glacier. *Géographie physique et Quaternaire*, *53*(2), 287–295. https://doi.org/10.7202/005696ar

Stoker, B. J., Dulfer, H. E., Stokes, C. R., Brown, V. H., Clark, C. D., Ó Cofaigh, C., Evans, D. J. A., Froese, D., Norris, S. L., & Margold, M. (2024). *Ice flow dynamics of the northwestern Laurentide Ice Sheet during the last deglaciation* [Preprint]. https://doi.org/10.5194/egusphere-2024-137

Stoker, B. J., Margold, M., Gosse, J. C., Hidy, A. J., Monteath, A. J., Young, J. M., Gandy, N., Gregoire, L. J., Norris, S. L., & Froese, D. (2022). The collapse of the Cordilleran–Laurentide ice saddle and early opening of the Mackenzie Valley, Northwest Territories,

Canada, constrained by ^{10}Be exposure dating. *The Cryosphere*, *16*(12), 4865–4886. https://doi.org/10.5194/tc-16-4865-2022

Stokes, C. R., Margold, M., Clark, C. D., & Tarasov, L. (2016). Ice stream activity scaled to ice sheet volume during Laurentide Ice Sheet deglaciation. *Nature*, *530*(7590), 322–326. https://doi.org/10.1038/nature16947

St-Onge, D. A., & McMartin, I. (1995). *Quaternary geology of the Inman River area, Northwest Territories*. *446*. https://doi.org/10.4095/203578

Stuiver, M., & Polach, H. A. (1977). Discussion Reporting of 14C Data. *Radiocarbon*, *19*(3), 355–363. https://doi.org/10.1017/S0033822200003672

Surficial geology, Franklin Bay and Brock River, District of Mackenzie, Northwest Territories—Le Dépôt fédéral de science ouverte du Canada. (n.d.). Retrieved October 28, 2024, from https://ostrnrcan-dostrncan.canada.ca/entities/publication/aa148476-3e89-42ea-81e5-8ece65d55cc7

Tarasov, L., Dyke, A. S., Neal, R. M., & Peltier, W. R. (2012). A data-calibrated distribution of deglacial chronologies for the North American ice complex from glaciological modeling. *Earth and Planetary Science Letters*, *315–316*, 30–40. https://doi.org/10.1016/j.epsl.2011.09.010

Treat, C. C., Kleinen, T., Broothaerts, N., Dalton, A. S., Dommain, R., Douglas, T. A., Drexler, J. Z., Finkelstein, S. A., Grosse, G., Hope, G., Hutchings, J., Jones, M. C., Kuhry, P., Lacourse, T., Lähteenoja, O., Loisel, J., Notebaert, B., Payne, R. J., Peteet, D. M., … Brovkin, V. (2019). Widespread global peatland establishment and persistence over the last 130,000 y. *Proceedings of the National Academy of Sciences*, *116*(11), 4822–4827. https://doi.org/10.1073/pnas.1813305116

Van der Sluijs, J., Kokelj, S. V., & Tunnicliffe, J. F. (2023). Allometric scaling of retrogressive thaw slumps. *The Cryosphere*, *17*(11), 4511–4533. https://doi.org/10.5194/tc-17-4511-2023

Vaughan, J., England, J. H., Coulthard, R. D., & La Farge, C. (2024). Passage and removal of the Amundsen Gulf Ice Stream, NW Laurentide Ice Sheet, recorded by the glacial and sea level

history of southern Banks Island, Arctic Canada. *Quaternary Science Reviews*, *344*, 108880. https://doi.org/10.1016/j.quascirev.2024.108880

Vinther, B. M., Buchardt, S. L., Clausen, H. B., Dahl-Jensen, D., Johnsen, S. J., Fisher, D. A., Koerner, R. M., Raynaud, D., Lipenkov, V., Andersen, K. K., Blunier, T., Rasmussen, S. O., Steffensen, J. P., & Svensson, A. M. (2009). Holocene thinning of the Greenland ice sheet. *Nature*, *461*(7262), 385–388. https://doi.org/10.1038/nature08355

Wang, B., Paudel, B., & Li, H. (2016). Behaviour of retrogressive thaw slumps in northern Canada—Three-year monitoring results from 18 sites. *Landslides*, *13*(1), 1–8. https://doi.org/10.1007/s10346-014-0549-y

Williams, P. J. (1968). Ice distribution in permafrost profiles. *Canadian Journal of Earth Sciences*, *5*(6), 1381–1386. https://doi.org/10.1139/e68-136

Worsley, P. (1999). Context of relict Wisconsinan glacial ice at Angus Lake, SW Banks Island, western Canadian Arctic and stratigraphic implications. *Boreas, 28*(4), 543–550. https://doi.org/10.1111/j.1502-3885.1999.tb00240.x

Young, R. A., Gordon, L. M., Owen, L. A., Huot, S., & Zerfas, T. D. (2020). Evidence for a late glacial advance near the beginning of the Younger Dryas in western New York State: An event postdating the record for local Laurentide ice sheet recession. *Geosphere*, *17*(1), 271–305. https://doi.org/10.1130/GES02257.1

Zazula, G. D., MacKay, G., Andrews, T. D., Shapiro, B., Letts, B., & Brock, F. (2009). A late Pleistocene steppe bison (*Bison priscus*) partial carcass from Tsiigehtchic, Northwest Territories, Canada. *Quaternary Science Reviews*, *28*(25), 2734–2742. https://doi.org/10.1016/j.quascirev.2009.06.012

Zdanowicz, C., Hall, G., Vaive, J., Amelin, Y., Percival, J., Girard, I., Biscaye, P., & Bory, A. (2006). Asian dustfall in the St. Elias Mountains, Yukon, Canada. *Geochimica et Cosmochimica Acta*, *70*(14), 3493–3507. https://doi.org/10.1016/j.gca.2006.05.005

Zhou, Y., Guo, H., Lu, H., Mao, R., Zheng, H., & Wang, J. (2015). Analytical methods and application of stable isotopes in dissolved organic carbon and inorganic carbon in

groundwater. *Rapid Communications in Mass Spectrometry*, *29*(19), 1827–1835. https://doi.org/10.1002/rcm.7280

Annex

Table 3. Comparative Radiocarbon ages of the IntCal 20 and IntCal 13 calibration curve of ice wedges samples taken from the Anderson River slump (ARS), the Franklin Bay slump (FBS) and Coal River slump (CRS).

Sample site and ID	Lab ID	IntCal 20		IntCal 13	
		Calibrated age range and probability (cal yr BP)	Median (cal yr BP)	Calibrated age range and probability (cal yr BP)	Median (cal yr BP)
ARS 002C	UOC-25119	13750-14160 (93.8%)	13,930	13710-14170 (95.3%)	13,910
ARS 005B	UOC-26607	15215-15920 (95.4%)	15,560	15200-15940 (95.4%)	15,555
ARS 005C	UOC-25120	12440-12680 (80.1%)	12,540	12370-12620 (83.6%)	12,470
ARS 007AC	UOC-25121	11600-11950 (90%)	11,780	11600-12050 (94.2%)	11,820
ARS 009AC	UOC-25122	12040-12620 (94.4%)	12,345	12081-12570 (95.4%)	12,350
FBS 015A	UOC-25123	2300-2360 (54.3%)	2,310	2300-2360 (62.5%)	2,320
FBS 015B	UOC-26608	3110-3370 (92.6%)	3,240	3110-3370 (92.9%)	3,240

Table 4. Anderson River Slump water geochemistry data.

Sample ID	Ice type	D ‰	^{18}O ‰	Ba (mg/L)	Ca (mg/L)	K (mg/L)	Mg (mg/L)	Na (mg/L)	Sr (mg/L)	Cl (mg/L)	SO_4 (mg/L)
002A	Ice wedge	-246,6	-30,8	0,1	120,2	5,5	16,7	6,1	0,5	4,6	405,1
002B	Ice wedge	-247,4	-30,8	0,1	128,1	4,5	14,2	4,2	0,5	3,5	418,4
002C	Ice wedge	-249,2	-30,9	0,1	117,8	5,2	14,6	5,1	0,6	4,6	427,2
003A	Massive ice	-233,7	-28,9	0,1	27,1	10,5	7,7	46,9	0,3	8,0	53,7
003B	Massive ice	-233,7	-28,7	0,1	30,9	12,1	9,9	62,6	0,3	8,4	62,6
003C	Massive ice	-236,9	-29,0	0,1	26,1	14,4	8,9	71,3	0,3	10,4	65,2
003D	Massive ice	-237,7	-29,3	0,1	27,3	12,8	9,1	63,3	0,3	9,7	63,1
003E	Massive ice	-235,2	-29,0	0,1	25,2	13,0	8,4	55,2	0,3	3,4	47,4
003F	Massive ice	-236,3	-29,0	0,1	25,4	15,0	8,7	62,5	0,3	3,8	84,0
003G	Massive ice	-237,5	-29,0	0,1	27,8	17,5	11,1	68,9	0,3	4,8	97,1
003H	Massive ice	-236,8	-28,9	0,1	35,8	14,6	13,4	67,7	0,4	3,8	100,1
003I	Massive ice	-237,6	-28,9	0,1	31,0	14,4	11,1	67,6	0,3	3,0	75,3
004	Massive ice	-231,2	-28,6								
005A	Ice wedge	-221,2	-27,5	0,1	76,5	11,6	16,7	8,9	0,4	4,7	346,7
005B	Ice wedge	-219,4	-27,3	0,0	124,0	13,8	31,3	18,3	0,7	6,6	596,9
005C	Ice wedge	-217,2	-27,3	0,1	38,0	7,0	9,9	5,4	0,2	2,8	125,2
006A	Ice vein	-225,3	-28,1	0,1	49,8	8,7	14,3	10,4	0,2	3,5	184,7
006B	Ice vein	-227,6	-28,3	0,1	48,1	7,4	11,4	7,6	0,3	1,6	185,0
007A	Ice wedge	-255,6	-31,9	0,1	135,4	6,4	14,1	6,5	0,6	5,8	478,3

007B	Ice wedge	-255,1	-31,7	0,1	119,8	6,7	12,2	5,6	0,7	5,5	506,3
007C	Ice wedge	-254,1	-31,6	0,1	140,1	7,6	18,1	5,7	0,7	4,5	560,0
008A	Massive ice	-228,0	-28,2	0,2	32,9	15,3	9,3	46,7	0,4	5,7	104,6
008B	Massive ice	-234,2	-28,6	0,1	35,8	9,3	9,3	37,2	0,3	2,8	81,5
008C	Massive ice	-235,1	-28,9	0,1	38,3	11,2	9,9	50,0	0,3	2,3	120,7
008D	Massive ice	-235,6	-29,1	0,1	27,6	19,2	13,9	90,8	0,4	2,9	211,1
008E	Massive ice	-238,6	-29,2	0,1	29,4	14,8	9,5	80,2	0,3	2,4	113,0
008F	Massive ice	-240,4	-29,1	0,1	32,2	17,1	10,5	87,4	0,3	2,1	148,0
009A	Ice wedge	-256,4	-32,0	0,1	155,4	8,5	18,9	9,1	0,8	5,8	612,8
009B	Ice wedge	-252,7	-31,0	0,1	132,0	5,8	11,1	5,3	0,6	3,6	452,8
009C	Ice wedge	-252,5	-30,9	0,1	137,7	5,9	14,1	5,6	0,6	4,1	497,4
010A	Active layer	-166,7	-20,9	0,1	73,5	4,2	38,1	8,3	0,6	5,2	21,1
010B	Active layer	-165,5	-20,4	0,2	26,5	5,8	12,0	3,2	0,3	1,5	11,1
012	Diamict	-186,7	-23,7	0,0	164,2	16,8	49,9	33,3	0,9	4,8	794,6
014	Diamict	-184,8	-23,5								

Table 5. Franklin Bay Slump water geochemistry data.

Sample ID	Ice type	D ‰	^{18}O ‰	Ba (mg/L)	Ca (mg/L)	K (mg/L)	Mg (mg/L)	Na (mg/L)	Sr (mg/L)	Cl (mg/L)	SO_4 (mg/L)
019	Diamict	-223,7	-27,8								
015A	Ice wedge	-160,7	-20,7	0,0	11,5	2,3	5,8	2,1	0,0	5,4	27,2
015B	Ice wedge	-159,1	-20,6	0,0	11,0	2,7	5,7	2,2	0,0	4,7	19,3
015C	Ice wedge	-162,0	-20,6	0,1	14,0	2,8	6,7	2,0	0,1	3,9	21,2
018A	Massive ice	-223,6	-27,8	0,2	22,3	9,7	6,8	19,4	0,3	0,7	61,5
018B	Massive ice	-219,9	-26,8	0,1	23,3	14,9	7,6	33,8	0,3	1,3	83,3
018C	Massive ice	-224,4	-27,4	0,2	30,7	17,2	9,9	39,3	0,4	1,3	106,4
018D	Massive ice	-223,6	-27,2	0,2	17,8	9,2	5,8	23,4	0,2	0,9	49,9
018E	Massive ice	-223,5	-27,5	0,2	18,9	9,7	5,7	21,9	0,2	0,5	47,0
018F	Massive ice	-223,7	-27,7	0,2	17,0	7,9	5,6	17,1	0,2	0,6	33,4
018G	Massive ice	-224,3	-27,7	0,2	25,7	8,7	8,0	20,9	0,3	0,6	48,5
018H	Massive ice	-226,2	-27,9	0,2	21,3	11,0	6,9	27,1	0,3	0,8	60,6
018I	Massive ice	-225,6	-27,6	0,1	6,3	12,1	1,9	0,9	0,3	0,6	71,8
018J	Massive ice	-221,7	-27,5	0,0	6,4	0,9	1,9	0,6	0,0	0,3	10,1
018K	Massive ice	-222,5	-27,7	0,1	16,1	2,4	5,6	2,3	0,1	1,2	20,1
018L	Massive ice	-222,1	-27,5	0,1	15,2	2,8	3,8	2,9	0,1	0,3	12,8
018M	Massive ice	-222,5	-27,4	0,2	26,9	11,5	7,8	20,7	0,3	0,5	54,0

018N	Massive ice	-222,1	-27,5	0,1	19,4	11,9	6,1	32,6	0,3	0,8	79,4
018O	Ice lens	-188,3	-25,2	0,1	23,9	2,0	3,5	2,4	0,1	2,2	61,3
018P	Ice lens	-184,0	-24,1	0,0	6,0	1,2	2,3	0,9	0,0	0,8	7,4
020A	Massive ice	-212,1	-26,8	0,0	7,6	1,5	2,8	1,2	0,0	0,6	12,6
020B	Massive ice	-208,2	-26,3	0,0	6,1	1,1	2,2	1,1	0,0	0,4	4,2
020C	Massive ice	-211,0	-26,8	0,0	4,0	0,6	1,4	0,9	0,0	0,5	2,4
020D	Massive ice	-214,3	-26,8	0,0	3,9	0,7	1,2	0,6	0,0	0,3	1,9
020E	Massive ice	-215,2	-27,1	0,0	12,0	1,4	3,3	1,2	0,0	0,3	3,6
020F	Massive ice	-215,2	-27,1	0,0	10,3	1,2	2,6	0,6	0,0	0,3	3,1
020G	Massive ice	-215,6	-27,2	0,0	4,7	0,7	1,6	0,2	0,0	0,2	1,2
020H	Massive ice	-213,2	-27,1	0,0	5,0	0,6	1,9	0,2	0,0	0,2	1,7

Table 6. Coal River Slump water geochemistry data.

Sample ID	**Ice type**	**D ‰**	**^{18}O ‰**	**Ba (mg/L)**	**Ca (mg/L)**	**K (mg/L)**	**Mg (mg/L)**	**Na (mg/L)**	**Sr (mg/L)**	**Cl (mg/L)**	**SO_4 (mg/L)**
021A	Ice lens	-258,7	-32,6	0,0	6,2	1,7	2,3	1,0	0,0	1,0	10,2
021B	Ice lens	-248,5	-31,2	0,0	8,8	0,8	1,3	0,7	0,1	0,9	11,0
021C	Ice lens	-255,3	-32,1	0,0	7,3	0,8	1,7	0,5	0,0	0,6	12,4
022A	Massive ice	-240,9	-30,5	0,0	104,6	15,4	52,7	38,5	1,0	67,3	566,6
022B	Massive ice	-242,4	-30,7	0,0	127,5	16,1	61,6	38,7	1,2	58,5	733,9
022C	Massive ice	-244,7	-30,7	0,2	52,1	7,4	12,9	6,2	0,6	1,2	123,0
022D	Massive ice	-244,8	-30,8	0,1	25,7	5,1	6,0	6,7	0,3	0,9	45,7
022E	Massive ice	-247,6	-31,2	0,1	27,2	4,9	6,1	5,5	0,3	1,0	46,4
022F	Massive ice	-244,9	-30,7	0,1	24,5	4,3	6,0	5,0	0,3	1,4	43,6
023A	Diamict	-236,1	-29,8	0,1	73,8	8,4	47,2	15,1	0,4	25,1	358,9
023B	Diamict	-239,5	-30,2	0,1	62,8	6,1	34,8	9,0	0,3	14,7	295,3
023C	Diamict	-243,0	-30,6	0,1	38,7	4,7	21,2	5,7	0,2	8,4	135,5
023D	Diamict	-246,3	-31,3	0,1	13,1	1,7	5,2	1,3	0,1	1,0	32,4

Table 7. Acid River Slump water geochemistry data.

Sample ID	**Ice type**	**D ‰**	**^{18}O ‰**	**Ba (mg/L)**	**Ca (mg/L)**	**K (mg/L)**	**Mg (mg/L)**	**Na (mg/L)**	**Sr (mg/L)**	**Cl (mg/L)**	**SO_4 (mg/L)**
030A	Massive ice	-206,9	-25,9	0,1	18,4	6,0	7,8	7,8	0,1	1,8	99,1

030B	Massive ice	-221,0	-28,2	0,0	84,3	34,8	34,7	54,5	0,5	7,7	579,9
030C	Massive ice	-220,8	-28,0	0,0	53,7	29,9	21,7	41,2	0,6	6,6	486,3
030D	Massive ice	-220,3	-28,0	0,0	94,0	19,9	34,1	51,9	0,4	11,6	357,8

Table 8. Percentage grain size of sediments found in different samples taken at the Acid River slump (AcRS), Anderson River slump (ARS), Coal River slump (CRS) and Franklin Bay slump (FBS). Note that the pebbles are reported as a weight percentage of bulk sample, while the sand silt and clay are reported as volumetric percentage of sediments smaller than 2 mm.

Site	Sample ID	Ice type	Pebbles weight %	Sand volume %	Silt (63-2um) volume %	Clay (<2um) volume %
ARS	003B	Massive ice	5,57	23,88	60,73	15,39
ARS	003D	Massive ice	6,15	23,95	59,95	16,09
ARS	003F	Massive ice	9,56	22,89	60,77	16,34
ARS	004	Massive ice	11,01	21,36	60,88	17,76
ARS	008A	Massive ice	13,06	22,60	59,54	17,85
ARS	008D	Massive ice	6,60	25,91	57,20	16,89
ARS	008E	Massive ice	5,23	24,31	58,44	17,25
ARS	010A	Active layer	1,25	10,53	74,86	14,61
ARS	010A (H2O2 Treated)	Active layer	1,17	6,56	78,18	15,25
ARS	012	Diamict	16,93	34,01	53,02	12,97
ARS	014	Diamict	7,60	29,06	55,68	15,26
FBS	016B	Diamict	4,60	29,45	58,46	12,09
FBS	017	Active layer	0,83	26,45	68,15	5,40
FBS	017 (H2O2 Treated)	Active layer	0,01	15,49	78,31	6,20
FBS	018B	Massive ice	15,10	33,85	50,45	15,71
FBS	018D	Massive ice	8,09	34,84	48,66	16,49
FBS	018H	Massive ice	9,61	40,02	46,98	13,00
FBS	018N	Massive ice	10,00	27,15	54,42	18,43
FBS	019	Diamict	4,50	30,31	51,89	17,80
FBS	020E	Massive ice	13,26	55,30	35,40	9,30
CRS	022B	Massive ice	1,97	36,21	50,90	12,89
CRS	022D	Massive ice	4,91	33,81	52,81	13,38
CRS	023A	Diamict	2,17	50,19	39,91	9,90
CRS	023D	Diamict	0,30	53,82	37,37	8,81

AcRS	030B	Massive ice	2,63	23,49	67,32	9,19
AcRS	030D	Massive ice	4,32	17,64	67,25	15,11

Table 9. Abundances of major and minor elements within the sediments of different samples taken at the Acid River slump (AcRS), Anderson River slump (ARS), Coal River slump (CRS) and Franklin Bay slump (FBS)

Site	Sample ID	Ice type	Ca (ppm)	Mg (ppm)	Na (ppm)	K (ppm)	S (ppm)	Fe (ppm)	Sr (ppm)	Rb (ppm)	Ba (ppm)
ARS	002	Ice wedge	2,78	1,34	0,021	0,19	0,306	2,4	49,7	11,3	214
ARS	003A	Massive ice	2,43	1,23	0,03	0,26	0,4	2,87	72,1	14,1	47,2
ARS	003E	Massive ice	1,77	1,09	0,042	0,3	0,349	2,85	63,7	16,5	156
ARS	003I	Massive ice	1,65	1,04	0,046	0,32	0,348	2,8	61,8	16,1	151
ARS	004	Massive ice	1,84	1,06	0,039	0,25	0,336	2,68	60	14,8	157
ARS	005	Ice wedge	2,4	1,33	0,023	0,25	0,191	2,36	49,3	13,9	204
ARS	008A	Massive ice	2,53	1,24	0,029	0,23	0,444	2,88	73,8	13	30,7
ARS	008C	Massive ice	2,62	1,29	0,033	0,25	0,359	2,52	68,3	14,9	166
ARS	008F	Massive ice	1,84	1,08	0,049	0,3	0,318	2,73	64,5	15,8	170
ARS	009	Ice wedge	2,69	1,33	0,022	0,19	0,308	2,22	52,4	10,9	188
ARS	010A	Active layer	0,7	0,63	0,021	0,44	0,038	2,88	62	24,6	184
ARS	012	Diamict	2,58	1,38	0,016	0,19	0,138	2,86	56,7	11,6	178
ARS	014	Diamict	2,52	1,05	0,019	0,2	0,128	2,52	58	11,9	165
FBS	016A	Diamict	2,65	1,77	0,026	0,28	1,227	3	74,5	13,3	25,3
FBS	016C	Diamict	2,4	1,67	0,033	0,32	1,018	3,12	71,1	16,3	56,1
FBS	017	Active layer	0,81	0,51	0,01	0,2	0,161	2,79	44,5	8,3	162
FBS	018A	Massive ice	3,51	2,25	0,029	0,25	0,459	2,28	58,8	13,7	117
FBS	018E	Massive ice	3,64	2,4	0,032	0,28	0,422	2,33	59,8	14,7	124
FBS	018G	Massive ice	4	2,53	0,023	0,18	0,507	2,38	61,6	10,6	58,3
FBS	018N	Massive ice	3,42	2,22	0,035	0,23	0,521	2,66	70	12,7	48,6
FBS	019	Diamict	3,84	2,54	0,023	0,16	0,491	2,43	61,5	10,1	52,5
FBS	020A	Massive ice	10,9	6,93	0,114	0,55	0,245	4,51	95,1	28,4	355
FBS	020F	Massive ice	8,48	5,68	0,025	0,16	0,147	1,56	41,3	8,8	77,6
CRS	022A	Massive ice	4,48	2,53	0,016	0,13	0,319	2,46	60	9,1	64,6
CRS	022C	Massive ice	3,87	1,88	0,025	0,25	0,391	2,61	78,1	15,8	139
CRS	022F	Massive ice	4,45	2,05	0,014	0,12	0,467	2,9	83,6	9,3	44,5
CRS	023A	Diamict	6,05	3,47	0,012	0,13	0,104	2,09	47,1	8	137
CRS	023C	Diamict	5,32	2,94	0,012	0,16	0,136	2,37	55,2	9,8	169

AcRS	030A	Massive ice	1,7	0,95	0,029	0,23	1,335	2,77	55,9	11,4	23,6
AcRS	030D	Massive ice	1,41	1,02	0,024	0,18	0,682	3,09	51,5	10,1	28,4

Table 10. Abundances of rare earth elements within the sediments of different samples taken at the Acid River slump (AcRS), Anderson River slump (ARS), Coal River slump (CRS) and Franklin Bay slump (FBS)

Site	Sample ID	Ice type	Cd (ppm)	Cs (ppm)	La (ppm)	Ce (ppm)	Pr (ppm)	Nd (ppm)	Sm (ppm)	Eu (ppm)	Tb (ppm)	Gd (ppm)	Dy (ppm)	Ho (ppm)	Er (ppm)	Tm (ppm)	Yb (ppm)
ARS	002	Ice wedge	0,23	0,89	12,1	28,9	3,5	14,8	2,8	0,5	0,4	2,9	1,9	0,3	0,9	0,1	0,7
ARS	003A	Massive ice	0,4	0,62	16,7	37,3	4,4	18,9	4,1	0,8	0,6	3,5	3,1	0,5	1,4	0,2	1,1
ARS	003E	Massive ice	0,34	0,83	17,8	40,5	4,5	19,2	3,8	0,7	0,5	3,8	2,7	0,5	1,3	0,2	1,1
ARS	003I	Massive ice	0,36	0,81	17,9	40,9	4,6	19,6	3,6	0,7	0,5	3,6	2,7	0,5	1,3	0,2	1,1
ARS	004	Massive ice	0,34	0,77	16,9	38,5	4,5	18,1	3,5	0,6	0,5	3,5	2,5	0,4	1,2	0,2	1
ARS	005	Ice wedge	0,28	0,82	13,6	32,4	3,7	15,8	3,3	0,6	0,4	2,9	2,1	0,4	1	0,1	0,8
ARS	008A	Massive ice	0,3	0,53	16,5	36,8	4,4	18,5	3,7	0,8	0,5	3,7	3,1	0,5	1,4	0,2	1,1
ARS	008C	Massive ice	0,26	0,84	14,8	33,8	3,9	16,6	3,4	0,6	0,5	3,1	2,3	0,4	1,1	0,1	0,9
ARS	008F	Massive ice	0,29	0,84	17,4	39,5	4,6	19,6	3,7	0,7	0,5	3,6	2,6	0,4	1,2	0,2	1,1
ARS	009	Ice wedge	0,24	0,77	11,4	26,7	3,1	13,5	3	0,5	0,4	2,7	1,9	0,3	0,9	0,1	0,7
ARS	010A	Active layer	0,16	0,97	24,8	54,4	6,6	27,8	5,6	1	0,7	5,1	3,6	0,6	1,8	0,2	1,5

ARS	012	Diamict	0,3	0,6	14,4	33	4	17,1	3,6	0,7	0,5	3,2	2,7	0,5	1,1	0,1	0,9
ARS	014	Diamict	0,4	0,68	13,7	30,7	3,6	15,5	3	0,7	0,5	2,9	2,4	0,4	1,1	0,1	0,9
FBS	016A	Diamict	2,2	0,51	18,1	40,3	4,7	19,7	4,1	0,8	0,6	3,7	3,4	0,6	1,6	0,2	1,3
FBS	016C	Diamict	1,67	0,74	16,8	39,3	4,5	18,6	3,9	0,6	0,5	3,4	2,7	0,5	1,2	0,2	1,1
FBS	017	Active layer	1,4	0,18	17	36,7	4,2	18,2	3,4	0,7	0,5	3,1	2,8	0,5	1,3	0,2	1,1
FBS	018A	Massive ice	0,36	0,75	15,5	35,3	3,9	16,8	2,8	0,6	0,4	3,1	2,2	0,4	1,1	0,1	0,9
FBS	018E	Massive ice	0,29	0,82	16,5	37,1	4,3	17,5	3,2	0,6	0,5	3,2	2,2	0,4	1,1	0,1	0,9
FBS	018G	Massive ice	0,3	0,5	15,1	34,7	4	16,8	3,7	0,7	0,5	3	2,5	0,5	1,2	0,1	1
FBS	018N	Massive ice	0,4	0,52	18,1	40,3	4,6	19,3	4,2	0,8	0,5	3,6	3	0,5	1,4	0,2	1,1
FBS	019	Diamict	0,4	0,45	16,4	38	4,3	18,5	3,3	0,8	0,5	3,3	2,9	0,5	1,2	0,2	1
FBS	020A	Massive ice	1,42	1,86	30,8	71,2	7,9	31,6	6,3	1	0,8	5,7	4,1	0,7	1,9	0,2	1,6
FBS	020F	Massive ice	0,11	0,62	11,1	25,7	2,9	11,4	2,3	0,4	0,3	2,1	1,4	0,2	0,7	< 0.1	0,6
CRS	022A	Massive ice	0,2	0,47	13,2	31,4	3,6	15,8	3,1	0,7	0,4	2,7	2,3	0,4	1,1	0,1	0,9
CRS	022C	Massive ice	0,18	0,96	14,7	34,8	3,9	16,7	3,7	0,7	0,5	3,5	2,2	0,4	1	0,1	0,8
CRS	022F	Massive ice	0,2	0,5	12	29,4	3,6	16,2	3,3	0,7	0,5	3,1	2,4	0,4	1,1	0,1	0,9
CRS	023A	Diamict	0,2	0,4	12,7	29,7	3,3	14,4	3	0,6	0,4	2,6	2,2	0,4	1	0,1	0,8
CRS	023C	Diamict	0,2	0,47	13,6	30,9	3,5	15,4	2,8	0,6	0,4	2,8	2,4	0,4	1,1	0,1	0,8

AcRS	030A	Massive ice	2,84	0,49	16,1	38	4,3	18	3,6	0,7	0,5	3,6	2,6	0,5	1,2	0,2	1,2
AcRS	030D	Massive ice	0,8	0,47	19,2	43,7	5,1	21,7	4,7	0,9	0,6	4	3,4	0,6	1,6	0,2	1,3